STUDIES IN THE THEORY OF MULTIBAND SUPERCONDUCTORS

Brendan Wilson

May 2015

Statement of Originality

I declare that the work presented in this thesis is my own, and was produced during my enrolment within the Department of Theoretical Physics at the Australian National University. This work has not been been previously submitted for any other degree at any university or other tertiary education institution.

_____   _____

Brendan Wilson   Date

Acknowledgements

Abstract

While the theory of multiband superconductivity has existed since the work of Suhl et al. and Moskalenko, it has only been with the discovery of superconductivity in magnesium diboride that this theory could be applied to real materials. The list of possible multiband superconductors has steadily grown, and these materials have attractive properties that warrant further investigation.

In this thesis we look at two theories of multiband superconductivity and the connection between them. The first theory is the multiband generalisation of the microscopic theory of Bardeen, Cooper and Schrieffer (BCS). In the case of three superconducting bands, it is well known that there can exist a phase transition to a new phase of superconductivity, the time-reversal-symmetry-broken (TRSB) state. We show that in this state the full multiband theory reduces exactly to solving a set of independent one-band equations. In addition, this reduction produces a set of conditions among these one-band solutions which must be satisfied for them to be solutions of the full multiband equations. These conditions can therefore be used to find the TRSB transition temperature.

The phenomenological Ginzburg-Landau theory (GL), which can be derived as an expansion of BCS theory around the critical temperature, has also had a multiband generalisation which was first derived by Tilley. Peeter's and co-workers recently used the Gor'kov technique to find the next order corrections to the theory, extending the validity to slightly lower temperatures. We restrict ourselves to the field-free case and find extensions to very high order. We show that in the one-band theory and most multiband cases the superconducting gap in this extended GL theory converges to the BCS theory over almost the entire temperature range. However there are some cases in the multiband theory where the GL expansion diverges. This divergence is related to the appearance of a second critical temperature in the uncoupled limit.

Finally we apply a range of numerical methods to find vortex and skyrmion states in multiband superconductors. The skyrmion states are variations of the well-known vortex states, and only appear when the bulk superconductor is in the TRSB state. We find that, with the bulk in the TRSB state, the low order skyrmion solutions

are very robust and are very likely to evolve from a random initial configuration. However the higher order skyrmion states are instead likely to form a collection of lower order skyrmions and vortices, and a large amount of control is required to form them.

Contents

List of Figures

List of Symbols

a	Second order expansion coefficient in GL theory
A_θ	Angular component of the vector potential in cylindrical coordinates
A	Unknown function for ansatz of vector potential
$\mathbf{A}$	Magnetic vector potential
$\mathcal{A}$	$\ln\left(\frac{2\hbar\omega_{\mathrm{D}}\mathrm{e}^{\Gamma}}{\pi k_{\mathrm{B}}T_{\mathrm{c}}}\right)$
b	Fourth order expansion coefficient in GL theory
$b_{m\nu}$	Higher order expansion coefficients in extended GL theory
$\mathbf{B}$	Magnetic induction
B_y	Magnetic induction in y direction
c	Speed of light, $299\,792\,458\,\mathrm{m\,s^{-1}}$
$\hat{c}$	Electron annihilation operator in momentum space
$\hat{c}^\dagger$	Electron creation operator in momentum space
C_v	Specific heat
d	Separation of vortex cores in double vortex solution
D_ν	Order parameter dispersion constant in TDGL
e	Euler's constant
e	Elementary electric charge, $1.602 \times 10^{-19}\,\mathrm{C}$
e^*	Electric charge of a Cooper pair
$\hat{\mathbf{e}}_x$	Unit vector in the x direction
$\hat{\mathbf{e}}_\theta$	Unit vector in the θ direction
E_{v}	Energy of a vortex solution relative to a uniform superconductor
$\mathbf{E}$	Electric field vector
f_ν	Modified Fermi function
f	Magnitude of the order parameter
$f_\nu^{(m)}$	Order parameter expansion coefficient in the variational method
$f_\nu^{(1)}(z, z^*)$	Variational method single vortex solution
$f_\nu^{(2)}(z, z^*)$	Variational method giant vortex solution
$\delta f_\nu^{(2)}(z, z^*)$	Variational method interaction correction ansatz

$f_{\nu 0}$	Magnitude of the order parameter in the absence of an applied magnetic field
$\mathscr{F}$	Anomalous Green function
F_{n0}	Free energy density of the normal state in the absence of an applied magnetic field
F_{s}	Free energy density of a superconductor
F_{s0}	Free energy density of a superconductor in the absence of an applied magnetic field
g	Electron-electron effective coupling strength
$\breve{g}$	Interband coupling matrix
$\mathscr{G}$	Full Green function
$\mathcal{G}$	Green function in the normal state
$\widetilde{\mathcal{G}}$	Conjugate Green function in the normal state
$\mathcal{G}^{0}$	Green function in the normal state in the absence of a magnetic field
$\widetilde{\mathcal{G}}^{0}$	Conjugate Green function in the normal state in the absence of a magnetic field
G_{s}	Gibbs free energy density of a superconductor
G_{s0}	Gibbs free energy density of a superconductor in the absence of an applied magnetic field
G_{n0}	Gibbs free energy density of a normal material in the absence of an applied magnetic field
$\hbar$	Reduced Planck's constant, $1.054\,57 \times 10^{-34}\,\mathrm{kg\,m^2\,s^{-1}}$
h_x	Discretisation step in the x direction
h_y	Discretisation step in the y direction
$\mathbf{H}$	Applied magnetic field
H_{c}	Thermodynamic critical field of a superconductor
H_{c1}	First critical field of a type II superconductor, the field at which the first vortex enters the superconductor
H_{c2}	Second critical field of a type II superconductor, above which the bulk of the material returns to the normal state
$\hat{H}$	A Hamiltonian
i	Unit imaginary number
i	Integer index
$i_{\max}$	Computational cut-off in the interaction correction ansatz in the variational method
$\breve{I}$	Matrix with the integrals from multiband BCS appearing on the diagonal
$\mathbb{I}$	Identity matrix

Im	Imaginary part of a complex quantity
j	Integer index
$\mathbf{j}$	Current
k	Absolute value of the vector $\mathbf{k}$
$\mathbf{k}$	Electron momentum vector
k_F	Fermi momentum
k_B	Boltzmann constant, $1.380\,648\,8 \times 10^{-23}\,\mathrm{J\,K^{-1}}$
K_0	Modified Bessel function of order zero
$\hat{K}_\mathrm{BCS}$	BCS Hamiltonian
$\hat{K}_\mathrm{eff}$	Mean-filed approximation to the BCS Hamiltonian
$\check{L}$	$\check{g}^{-1} - \check{N}(0)\mathcal{A}$
L_x	Length of the computational domain in the x direction
L_y	Length of the computational domain in the y direction
m	Particle's mass
m	Integer index
m_e	Mass of an electron
m^*	Mass of a Cooper pair
m_max	Cut-off in the expansion of ansatz in the variational method
$\mathbf{M}$	Magnetisation
$M_\mathbf{q}$	Electron-phonon matrix element
n	Integer index
n_V	Number of vortices
$N(0)$	Density of states at the Fermi level
$\check{N}(0)$	Matrix containing the density of states at the Fermi level of each band
$\mathcal{O}$	Big O notation for the leading order behaviour of a function
$\vec{P}_m$	Extended GL
$\mathbf{q}$	Phonon momentum vector
Q	Quadratic kernel in Gor'kov expansion
$\vec{Q}_m$	Extended GL kernel in Gor'kov expansion
Q^0	Quadratic kernel in Gor'kov expansion without magnetic field
$\mathbf{r}$	Position vector, with components $\{x,y,z\}$ in Cartesian coordinates, and $\{\rho,\theta,z\}$ in cylindrical coordinates
r	Magnitude of a position vector
R	Quartic kernel in Gor'kov expansion
$\vec{R}$	Right-hand side of self-consistent equation in extended GL

Re	Real part of a complex quantity
S	Entropy
t	Reduced temperature, T/T_c
t	Time
t	Imaginary time parameter used in finite temperature field theory
T	Temperature
T_c	Critical temperature
T^0	Temperature where one superconducting gap vanishes as the sign of the gap flips
T^*	Critical temperature for the transition to the TRSB state
$T_{\nu c}$	Critical temperature of band ν in the absence of any interband coupling
T_t	Time ordering operator
Tr	Trace
$u_\mathbf{k}$	BCS variational coefficient
U_x	Link variable used in TDGL
U_y	Link variable used in TDGL
$v_\mathbf{k}$	BCS variational coefficient
v_F	Fermi velocity
w	Weighting of the single vortex solution in the variational method
$\vec{W}$	Vector in extended GL theory, $\mathcal{A}\check{N}(0)\Delta - \vec{R}$
$\vec{\tilde{W}}$	$\vec{W}$ scaled by $\tau^{1/2}$
$\vec{W}^{(n)}$	Coefficient in the expansion of $\vec{\tilde{W}}$
W_z	Link variable for the magnetic field in TDGL
x	Cartesian component of a position vector
$\mathbf{x}$	Position vector
x_L	Left end point in finite difference method
x_R	Right end point in finite difference method
y	Cartesian component of a position vector
$\mathbf{y}$	Position vector
$\mathbf{y_i}$	Position vector
z	Cartesian component of a position vector
z	Complex $z = x + \mathrm{i}y$ used in the conformal variational transformation
$\mathbf{z}$	Position vector
β	Thermodynamic beta, $1/k_\mathrm{B}T$
γ	Interband coupling coefficient in the multiband Ginzburg-Landau theory

Γ	Euler-Mascheroni constant, $0.577216\ldots$
$\delta(r)$	Dirac delta function
$\delta^3(\mathbf{r})$	Three-dimensional Dirac delta function
Δ	Superconducting gap
$\vec{\Delta}$	Vector containing the set of superconducting gaps
Δ_0	Superconducting gap at zero temperature
$\vec{\tilde{\Delta}}$	Extended GL theory scaled by $\tau^{1/2}$
$\vec{\Delta}^{(n)}$	Coefficient in expansion of the scaled gap in extended GL theory
ε	Energy
$\varepsilon_{\mathbf{k}}$	Electron energy as a function of the wave-vector $\mathbf{k}$
ϵ_{F}^0	Fermi energy in the normal state
$\zeta(z)$	Riemann zeta function
$\zeta_{\mathbf{A}}$	Thermal Gaussian noise term for vector potential in TDGL
ζ_ν	Thermal Gaussian noise term for order parameters in TDGL
$\vec{\eta}_j$	Eigenvector basis vector in extended GL
$\eta_{j,\nu}$	ν component of $\vec{\eta}_j$
θ	Angular component in cylindrical coordinates
κ	Ginzburg-Landau parameter, ξ/λ
λ	Magnetic field decay length
λ	Strong-coupling theory electron-phonon coupling coefficient
λ_{L}	Magnetic field decay length in London model
Λ	Total effective coupling parameter, $gN(0)$
$\vec{\Lambda}$	Total effective coupling matrix, $\vec{g} \cdot \vec{N}(0)$
μ	Chemical potential
μ^*	Strong-coupling theory electron-electron Coulomb pseudopotential coefficient
ν	Band index
ξ	Superconducting coherence length
ξ_0	Pippard coherence length
π	Ratio of a circle's circumference to its diameter, $3.14159\ldots$
Π	Gauge independent momentum operator, $\left(-\mathrm{i}\hbar\nabla + \frac{e^*\mathbf{A}(\mathbf{x})}{c}\right)$
ρ	Radial coordinate in cylindrical coordinates
ρ_n	Component of the basis eigenvector in extended GL
σ	A spin variable, $\uparrow$ or $\downarrow$
σ	Conduction coefficient in TDGL

σ_{ns}	Surface energy at an interface between a normal and a superconducting material
τ	Expansion parameter in GL theory, $1 - T/T_{\mathrm{c}}$
ϕ	Complex phase of an order parameter
$\phi_{\nu 0}$	Complex phase of an order parameter in the absence of a magnetic field
φ	Phase correction to normal Green function in a magnetic field
φ_0	Flux quantum, $\frac{hc}{2e} = 2.06783 \times 10^{-7}\,\mathrm{G\,cm^2}$
χ	Ratio of the magnitude of superconducting gaps
$\hat{\psi}$	Electron annihilation operator in real space
$\hat{\psi}^\dagger$	Electron creation operator in real space
$\hat{\psi}_{K\sigma}$	Temperature Heisenberg electron annihilation operator
$\hat{\psi}^\dagger_{K\sigma}$	Temperature Heisenberg electron creation operator
$\psi_j^{(n)}$	Coefficient in the expansion of the gaps in extended GL
Ψ	Ginzburg-Landau phenomenological order parameter
ω_n	Fermionic Matsubara frequency
$\omega_{\mathbf{q}}$	Phonon frequency as a function of momentum
ω_{D}	Debye frequency, which can be replaced with a more general cut-off frequency
∇	Vector differential operator

List of Abbreviations

BCS Bardeen-Cooper-Schrieffer

FTCS Forward-time-central-space

GL Ginzburg-Landau

TDGL Time-dependent Ginzburg-Landau

TRSB Time-reversal-symmetry-broken

List of Publications

Papers

The following papers were published during the PhD candidature:

[1] B. J. Wilson and M. P. Das, "Time-reversal-symmetry-broken state in the BCS formalism for a multi-band superconductor", J. Phys.: Condens. Matter **25**, 425702 (2013).

[2] B. J. Wilson and M. P. Das, "Beyond the standard model of Ginzburg-Landau theory: multiband superconductors", J. Phys.: Condens. Matter **26**, 325701 (2014).

These two papers also contribute a large portion of a review article, which has been accepted for publication:

[3] M. P. Das and B. J. Wilson, "Novel superconductivity: from bulk to nano systems", Adv. Nat. Sci.: Nanosci. Nanotechnol. **6**, 013001 (2015).

The following papers were also published during the candidature, but are not directly related to the topic of the thesis:

[4] X.-W. Guan, Z.-Q. Ma, and B. Wilson, "One-dimensional multicomponent fermions with δ-function interaction in strong- and weak-coupling limits: κ-component Fermi gas", Phys. Rev. A **85**, 033633 (2012).

[5] B. Wilson, A. Foerster, C. Kuhn, I. Roditi, and D. Rubeni, "A geometric wave function for a few interacting bosons in a harmonic trap", Phys. Lett. A **378**, 1065 (2014).

Conferences

During the candidature, my work was presented at the following conferences:

[6] B. J. Wilson and M. P. Das, "Multi-band superconductivity", in the Sixth International Conference on Advanced Materials and Nanotechnology (Feb. 11–15, 2013).

[7] B. J. Wilson and M. P. Das, "Phase diagram and chiral skyrmions in three band superconductors", in the 14th International Workshop on Vortex Matter in Superconductors (May 21–28, 2013).

[8] M. P. Das and B. J. Wilson, "Beyond the standard model of GL theory", in the 4th International Conference on Superconductivity and Magnetism (Apr. 27–, May 2, 2014).

CHAPTER ONE

Introduction

Superconductivity has a long history, with a vast number of contributors to its development, theoretical understanding, and applications since its unexpected discovery in 1911.

In this chapter we highlight some of the key developments in the field, beginning with the discovery. We look at the reasoning behind the development of the first theories of superconductivity – the London model, Ginzburg-Landau (GL) theory, and Bardeen-Cooper-Schrieffer (BCS) theory. We also briefly discuss some other theories which treat the electron-phonon interaction mechanism more explicitly.

We finish with a look at some recent developments in superconducting materials, indicating that a large class of the recently discovered superconductors with higher critical temperatures have multiple superconducting gaps. Some of the established theories of these multiband materials are also discussed, as well as some additional aspects which appear in multiband superconductors.

The remainder of this thesis is organised as follows. In chapter 2 we look in more detail at the foundations of BCS and GL theories, some results that can be found from these theories, and the connection between the two. In chapter 3 we discuss the extension to multiband BCS theory. Of particular interest is the result that under specific conditions, a new superconducting state appears. We show that when this happens the coupled multiband BCS can be decoupled, and instead form decoupled one-band BCS equations.

In chapter 4 we look at two extensions to a multiband GL theory. We include a new expansion to include many corrections in the temperature expansion. We show that this expansion is very beneficial in some cases, but fails to give much improvement under certain conditions. In chapter 5 we describe numeric approaches to solving the multiband GL equations to find magnetic vortex-like structures. We discuss some vortex solutions as well as some skyrmion solutions.

The final chapter draws conclusions and highlights further directions and applications of this work.

1.1 History of Superconductivity

1.1.1 Discovery

The discovery of superconductivity was a remarkable event that was completely unexpected. The laboratory of Heike Kamerlingh Onnes at the University of Leiden succeeded in the liquefaction of helium, allowing the investigation of the properties of materials at lower temperatures than could previously be accessed, due to its extremely low boiling point. With access to these new low temperatures, one property to be investigated was how the conductivity of metals behaved at these temperatures.

Before performing the measurement, it was known that with decreasing temperature, the resistance of metals tended to decrease. However, it was unknown whether this trend would continue in such a way that the resistance decayed linearly towards zero, whether it would retain a residual resistance, or if the resistance would increase at low temperature.

The first experiment was performed by Giles Holst, an assistant of Onnes, on a sample of mercury, which was used due to its high purity. Contrary to any of the predictions, the resistance initially fell linearly, but at about $4.2\,\mathrm{K}$ the resistance suddenly vanished, dropping by several orders of magnitude below the sensitivity of the measuring equipment [9, 10].

It was later found that in fact many materials become superconductors at sufficiently low temperatures, including a large number of elemental materials (some only under pressure), many alloys, and others with different material compositions.

1.1.2 The Meissner Effect

The original observations of superconductivity showed that superconducting materials conducted electricity with zero resistivity. While this was a startling and unexpected effect, such a material today would be called a perfect conductor, rather than a superconductor. In 1933 Meissner and Ochsenfeld [11] showed that in addition these materials possess a second property which distinguishes this state from any traditional state: a superconductor expels all magnetic fields regardless of its history (figure 1.1). This is in contrast to a perfect conductor which would trap any existing magnetic fields so that there was no change of the magnetic field within the material.
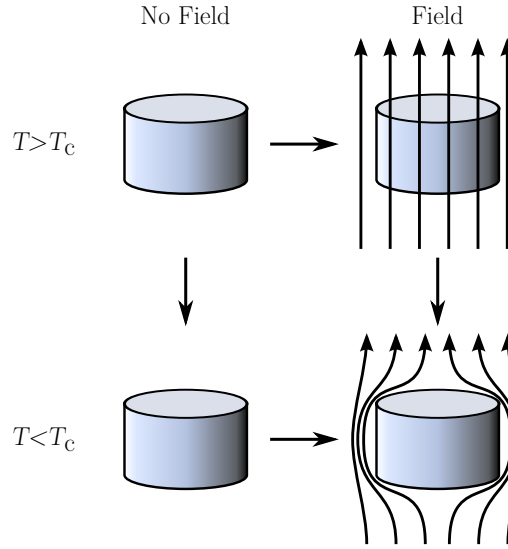
Figure 1.1: The Meissner effect: All magnetic fields are expelled from the superconductor whether the superconductor is cooled below the critical temperature before or after the magnetic field is applied.

This effect showed that the superconducting state was very different from any other observed state and gave the first insight into establishing a theory of superconductivity.

1.1.3 The London Equation

Since it was observed that superconductors conducted with zero resistivity, the assumed approach was to replace Ohm's law with a new law for superconductors:

$$\lambda_{\mathrm{L}}^2 \frac{\partial \mathbf{j}}{\partial t} = c^2 \mathbf{E}, \tag{1.1}$$

where $\lambda_{\mathrm{L}} = \sqrt{mc^2/n_s e^2}$ is the London penetration depth which parametrises the decay of the magnetic field into the bulk of the superconductor. This states the assumed relation that, due to the lack of resistance, the current inside a superconductor would continually increase under an applied electric field. Then, using Maxwell's equations, this would lead to

$$\nabla^2 \frac{\partial \mathbf{H}}{\partial t} = \frac{1}{\lambda_{\mathrm{L}}^2} \frac{\partial \mathbf{H}}{\partial t}. \tag{1.2}$$

The London brothers, Fritz and Heinz, noted that this did not prove that a superconductor obeys the Meissner effect [12], but instead shows that any magnetic field within a superconductor would remain except over a small length scale near the surface (on the order of nanometres). However the required equation that would

ensure that a superconductor obeys the Meissner effect would be the same equation, but without the time derivatives. They then showed that this would imply a new relation for the current within a superconductor, and claimed that this should be the fundamental relation defining the supercurrent. This relation is

$$\lambda_{\mathrm{L}}^2 \nabla \times \mathbf{j} = -c\mathbf{H}. \tag{1.3}$$

This leads to the electric field having an exponential decay within the superconductor, leading to the zero resistance observed. They also show how the existence of a critical magnetic field leads to a critical current for a superconducting wire of a given cross-section.

The same expression can be achieved by setting the current proportional to the vector potential in the Coulomb gauge. Pippard [13, 14] used this form to create a nonlocal theory, where, instead of the current being proportional to the vector potential at the same point, the vector potential is averaged of over a small volume with radius ξ_0 (the Pippard coherence length of the material). This length scale tends towards an intrinsic value for pure superconductors, and approaches the mean free path in heavily doped materials.

1.1.4   Ginzburg-Landau Theory and Vortex States

The next major theory of superconductivity came from the work of Ginzburg and Landau. This was based on Landau's theory of phase transitions [15]. Landau theory looks at the behaviour of systems near phase transitions, and notes that often the symmetry of a system will change as it undergoes a phase transition. This change in symmetry is quantified by using an order parameter, which is zero on one side of a phase transition and nonzero on the other.

In applying this theory to superconductors, the order parameter was chosen to be charged with an unknown charge e^*, and coupled to the vector potential via minimal coupling [16]. This theory then predicted a critical magnetic field, above which it is more favourable for the superconductor to return to the normal state.

In the uniform limit, this theory reproduces the result that the current is proportional to the vector potential, but additional terms are included when the gradient of the order parameter is nonzero.

In 1957, Abrikosov [17] showed that these equations admitted a new solution. He assumed that the magnitude of the order parameter could have a doubly periodic variation, and studied this solution near the upper critical field. In this region the
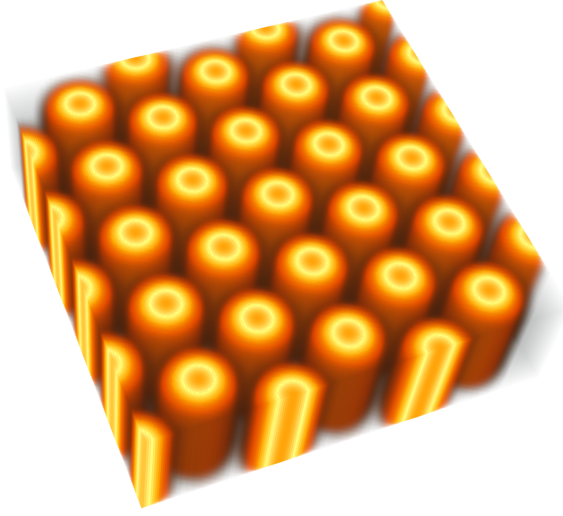
Figure 1.2: The Abrikosov vortex lattice (schematic).

order parameter is greatly suppressed and the equations can be linearised, allowing for an analytic solution of a superconducting vortex lattice. This state was seen soon after in neutron scattering by Cribier et al. [18] and decoration experiments by Essmann and Träuble [19, 20]. The vortex lattice is a triangular lattice of flux lines, each of which is confined by a circulating supercurrent, and is schematically represented in figure 1.2.

This solution is not stable for all superconductors, and this criteria divides them into two types: type I, where vortex states are suppressed, and type II, where the vortex states are stable. The presence of vortices dramatically changes the magnetic behaviour of a superconductor (figure 1.3). In type I the superconductor is in the Meissner state until the critical field H_c, where it returns to the normal state. In type II the superconductor is initially in the Meissner state. Increasing the field eventually allows vortices to enter at the field H_{c1}, where the magnetisation suddenly drops. Increasing the applied field further allows more vortices to enter the superconductor, and the magnetisation continues to fall. This continues until it drops to zero at the upper critical field H_{c2} where the material returns to the normal state.

Much work has gone in to the understanding of vortex states in all parts of the phase diagram, as they have a large impact on the behaviour in magnetic fields, including self-induced magnetic fields due to high current applications, and contribute to the dissipation of energy if they are allowed to move through the material [21, 22]. The movement of the vortices can be controlled by pinning centres, such as defects, twinning boundaries and dislocations in the crystal structure, as well as nanostructuring of the surface, especially in the case of thin films.
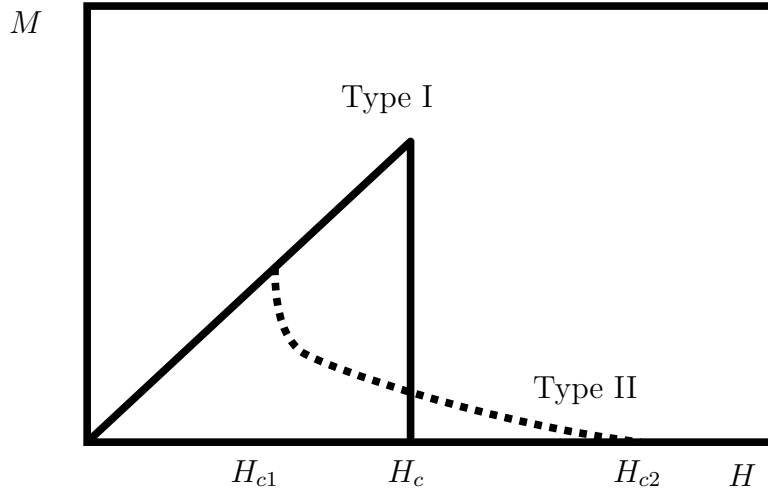
Figure 1.3: Magnetisation curve in type I and type II superconductors (schematic).

While GL theory was and still is successful at matching the properties of supercon-ductors near the transition temperature, it gave no indication as to the mechanism of superconductivity. The major hint as to the cause of superconductivity came in 1950 with the observation of the isotope effect.

1.1.5 The Isotope Effect and the Electron-Phonon Interaction

Since the discovery of superconductivity, many attempts had been made to discover the nature of the state. These efforts focused on finding properties that affected the critical temperature and other observables in a systematic way. In 1950, Maxwell [23] and Reynolds et al. [24] announced that they had independently observed a systematic variation of the critical temperature in mercury with various isotopes. The effect is known as the isotope effect, and shows that some property of the crystal lattice vibrations is involved in the formation of the state.

Similar investigations had previously been attempted in other materials (e.g. Pb [25]), but the effect was either nonexistent in these materials, or too weak to be observed.

The isotope effect instigated investigations into the electron-phonon interaction in metals. Fröhlich [26] studied how the electron-phonon interaction perturbs the Fermi sea in momentum space at zero temperature. This showed that the electron-phonon interaction could cause an attraction between electrons near the Fermi surface, and this could cause an instability which was assumed to be related to the superconducting state. This attractive interaction was further investigated by Bardeen [27], and Bardeen and Pines [28].

The interaction energy derived in these papers is

$$\frac{\hbar\omega_{\mathbf{q}}\left|M_{\mathbf{q}}\right|^2}{(\varepsilon_{\mathbf{k}} - \varepsilon_{\mathbf{k}'})^2 - (\hbar\omega_{\mathbf{q}})^2}, \tag{1.4}$$

where the interaction scatters a pair of electrons with momentum $\mathbf{k}$ and $\mathbf{k}'$ to the states $\mathbf{k} + \mathbf{q}$ and $\mathbf{k}' - \mathbf{q}$, $M_{\mathbf{q}}$ is the matrix element for the exchange of a phonon of momentum $\mathbf{q}$, and $\omega_{\mathbf{q}}$ is the frequency of an exchanged phonon. When the energy difference between the states is smaller than the energy of the exchanged phonon, the interaction energy becomes negative due to the denominator. This condition can be achieved by choosing electrons on opposite sides of the Fermi surface, so that $\mathbf{k} = -\mathbf{k}'$ and $\varepsilon_{\mathbf{k}} = \varepsilon_{\mathbf{k}'} = \epsilon_{\mathrm{F}}^0$. This results in an attractive interaction between the pair of electrons. If this attraction is large enough, then it can overcome the Coulomb repulsion. This idea of attraction between electrons was very new and is the key component of the BCS theory.

Another experimental piece of evidence was provided in 1955 with the observation of a gap in the electron spectrum in the superconducting state, which was observed using far infrared absorption [29, 30]. This indicated that a mechanism was needed where a phonon-mediated interaction causes the electrons to condense into a ground state, which is separated from the excited states by a gap. This is in contrast to a normal metal, where a continuum of states near the Fermi level is needed to allow the electrons to move easily from state to state. Instead it is usually insulators which have an energy gap at the Fermi level, preventing electrons from escaping the ground state and therefore inhibiting conduction.

The approach that brought all of this together and produced verifiable predictions is the BCS theory.

1.1.6 The Microscopic BCS Theory

BCS theory is the combined effort of Bardeen, Cooper and Schrieffer, and is outlined in three papers that appeared in quick succession. In the first paper Cooper shows that for two electrons sitting above a Fermi sea with a net attractive interaction between them, no matter how weak, there always exists a bound state as the ground state [31]. This suggests that the attractive electron-phonon interaction between electrons would cause them to form pairs, known as Cooper pairs.

In the following two papers, the authors first show how to compose a ground state of many Cooper pairs [32], and then proceed to examine many properties of the superconducting state, including the gap, the critical field, specific heat, Meissner

effect, and the penetration depth [33]. A vastly simplified form of the interaction is used, where the interaction is a constant attractive interaction within $\hbar\omega_\mathrm{D}$ of the Fermi surface, with ω_D the Debye frequency.

The ground state in the BCS theory consists of a superposition of empty and filled pairs, and hence is truly a many-body state. At zero temperature, this state can be written in the form

$$|\Psi\rangle = \prod_\mathbf{k} \left(u_\mathbf{k} + v_\mathbf{k} \hat{c}^\dagger_{\uparrow\mathbf{k}} \hat{c}^\dagger_{\downarrow-\mathbf{k}} \right) |0\rangle \,, \tag{1.5}$$

where $\hat{c}^\dagger$ is the electron creation operator, $|0\rangle$ is the vacuum state, and $u_\mathbf{k}$ and $v_\mathbf{k}$ are coefficients to be determined.

Independently, Bogoliubov [34] and Valatin [35] showed how a linear transformation can be used which diagonalises the Hamiltonian. In this way, the superconducting state is described as a ground state of paired electrons with an excitation spectrum of quasiparticles.

Gor'kov reformulated the BCS theory in the language of quantum field theory, and used this to derive the GL theory as an expansion of the BCS theory around the critical temperature [36].

1.1.7 Other Theories

Many other theories have been applied to the superconducting state. In this section we highlight some of these.

Migdal [37] showed how the electron-phonon interaction could be handled more completely in strong coupling superconductors. This work was extended by Eliashberg [38, 39] and Nambu [40]. See [41] for a review. This theory was also extended to the case of multiple superconducting bands [42] after the multiband BCS theory was established.

Using this strong coupling theory, McMillan [43] derived a new formula for the critical temperature

$$T_c = \frac{\hbar\omega_\mathrm{D}}{1.45} \exp\left(-\frac{1.04(1+\lambda)}{\lambda - \mu^*(1 + 0.62\lambda)} \right) , \tag{1.6}$$

where λ is the electron-phonon coupling constant and μ^* the repulsive Coulomb pseudopotential coefficient. Relating the phonon cut-off to the electron-phonon coupling constant, this showed that the critical temperature has a maximum, and that the materials observed to date were likely close to this limit. However several

approximations were made in this derivation, especially concerning the phonon spectrum, so a strict upper limit could not be obtained.

Anderson [44], and independently Abrikosov and Gor'kov [45, 46], extended the BCS theory to treat the case where the mean free path is much shorter than the coherence length, which occurs especially in samples with a large number of impurities. Materials in this limit are called *dirty* superconductors, and are contrasted to materials with few impurities which are called *clean* or *pure.* This theory also admits a GL type expansion around the critical temperature [47].

The Hubbard model has been applied successfully to a range of materials [48–51]. The Hubbard model is a model of electrons in a lattice. The simplest Hamiltonian includes two terms: an on-site interaction (usually repulsive due to the Coulomb interaction) and hopping between sites (usually restricted to include only nearest neighbours). However many other interactions can be included to form an extended Hubbard model. This is an effective approach for treating the layered superconductors, such as the cuprates and pnictides. See [52] for a review.

Josephson [53] examined the case of two superconductors, separated by a thin insulator. In this work, he argued that the Cooper pairs would spill out of the superconductors, tunnelling through the insulating material, and into the other superconductor. In this way the two superconductors would become coupled, with a current between the superconductors which is dependent on the phase difference between the two gaps.

The effect is separated into two effects – the DC and the AC Josephson effect. The DC effect refers to the formation of a current across the insulator in the absence of any applied potential, which is driven by the difference in the phase of the order parameters. In the AC effect, a constant applied voltage causes a sinusoidally varying current across the insulator. Josephson junctions are a key element in SQUIDS, high precision magnetic field detectors.

Eilenberger [54] made a semi-classical approximation to the Green function approach of Gor'kov to find effective transport equations. In this theory the Green functions are taken to be functions of both position and momentum. This was simplified in the dirty limit by Usadel [55], producing a useful approach to study transport processes in dirty superconductors.

The GL theory discussed previously is an expansion to lowest order of the gap around the critical temperature. It is possible to retain higher order terms in this expansion. Recently Peeters and co-workers [56–58] performed this extension to

retain the next order term in the expansion. In chapter 4 we examine the expansion in the absence of a magnetic field to a large order, treating both the one-band theory and multiband theory. Klimin et al. [59] have also recently performed a similar expansion in the theory of superconducting Fermi fluids, treating the spatial variation as a perturbation, while re-summing the terms which contribute to the magnitude of the order parameter, as defined by the uniform BCS equations.

1.2 Superconducting Materials

In this section we highlight a few families of important superconductors.

1.2.1 Elements

The elemental superconductors were the first family to be discovered. About half of all elements have a superconducting state, though the critical temperature can be extremely low, and some only become superconducting under pressure (figure 1.4). Most of these have been known to be superconducting for a long time [60] while others, such as lithium [61], have only been discovered to be superconducting recently. It is likely that as lower temperatures and higher pressures become achievable additional elements will be found to have a superconducting phase, though these are unlikely to have practical applications.

Niobium has a critical temperature of 9.25 K [62], the highest observed in bulk for any pure elemental sample. The other main stand-outs, in terms of high critical temperatures, are Technetium (7.7 K) and Lead (7.2 K).

A large class of these materials are well explained by the standard BCS theory. However the transition metals are not adequately explained by BCS theory. No isotope effect has been seen in these materials, and the pairing has a different symmetry due to the available states originating from d orbitals.

1.2.2 Alloys

Alloys are useful for studying the conditions that allow for superconductivity, as they can be used to continuously study a region of parameter space. By using two atoms with a similar atomic radius, but with a different number of conduction electrons, the chemical potential can be continuously varied. However, since the atomic radius is never identical, additional substitutions eventually cause the alloys to undergo
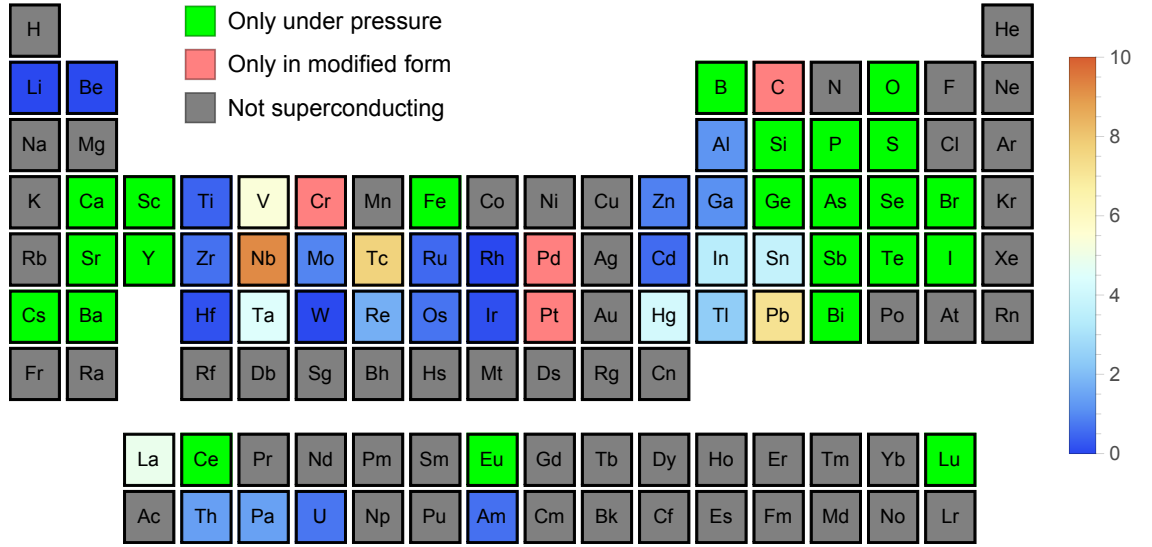
Figure 1.4: The elements which have been found to be superconducting. Some are only under high pressure (green), and some are not superconducting in bulk (pink). The colour on the other superconducting elements indicate the critical temperature in the bulk (in K).

a structural phase transition. This often occurs before the composition achieves a maximum or minimum in the critical temperature [63].

The use of alloying has been used to successfully enhance the critical temperature of many elements, as well as improving other properties, such as the critical magnetic field, and physical properties such as malleability, strength etc.

Niobium based compounds can have very high critical temperatures, for example NbTi (9.2 K), NbN (16 K), Nb_3Sn (18.3 K), and Nb_3Ge (23 K). Both NbTi and Nb_3Sn are important in practical applications due to their high critical magnetic fields.

1.2.3 Cuprates and the Increase in Critical Temperature

In 1986 Georg Bednorz and K. Alex Müller [64] announced that they had discovered a new superconducting material, LaBaCuO (or LBCO). This had a critical temperature of 30 K, and later samples of this material have achieved critical temperatures of 35 K. This was an exceptional increase over the highest critical material available at the time (Nb_3Ge with a critical temperature of 23 K). This generated a lot of interest in copper oxide ceramics, and soon after the initial announcement, a range of other copper oxide compounds were found to be superconducting with even higher critical temperatures. These include YBCO and BSCCO, with the record for the
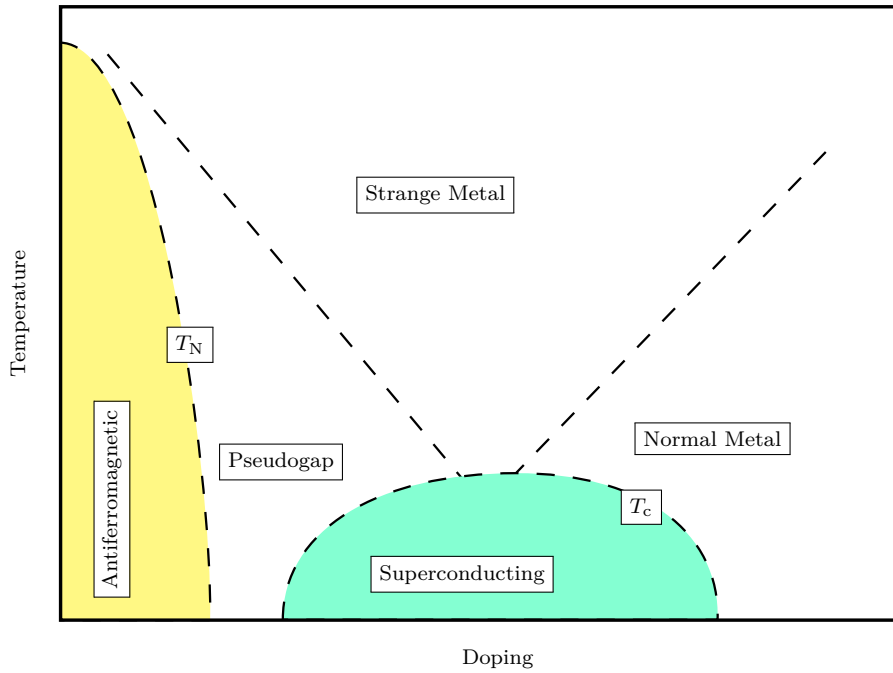
Figure 1.5: High T_c phase diagram: the cuprates have an antiferromagnetic parent material which becomes superconducting after doping (schematic).

highest critical temperature in $HgBa_2Ca_2Cu_3O_8$ [65], with a critical temperature of $133\,K$ under ambient pressure, and higher critical temperatures can be reached by applying pressure [66].

A full understanding as to the mechanism for superconductivity in these materials has not been achieved. However it is clear that the superconductivity is mostly confined to the two-dimensional copper oxide planes, with tunnelling between the dielectric-like separating material.

These cuprates have an antiferromagnetic parent compound (figure 1.5). Doping this parent material causes a lowering of the magnetic ordering, and eventually destroys the magnetic state completely. With additional doping, a superconducting phase then emerges, reaching a maximum critical temperature with an optimal doping, and then decaying again with further doping.

Some work was done to treat the cuprates using multiband theory [67, 68], however, although multiple Fermi surfaces are involved in the superconductivity of the cuprates, no evidence of multiple superconducting gaps has been found.
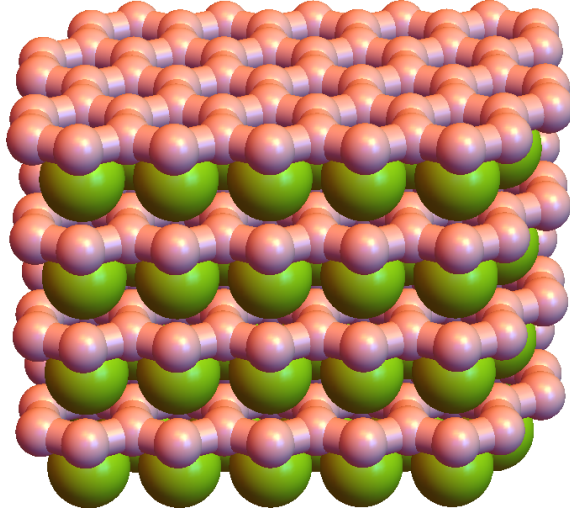
Figure 1.6: The crystal structure of magnesium diboride. The magnesium atoms are green, the boron atoms are pink.

1.2.4 Magnesium Diboride

Magnesium diboride (MgB_2) is a well-known material that has been synthesised for a long time [69], and had even been studied at low temperature (e.g. measurements of the heat capacity [70]). However, it was only in 2001 that it was found to be superconducting by Nagamatsu et al. [71]. This material has an extremely simple composition, yet has a high critical temperature of 39 K, which is higher than the critical temperature of the original cuprate superconductor LBCO.

The crystal structure is layered, with layers of magnesium forming a triangular lattice, and boron atoms forming a honeycomb lattice (figure 1.6). The isotope effect has been observed by changing the isotope of the boron atoms [72], indicating that the coupling mechanism is likely to be phonon mediated. However the effect is weaker than expected, and changing the isotope of magnesium does not affect the transition temperature. This could either indicate that there are additional coupling mechanisms, or that the phonon coupling in this material is more specific than in most materials, with only some phonon modes coupled strongly.

The band structure of MgB_2 indicates that the Fermi surface consists of four separate sheets, two of which form a layered cylindrical structure, while the other two form a tubular network [73]. The planar nature of this network causes the material to display anisotropic behaviour when the applied fields are parallel or perpendicular to the boron layers.

Experiments using point contact spectroscopy have provided evidence that there

are two distinct gaps [74, 75]. The temperature dependence of the specific heat also confirms the two-band picture of superconductivity in MgB_2 [76], and the two gaps have been attributed to the two different types of Fermi surfaces, with the largest gap associated with the atoms in the boron plane [77, 78].

A large amount of additional material on MgB_2 can be found in the review articles by Xi [79] and Zehetmayer [80].

1.2.5 Pnictides

More recently, a range of new materials have emerged with temperatures that are also placed in the category of high temperature superconductors, with temperatures above the original 30 K limit [81, 82]. These have different structures to the cuprates, and could give further insights into the possible mechanisms creating the electron-electron attraction. However, there are many similarities to the cuprates, indicating some of the properties that could be the key to this type of unconventional superconductivity.

Like the cuprates, the pnictides are layered, with the superconducting electrons forming in the iron layers. This enhances the coherence of the electrons in the plane, and increases the interaction cross-section.

They have an antiferromagnetic parent compound. With doping, the magnetic phase becomes suppressed. Then, near the point where the magnetic ordering vanishes, a superconducting phase appears. The superconducting critical temperature rises to a maximum at an ideal doping, then decays to zero.

There are four main classes of pnictide superconductors, and these determine the crystal structure. The classes are known as 11, 111, 122 and 1111, which indicate the number of each element in the material, and also differentiate between different crystal structures. Examples of the parent materials are 11: FeSe, FeAs, 111: LiFeAs, 122: $A\mathrm{Fe_2As_2}$ (A =Ba, Sr, Ca), and 1111: RFeAsO (R =La, Nd, Sm, Gd, Er, Pr ,Nd, Ce). In these, As can also be replaced with Se. These are then doped, for example by substituting O with F, to produce a superconducting compound. Good reviews about pnictide superconductors have been written by Ishida et al. [83], Mazin and Schmalian [84], and Wilson [85].

1.2.6 Other Novel Superconductors

Superconductivity has also been seen in doped covalent compounds such as boron, diamond, silicon and germanium [86, 87]. Superconductivity has also been observed in carbon nanotubes [88], doped layered graphene structures, such as CaC_6 [89], and

doped fullerenes, such as Cs_2RbC_{60} [90]. The doped graphene structures have a similar structure to MgB_2, with the superconductivity occurring in the two-dimensional hexagonal graphene layers, with weak tunnelling between the layers.

Other unconventional properties of novel superconductors include coexistence of superconductivity with antiferromagnetism ($CeCuSi_2$) [91] or with ferromagnetism (UGe_2) [92], predominantly in heavy fermion systems, coexistence of superconductivity with charge/spin ordering ($NbSe_2$, Cuprates) [93], and non-centrosymmetric heavy fermion systems ($CePt_3Si,CeInSi_3$) [94], where lack of inversion symmetry gives rise to spin-orbit interaction with no definite parity in the ground state.

1.3 Multiband Theories

Soon after the BCS theory was published, Suhl et al. [95] and Moskalenko [96] investigated an extension to superconductors with two bands crossing the Fermi surface and included the interband Josephson coupling between the bands. This work was extended by Peretti [97], Kondo [98], and Geilikman et al. [99].

Tilley [100] applied the Gor'kov technique to find a two-band GL theory as an expansion of two-band BCS theory. This is used to find the GL approximation to the upper critical field.

The two interacting electron bands lead to the creation of two superconducting gaps, with the possibility of the two gaps having very different properties. It was shown that the interband coupling caused the two critical temperatures to instead become just one critical temperature, which is enhanced above both of the uncoupled critical temperatures. This enhancement occurs regardless of the sign of the interband coupling.

The lowest energy state for a two-band superconductor has the two bands in phase or out of phase with each other. Leggett [101] examined the possibility of fluctuations in the phase difference, and showed that this causes fluctuations in the density of Cooper pairs. This leads to collective excitation states, known as Leggett modes. The energy associated with these modes is usually quite high, but at some points in the phase diagram, the energy of these modes can become arbitrarily small. There has been some evidence that this was observed with Raman spectroscopy [102], but this has not been independently verified.

The initial works on multiband theories were motivated by the fact that the transition metals were not adequately explained by BCS theory. These materials

have multiple bands near the Fermi surface, due to the presence of partially filled d orbitals, and it was conjectured that these should be treated separately. However Garland [103] argues that transition metals have a large number of impurities, and therefore the theory of dirty superconductors is more appropriate. In this theory, the electron basis states are chosen to diagonalise the scattering from the impurities before the pairing is considered. This diagonalisation mixes the states from all parts of all the Fermi surfaces, and hence the use of a multiband theory is no longer appropriate.

Similar reasoning also applies to the high temperature cuprates, and hence interest in multiband BCS theory dwindled due to the absence of any application to observed materials, until the discovery of MgB_2. This material for the first time showed clear evidence of multiple superconducting gaps and renewed interest in multiband theories. Some evidence of multiple superconducting gaps has now been observed in MgB_2, OsB_2 [104], LiFeAs [105], $FeSe_{0.94}$ [106], and other pnictides, so further development of multiband theories is important.

More recently the theories have been generalised to an arbitrary number of bands, and investigated by many groups in the context of both BCS [1, 107, 108] and GL [109–118], as well as hybrid approaches [119]. The multiband GL theory is used to investigate the behaviour of multiband materials, especially in the presence of magnetic fields.

1.3.1 Type 1.5 Superconductors

The term type 1.5 superconductivity was created in 2005 by Babaev and Speight [120]. The idea is to look at a two-band superconductor in the weak coupling limit, where, in the absence of the other band, one of the bands would be type I and the other type II. The authors claim that this combination can lead to a superconductor which is neither type I or type II. Using the definition that in type I superconductors vortex solutions are attractive while in type II they are repulsive, they show that for these multiband materials the vortex states are repulsive at short distances but attractive at large distances. This is said to lead to a clustering of vortex states at low fields, while reverting to a standard Abrikosov lattice at high fields [121].

This work has received considerable attention, however several authors have been critical of this finding. Brandt and Das [122] point out that long range attraction in type II materials is also observed in one-band GL models [123–125], so that this phenomenon is not new and does not warrant the definition of a new type of

superconductivity. Additionally, they argue that the vortex clustered state does not constitute a separate thermodynamic state from the Meissner state, and any transition from a vortex cluster to a vortex lattice would be a crossover rather than a phase transition.

Kogan and Schmalian [126] argue that the multiband GL model is incomplete. The theory is an expansion in the reduced temperature, τ, about the critical point. However, some higher order terms are retained in the expansion, but these terms are not complete. If the incomplete terms are removed from the solution, then the ratio of the order parameters in the two bands becomes a constant. Therefore it is not possible to conclusively prove within multiband GL theory whether the different bands can have separate coherence lengths. These criticisms are rejected by the original authors [127], but reinforced by Kogan and Schmalian [128].

1.3.2 Time-Reversal-Symmetry-Broken State

In addition to the standard superconducting states considered so far, there is another configuration that appears in both the multiband BCS and multiband GL theories, and is only possible in systems with three bands or more.

In clean two-band superconductors, the lowest energy state always has the bands in phase or out of phase with each other, depending on the sign of the Josephson interaction, as this configuration lowers the energy of this term without impacting on any of the other terms. This remains true even when spatial variations are considered, and in the lowest energy state the bands are always phase-locked.

However, with three bands there is the possibility of frustration between the relative phases of the bands [107]. This can occur if the interband couplings are all repulsive, or for the case of two attractive and one repulsive interaction.

When this frustration causes the relative phases of the uniform state to take on values other than 0 or π the superconductor is said to be in the Time-Reversal-Symmetry-Broken (TRSB) state.

This state has been examined within the context of multiband BCS theory [1, 108] as well as multiband GL theory [114, 116]. This state will be discussed later in more detail in multiband BCS theory in chapter 3 and briefly in multiband GL in chapter 4.

1.3.3 Skyrmion States

Skyrmion states are a generalisation of vortex states that have been found theoretically in the multiband GL when the uniform solution is in the TRSB state.

These states consist of a combination of the domain wall solutions, which separate regions of the two different ground state solutions, and fractional vortex solutions, where the phase of one order parameter shifts by 2π when following a path around the fractional vortex, while the phase of the remaining bands does not shift.

These states have been studied analytically with various approximations by Yanagisawa et al. [114], and numerically by Garaud et al. [129, 130]. Some skyrmion states will also be discussed in chapter 5.

CHAPTER TWO

Background

In this chapter we examine the fundamental theories of superconductors in more detail. We consider the two most successful theories – the phenomenological GL theory and the microscopic BCS theory. We outline the origin of the theories and outline how to form the fundamental equations. Many details are included here, and this allows only important differences in the multiband theories to be highlighted in subsequent chapters. A few fundamental results are then derived in each case.

We finish the chapter by exploring the Gor'kov technique, which allows for the derivation of the GL theory as an expansion of BCS theory about the critical temperature. This connection puts GL theory on a much more rigorous footing and allows for an analysis of where the theory is applicable. The phenomenological parameters of GL theory are written in terms of the microscopic parameters, which allows for a more direct comparison to real materials.

Finally it also allows for corrections which extend the region of applicability of the theory to lower temperatures and higher fields. This is useful in chapter 4 where we use this approach to generalise the theory to the multiband case and discuss corrections away from the critical temperature.

2.1 The Ginzburg-Landau Equations

Landau's semi-classical mean field theory of continuous second order phase transitions has been qualitatively applied to many critical phenomena [15]. The theory smooths over the details of the system, and instead looks at the sudden appearance of order below the critical temperature of the transition. This is assumed to change some symmetry of the system. To allow for this, Landau created an order parameter which has the symmetry of the more ordered system. This order parameter must then be nonzero below the phase transition, and become zero at the phase transition. Ginzburg and Landau adapted this approach and developed a systematic

phenomenological approach which they could apply to superconducting systems.

In GL theory there is assumed to be a phase transition that occurs at a critical temperature T_c. Below this temperature, a new state is formed, which is characterised by a complex order parameter Ψ. Ψ vanishes above T_c, and increases in magnitude for $T < T_c$. Near T_c, the order parameter is small, and we can therefore create an expansion in the free energy density for this parameter about this point. Because the order parameter is complex, and the free energy is a real quantity, only even powers of the order parameter enter the expansion. We use this approach to describe the superconducting state, and therefore express the free energy density of the superconducting state as

$$\mathrm{F_{s0}} = \mathrm{F_{n0}} + a(T)\,|\Psi|^2 + \frac{1}{2}b\,|\Psi|^4 + \dots, \tag{2.1}$$

where $\mathrm{F_{n0}}$ is the free energy density of the normal state and we have truncated the expansion at fourth order. We assume that the fourth order expansion coefficient, b, is large and positive, and that the variation with temperature of this coefficient is small enough that we can neglect it close to the transition temperature. If instead b is negative or zero, then additional terms would have to be retained in order for the free energy to be bounded from below, and hence have a stable equilibrium.

In the absence of applied fields and/or inhomogeneity, it is expected that the order parameter will tend towards a uniform value. Therefore, if the order parameter is allowed to vary in space, the spatial variations should be suppressed when there are no applied fields. To accomplish this a gauge invariant derivative term is added to the free energy. This also introduces the coupling of the order parameter to the vector potential. Finally a term is included to account for the energy density of a magnetic field. The free energy density of the superconducting state in GL theory is then given by

$$\mathrm{F_s} = \mathrm{F_{n0}} + \frac{1}{2m^*}\left|\left(-\mathrm{i}\hbar\nabla + \frac{e^*\mathbf{A}(\mathbf{r})}{c}\right)\Psi(\mathbf{r})\right|^2 + a(T)\,|\Psi(\mathbf{r})|^2 + \frac{1}{2}b\,|\Psi(\mathbf{r})|^4 + \frac{\mathbf{B}(\mathbf{r})^2}{8\pi}, \tag{2.2}$$

where $\mathbf{B}(\mathbf{r}) = \nabla \times \mathbf{A}(\mathbf{r})$ is the magnetic field, and e^* and m^* are a phenomenological effective charge and mass respectively.

The usual case we are interested in is when the superconductor is in a uniform external magnetic field. We write the Gibbs free energy of the system

$$\mathrm{G_s} = \mathrm{F_s} - \frac{1}{4\pi}\mathbf{B}\cdot\mathbf{H}, \tag{2.3}$$

where $\mathbf{H}$ is an externally applied magnetic field. Now, any system in thermodynamic equilibrium will minimise the Gibbs free energy. We therefore make variations of

the Gibbs free energy with respect to the complex conjugate of the order parameter, $\Psi^*(\mathbf{r})$, and the vector potential, $\mathbf{A}(\mathbf{r})$, and set the result equal to zero.

$$\frac{\delta G_s}{\delta \Psi^*} = 0, \tag{2.4a}$$

$$\frac{\delta G_s}{\delta \mathbf{A}} = 0. \tag{2.4b}$$

This leads to the GL equations

$$\frac{1}{2m^*} \left(-i\hbar\nabla + \frac{e^*\mathbf{A}(\mathbf{r})}{c}\right)^2 \Psi(\mathbf{r}) + a(T)\Psi(\mathbf{r}) + b\left|\Psi(\mathbf{r})\right|^2 \Psi(\mathbf{r}) = 0, \tag{2.5a}$$

$$\frac{c}{4\pi}\nabla \times \nabla \times \mathbf{A}(\mathbf{r}) = \frac{ie^*\hbar}{2m^*}\left(\Psi^*(\mathbf{r})\nabla\Psi(\mathbf{r}) - \Psi(\mathbf{r})\nabla\Psi^*(\mathbf{r})\right) - \frac{e^{*2}}{m^*c}\left|\Psi(\mathbf{r})\right|^2 \mathbf{A}(\mathbf{r}). \tag{2.5b}$$

Since Ampere's law tells us that $\mathbf{j}(\mathbf{r}) = \frac{c}{4\pi}\nabla \times \nabla \times \mathbf{A}(\mathbf{r})$, we can define the supercurrent as

$$\mathbf{j}(\mathbf{r}) = \frac{ie^*\hbar}{2m^*}\left(\Psi^*(\mathbf{r})\nabla\Psi(\mathbf{r}) - \Psi(\mathbf{r})\nabla\Psi^*(\mathbf{r})\right) - \frac{e^{*2}}{m^*c}\left|\Psi(\mathbf{r})\right|^2 \mathbf{A}(\mathbf{r}). \tag{2.6}$$

If the gradient terms are zero, then the supercurrent is proportional to the vector potential, as predicted by the London model.

2.1.1 Uniform Solutions and Decay Lengths

The uniform solution is the simplest to find. In this case we set the vector potential to zero, as well as the derivatives of the order parameter. This removes equation (2.5b) and greatly simplifies equation (2.5a). The resulting equation has the solutions

$$\left|\Psi\right|^2 = -\frac{a(T)}{b}, \qquad \text{or,} \tag{2.7a}$$

$$\Psi = 0. \tag{2.7b}$$

Since we have assumed that $b > 0$, the first solution is only acceptable if $a(T)$ is less than zero. We expect that, near the critical temperature, the parameter $a(T) \sim (1 - T/T_c)$, and therefore a will change sign at the critical temperature. Above the critical temperature, the trivial solution is the only solution, while below the critical temperature, the nonzero solution is the stable solution.

Next we would like to find how Ψ returns to this uniform solution in the absence of a magnetic field. To find this we again neglect equation (2.5b) and simplify equation (2.5a) to the form

$$0 = -\frac{\hbar^2}{2m^*}\nabla^2\Psi(\mathbf{r}) + a(T)\Psi(\mathbf{r}) + b\left|\Psi(\mathbf{r})\right|^2 \Psi(\mathbf{r}). \tag{2.8}$$

We want a solution which smoothly connects the state where the order parameter is zero to the nonzero uniform state. We therefore restrict our solution to be only a function of the spatial direction z and scale the order parameter by the uniform solution, $\Psi(z) = \psi(z)\sqrt{-a(T)/b}$. The equation reduces to the form

$$0 = -\frac{\hbar^2}{2m^* |a(T)|}\frac{\partial^2}{\partial z^2}\psi(z) - \psi(z) + |\psi(z)|^2\,\psi(z). \tag{2.9}$$

This indicates that the order parameter should vary on a length scale of $\xi = \sqrt{\frac{\hbar^2}{2m^*|a(T)|}}$ since scaling z by ξ reduces this to a dimensionless form. This length scale, ξ, is called the coherence length, which determines the length over which the order parameter varies.

Next we would like to find the characteristic length scale on which the magnetic field varies. To find this length scale, we assume that the order parameter has achieved the uniform solution and look at the variation of $\mathbf{A}$. In this limit, equation (2.5b) becomes

$$\frac{c}{4\pi}\nabla \times \nabla \times \mathbf{A}(\mathbf{r}) = -\frac{e^{*2}}{m^*c}\frac{|a(T)|}{b}\mathbf{A}(\mathbf{r}), \tag{2.10}$$

$$\therefore \frac{m^*c^2b}{4\pi e^{*2}|a(T)|}\nabla \times \nabla \times \mathbf{A}(\mathbf{r}) = -\mathbf{A}(\mathbf{r}). \tag{2.11}$$

This allows us to define the magnetic field penetration depth $\lambda = \sqrt{\frac{m^*c^2b}{4\pi e^{*2}|a(T)|}}$, as scaling all lengths by this reduces equation (2.11) to a dimensionless form. This provides an approximation of the length over which the magnetic field varies.

Next we imagine placing a large superconductor in a uniform magnetic field. We compare the Gibbs free energy of the Meissner state with zero magnetic field in the core ($B = 0$) to the Gibbs free energy of the normal state with the uniform magnetic field penetrating the material ($B = H$). At a critical magnetic field, H_{c}, these two energies are equal and allow us to find the critical field, H_{c}

$$\frac{H_{\mathrm{c}}^2}{8\pi} = \frac{a^2(T)}{2b}. \tag{2.12}$$

This field provides a convenient scale for the magnetic field. Using this and the length scales defined above, all terms in the free energy may be scaled and the free

energy can be written in a scaleless form. The complete scaling transformations are:

$$\xi = \sqrt{\frac{\hbar^2}{2m^*|a|}}, \qquad\qquad \Psi'(\mathbf{r}') = \sqrt{\frac{b}{|a|}}\Psi(\mathbf{r}),$$

$$\lambda = \sqrt{\frac{m^*c^2b}{4\pi e^{*2}|a|}}, \qquad\qquad \mathbf{A}'(\mathbf{r}') = \frac{\mathbf{A}(\mathbf{r})}{\sqrt{2}H_\mathrm{c}\lambda},$$

$$\frac{H_\mathrm{c}^2}{8\pi} = \frac{a^2}{2b}, \qquad\qquad \mathbf{B}'(\mathbf{r}') = \frac{\mathbf{B}(\mathbf{r})}{\sqrt{2}H_\mathrm{c}},$$

$$\mathbf{r}' = \frac{\mathbf{r}}{\lambda}, \qquad\qquad \mathrm{F}' = \frac{4\pi\mathrm{F}}{H_\mathrm{c}^2},$$

$$\kappa = \frac{\lambda}{\xi}, \qquad\qquad \sigma'_\mathrm{ns} = \frac{4\pi}{\lambda H_\mathrm{c}^2}\sigma_\mathrm{ns}, \qquad (2.13)$$

where σ_ns is the surface free energy to be discussed later.

With these scaling factors, the free energy density may be rewritten as

$$\mathrm{F}_\mathrm{s} = \mathrm{F}_\mathrm{n0} + \left|\left(-\frac{\mathrm{i}}{\kappa}\nabla + \mathbf{A}(\mathbf{r})\right)\Psi(\mathbf{r})\right|^2 - |\Psi(\mathbf{r})|^2 + \frac{1}{2}|\Psi(\mathbf{r})|^4 + \mathbf{B}(\mathbf{r})^2. \qquad (2.14)$$

In this form, the only remaining parameter is κ, the Ginzburg-Landau parameter. The value of this is a property of a material and is the main parameter distinguishing different types of superconductors in this formalism.

With this scaling the GL equations are

$$\left(-\frac{\mathrm{i}}{\kappa}\nabla + \mathbf{A}(\mathbf{r})\right)^2\Psi(\mathbf{r}) - \Psi(\mathbf{r}) + |\Psi(\mathbf{r})|^2\Psi(\mathbf{r}) = 0, \qquad (2.15\mathrm{a})$$

$$\nabla\times\nabla\times\mathbf{A}(\mathbf{r}) + |\Psi(\mathbf{r})|^2\mathbf{A}(\mathbf{r}) + \frac{\mathrm{i}}{2\kappa}\left(\Psi^*(\mathbf{r})\nabla\Psi(\mathbf{r}) - \Psi(\mathbf{r})\nabla\Psi^*(\mathbf{r})\right) = 0, \qquad (2.15\mathrm{b})$$

and the supercurrent becomes

$$\mathbf{j}(\mathbf{r}) = \frac{1}{2\mathrm{i}\kappa}\left(\Psi^*(\mathbf{r})\nabla\Psi(\mathbf{r}) - \Psi(\mathbf{r})\nabla\Psi^*(\mathbf{r})\right) - |\Psi(\mathbf{r})|^2\mathbf{A}(\mathbf{r}). \qquad (2.16)$$

This completes the justification for the GL equations and the transformation to the dimensionless form. Next we will look at some specific cases for the application of these equations.

2.1.2   The Surface Energy

It is possible to define an energy resulting from a surface where a bulk normal material is in contact with a bulk superconductor. This boundary will only be stable if the free energy on either side of the boundary is the same. In this case, far from

the normal-superconductor surface, the Gibbs free energy of the normal material must equal that of the superconductor. This requires

$$G_{n0} - \frac{H_c^2}{8\pi} = G_{s0}, \tag{2.17}$$

which is possible if we apply a critical field to create the normal material. We examine the case of an infinite planar surface between two semi-infinite materials, so that the problem may be reduced to an effective one dimensional problem. We introduce the ansatz solutions

$$\Psi(\mathbf{r}) = f(z),$$
$$\mathbf{A}(\mathbf{r}) = A(z)\hat{\mathbf{e}}_x, \tag{2.18}$$

where $\hat{\mathbf{e}}_x$ is a unit vector in the x direction and we can assume $\Psi(\mathbf{r})$ is real without loss of generality. Then the GL equations may be reduced to the form

$$-\frac{1}{\kappa^2}\frac{\mathrm{d}^2 f(z)}{\mathrm{d}z^2} + A^2(z)f(z) - f(z) + f(z)^3 = 0, \tag{2.19a}$$

$$\frac{\mathrm{d}^2 A(z)}{\mathrm{d}z^2} - f(z)^2 A(z) = 0, \tag{2.19b}$$

along with the boundary conditions

$$
\begin{aligned}
z &\to -\infty, & z &\to \infty, \\
f &= 0, & f &= 1, \\
B_y = \frac{\mathrm{d}A}{\mathrm{d}z} &= \frac{1}{\sqrt{2}}, & A &= 0.
\end{aligned}
\tag{2.20}
$$

The supercurrent associated with this interface can also be calculated as

$$\mathbf{j}(\mathbf{r}) = -f^2(z)A(z)\hat{\mathbf{e}}_x. \tag{2.21}$$

These equations still cannot be solved analytically, and numeric approaches must be used. One approach is to use a finite difference method. An example solution for one choice of κ is shown in figure 2.1. At the far left boundary the order parameter drops to zero and the magnetic field is equal to the critical field, $1/\sqrt{2}$. At the far right boundary the order parameter is at the bulk value of 1, while the magnetic field has decayed to zero.

We can associate an energy with this interface solution by comparing the energy to the energy of a uniform superconductor. The surface free energy is therefore given
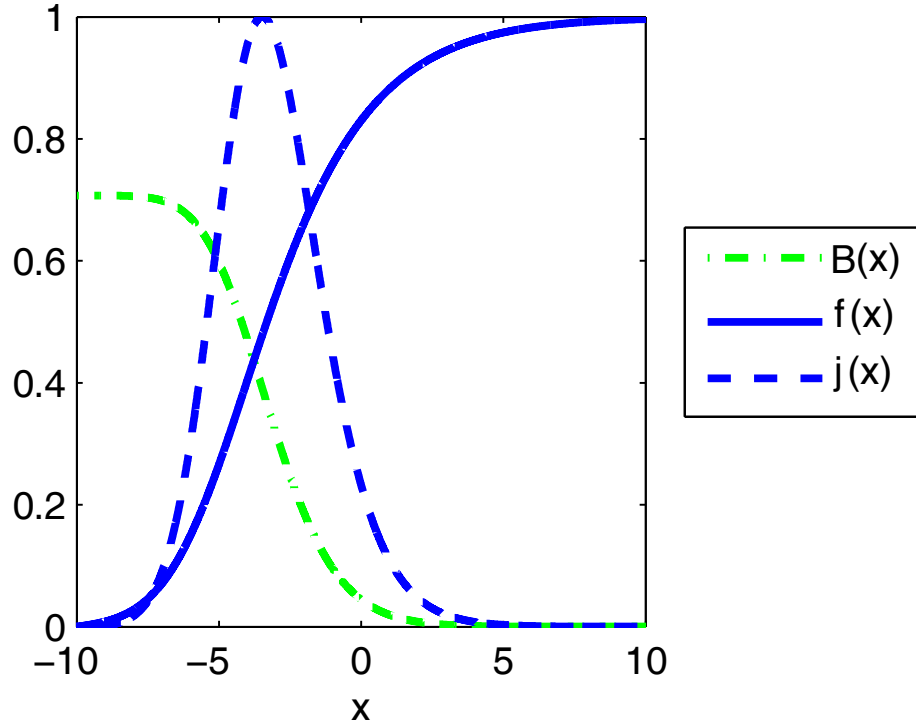
Figure 2.1: A typical interface solution to the GL equations for $\kappa = 0.278$

by the integral [131]

$$
\begin{aligned}
\sigma_{\mathrm{ns}} &= \int_{-\infty}^{\infty} \mathrm{d}z \left[\mathrm{G}(z) - \mathrm{G}_{\mathrm{n0}} + \frac{1}{2} \right] = \int_{-\infty}^{\infty} \mathrm{d}z \left[\mathrm{G}(z) - \mathrm{G}_{\mathrm{s0}} \right] \\
&= \int_{-\infty}^{\infty} \mathrm{d}z \left[- |\Psi(\mathbf{r})|^2 + \frac{1}{2} |\Psi(\mathbf{r})|^4 \right. \\
&\qquad \left. + \left| \left(-\frac{\mathrm{i}}{\kappa} \nabla + \mathbf{A}(\mathbf{r}) \right) \Psi(\mathbf{r}) \right|^2 + \left(\frac{1}{\sqrt{2}} - B_y(\mathbf{r}) \right)^2 \right],
\end{aligned}
\tag{2.22}
$$

where the half comes from adding the energy associated with the application of the critical field. This can be simplified by multiplying equation (2.15a) by $\Psi^*(\mathbf{r})$ and integrating along z to find

$$
\int_{-\infty}^{\infty} \mathrm{d}z \left[- |\Psi(\mathbf{r})|^2 + |\Psi(\mathbf{r})|^4 + \left| \left(-\frac{\mathrm{i}}{\kappa} \nabla + \mathbf{A}(\mathbf{r}) \right) \Psi(\mathbf{r}) \right|^2 \right] = 0.
\tag{2.23}
$$

Subtracting this away from equation (2.22), we find the surface free energy may be expressed as

$$
\sigma_{\mathrm{ns}} = \int_{-\infty}^{\infty} \mathrm{d}z \left[-\frac{1}{2} |f(z)|^4 + \left(\frac{1}{\sqrt{2}} - B_y(z) \right)^2 \right].
\tag{2.24}
$$

The surface free energy is a function of the parameter κ through the dependence of $f(z)$ on κ. Solving the surface equations (equation (2.19)) with varying κ, the

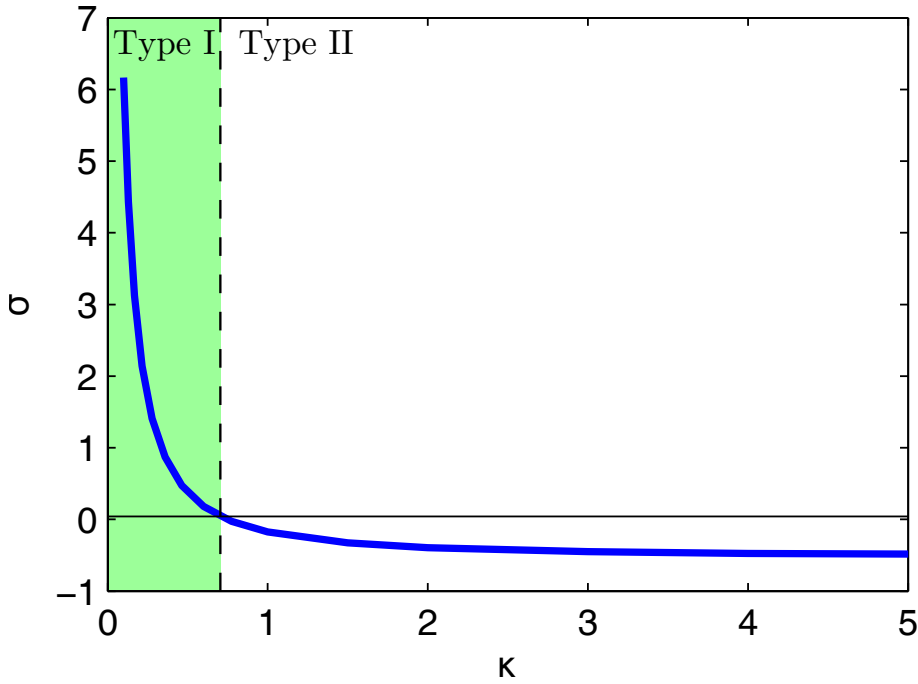**Figure 2.2:** The surface free energy as a function of the GL parameter κ. This shows the cross-over from type I ($\sigma_{\text{ns}} > 0$) to type II ($\sigma_{\text{ns}} < 0$) when $\kappa = 1/\sqrt{2}$, and the asymptotic value of $\sigma_{\text{ns}} = -0.55$ for large κ.

surface free energy can be plotted as a function of κ (figure 2.2). This shows that the critical value of $\kappa = 1/\sqrt{2}$ divides superconductors into two classes, those where the creation of interfaces between the normal state and the superconducting state costs energy, and those where including interfaces lowers the energy. This critical value distinguishes the type I and type II superconductors. However, at this transition point, another nonuniform solution also changes sign and becomes more stable then the interface solution. These are the vortex states.

2.1.3 Vortex States

A novel solution to the GL equations was proposed by Alexei Abrikosov [132]. This new solution is needed to explain the observation that some materials had two critical magnetic fields. Below the first critical field, H_{c1}, these superconductors are in the Meissner state, and above the second critical field, H_{c2}, the material returns to the normal state. However, in between these two critical fields, the magnetic field slowly increases within the material. Abrikosov's explanation was that in this region the normal state was in equilibrium with the superconducting state, with the creation of vortex states. The magnetic flux penetrates the material at localised regions where the material is in the normal state, and these regions are surrounded by a

superconducting current which confine the magnetic field to individual flux lines.

With increasing applied field, these vortices become closely packed and arrange themselves into a triangular lattice, known as an Abrikosov lattice. Upon further increasing the field, the vortices begin to overlap, and eventually the order parameter is unable to recover between the vortices and the material returns to the normal state.

Vortices have been studied intensively since their inception, and there are many good sources which explore these states [22, 133–136].

We first look for a single vortex solution. If a single vortex is placed in a large superconductor, then the vortex system will have cylindrical symmetry, with the origin at the centre of the vortex. To allow this we choose the following ansatz solution in the form

$$\mathbf{A}(\mathbf{r}) = \mathbf{A}(\rho)$$
$$= \frac{nA(\rho)}{\kappa\rho}\hat{\mathbf{e}}_\theta, \tag{2.25a}$$

$$\Psi(\mathbf{r}) = \Psi(\rho)$$
$$= f(\rho)e^{in\theta}, \tag{2.25b}$$

where n is an integer which determines the order of the vortex. This form allows us to reduce the GL equations to the form

$$\frac{d^2 f}{d\rho^2} + \frac{1}{\rho}\frac{df}{d\rho} - \frac{n^2(A-1)^2}{\rho^2}f - \kappa^2 f\left(f^2 - 1\right) = 0, \tag{2.26a}$$

$$\frac{d^2 A}{d\rho^2} - \frac{1}{\rho}\frac{dA}{d\rho} + f^2(1-A) = 0, \tag{2.26b}$$

with the boundary conditions

$$
\begin{aligned}
&\rho \to 0, && \rho \to \infty, \\
&f = 0, && f = 1, \\
&A = 0, && A = 1, \tag{2.27}
\end{aligned}
$$

and the supercurrent around the vortex given by

$$\mathbf{j}(\mathbf{r}) = \frac{n}{\kappa\rho}(1 - A(\rho))f^2(\rho)\hat{\mathbf{e}}_\theta. \tag{2.28}$$

The resulting equations still cannot be solved analytically. However asymptotic results can be obtained. For example, in the limit $\lambda \gg \xi$, we can approximate equation (2.26b) by setting $f = 1$, where the resulting equation is a modified
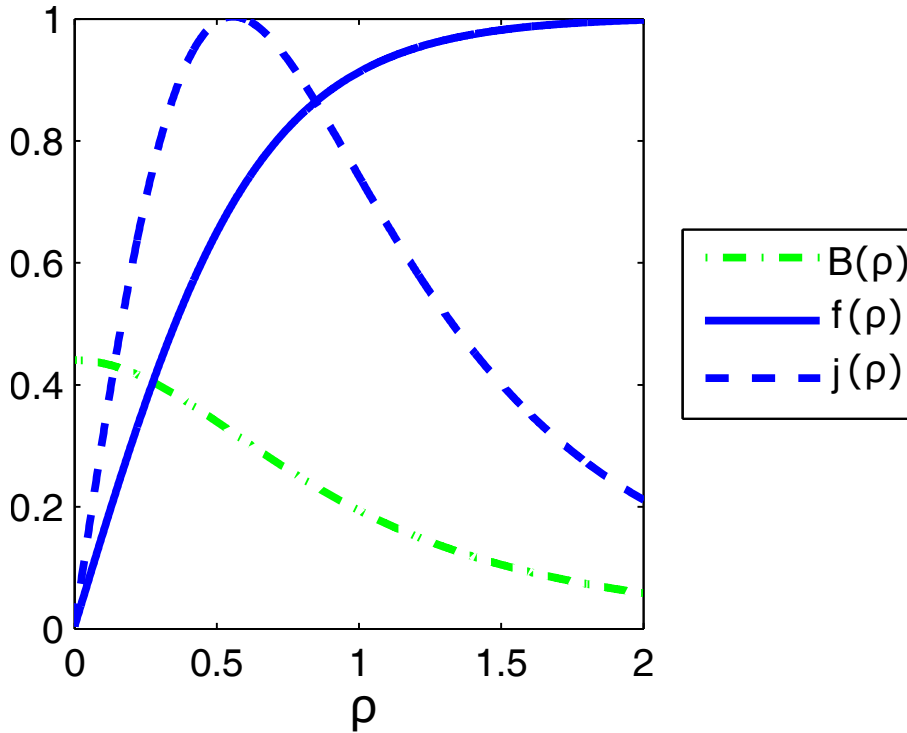
Figure 2.3: A vortex solution to the GL equations for $\kappa = 2.336$

Bessel's equation of order zero. The solution for the resulting magnetic field in this case is

$$B_z(\rho) = K_0(\rho), \tag{2.29}$$

and is a good approximation to the full solution when $\rho \gg \xi$. For a more complete solution, numerical methods must be used. A numerical solution to the coupled equations is presented in figure 2.3. This shows how the order parameter returns to the equilibrium value and the decay of the magnetic field.

Other properties of superconductors, such as the critical fields for type II superconductors, H_{c1} and H_{c2}, the Abrikosov lattice, the jump in the specific heat at the critical temperature, the magnetisation as a function of applied field, etc. can also be obtained from GL theory.

Next we move on from the phenomenological theory of Ginzburg and Landau and consider the microscopic theory of BCS.

2.2 BCS Theory

The BCS theory of Bardeen, Cooper and Schrieffer is the first microscopic theory of superconductivity [32]. The electron-phonon interaction was argued earlier to create

an effective attractive interaction between electrons near the Fermi surface [27], with a cut-off at the scale of the phonon energy, $\hbar\omega_\mathrm{D}$.

In general, the interaction should include a sum over all phonon frequencies and all initial and final state electron momentum states. The leading contribution however comes from electrons with opposite momenta pairing up. Only including interactions between these states, the Hamiltonian becomes much simpler.

There are many treatments of BCS theory [see 137–139]. In the following, we follow closely the treatment by Fetter and Walecka [140]. Converting to real space, the interaction becomes a local interaction between electrons with opposite spins. The BCS grand canonical Hamiltonian is written in real space as

$$
\begin{aligned}
\hat{K}_\mathrm{BCS} = & \sum_\sigma \int \mathrm{d}\mathbf{r}\, \hat{\psi}_\sigma^\dagger(\mathbf{r}) \left(\frac{1}{2m} \left(-\mathrm{i}\hbar\nabla + \frac{e\mathbf{A}(\mathbf{r})}{c} \right)^2 - \mu \right) \hat{\psi}_\sigma(\mathbf{r}) \\
& - g \int \mathrm{d}\mathbf{r}\, \hat{\psi}_\uparrow^\dagger(\mathbf{r})\hat{\psi}_\downarrow^\dagger(\mathbf{r})\hat{\psi}_\downarrow(\mathbf{r})\hat{\psi}_\uparrow(\mathbf{r}),
\end{aligned}
\tag{2.30}
$$

where $\hat{\psi}$ ($\hat{\psi}^\dagger$) is the electron annihilation (creation) operator, m is the electron mass, σ is a spin label (up or down), μ is the chemical potential, and g is the interaction strength.

Taking a mean-field approximation of this Hamiltonian, and neglecting the Hartree-Fock terms (which are expected to be similar in the normal and superconducting states) to find the effective BCS Hamiltonian

$$
\begin{aligned}
\hat{K}_\mathrm{eff} = & \sum_\sigma \int \mathrm{d}\mathbf{r}\, \hat{\psi}_\sigma^\dagger(\mathbf{r}) \left(\frac{1}{2m} \left(-\mathrm{i}\hbar\nabla + \frac{e\mathbf{A}(\mathbf{r})}{c} \right)^2 - \mu \right) \hat{\psi}_\sigma(\mathbf{r}) \\
& - g \int \mathrm{d}\mathbf{r}\, \left(\left\langle \hat{\psi}_\uparrow^\dagger(\mathbf{r})\hat{\psi}_\downarrow^\dagger(\mathbf{r}) \right\rangle \hat{\psi}_\downarrow(\mathbf{r})\hat{\psi}_\uparrow(\mathbf{r}) + \hat{\psi}_\uparrow^\dagger(\mathbf{r})\hat{\psi}_\downarrow^\dagger(\mathbf{r}) \left\langle \hat{\psi}_\downarrow(\mathbf{r})\hat{\psi}_\uparrow(\mathbf{r}) \right\rangle \right),
\end{aligned}
\tag{2.31}
$$

where the angular brackets denote an ensemble average with respect to $\hat{K}_\mathrm{eff}$

$$
\left\langle \hat{O} \right\rangle = \frac{\mathrm{Tr}[e^{-\beta\hat{K}_\mathrm{eff}}\hat{O}]}{\mathrm{Tr}[e^{-\beta\hat{K}_\mathrm{eff}}]}.
\tag{2.32}
$$

We use this to define temperature Heisenberg creation and annihilation operators, which, in analogy to the time-dependent operators, are defined as

$$
\hat{\psi}_{K\uparrow}(\mathbf{r}, t) = e^{\hat{K}_\mathrm{eff}t/\hbar}\hat{\psi}_\uparrow(\mathbf{r})e^{-\hat{K}_\mathrm{eff}t/\hbar},
\tag{2.33a}
$$

$$
\hat{\psi}_{K\downarrow}^\dagger(\mathbf{r}, t) = e^{\hat{K}_\mathrm{eff}t/\hbar}\hat{\psi}_\downarrow^\dagger(\mathbf{r})e^{-\hat{K}_\mathrm{eff}t/\hbar}.
\tag{2.33b}
$$

Note that the imaginary time creation operator is not the Hermitian conjugate of the annihilation operator. From this it is easy to find the equation of motion of these

operators from the commutation relation with the Hamiltonian, which states that, for any operator $\hat{O}$ in the Heisenberg picture, the equation of motion is given by

$$\hbar\frac{\mathrm{d}\hat{O}}{\mathrm{d}t} = \left[\hat{K}_{\mathrm{eff}}, \hat{O}\right]. \tag{2.34}$$

The equation of motion of the creation and annihilation operators is therefore

$$\hbar\frac{\partial\hat{\psi}_{K\uparrow}(\mathbf{r},t)}{\partial t} = -\left[\frac{1}{2m}\left(-\mathrm{i}\hbar\nabla + \frac{e\mathbf{A}(\mathbf{r})}{c}\right)^2 - \mu\right]\hat{\psi}_{K\uparrow}(\mathbf{r},t)$$
$$- g\left\langle\hat{\psi}_{\uparrow}(\mathbf{r})\hat{\psi}_{\downarrow}(\mathbf{r})\right\rangle\hat{\psi}^{\dagger}_{K\downarrow}(\mathbf{r},t), \tag{2.35a}$$

$$\hbar\frac{\partial\hat{\psi}^{\dagger}_{K\downarrow}(\mathbf{r},t)}{\partial t} = \left[\frac{1}{2m}\left(\mathrm{i}\hbar\nabla + \frac{e\mathbf{A}(\mathbf{r})}{c}\right)^2 - \mu\right]\hat{\psi}^{\dagger}_{K\downarrow}(\mathbf{r},t)$$
$$- g\left\langle\hat{\psi}^{\dagger}_{\downarrow}(\mathbf{r})\hat{\psi}^{\dagger}_{\uparrow}(\mathbf{r})\right\rangle\hat{\psi}_{K\uparrow}(\mathbf{r},t). \tag{2.35b}$$

We then define the temperature Green function and the anomalous temperature Green function in the superconducting state.

$$\mathscr{G}(\mathbf{r}t, \mathbf{r}'t') = -\left\langle\mathrm{T}_t\left[\hat{\psi}_{K\uparrow}(\mathbf{r},t)\hat{\psi}^{\dagger}_{K\uparrow}(\mathbf{r}',t')\right]\right\rangle, \tag{2.36a}$$

$$\mathscr{F}(\mathbf{r}t, \mathbf{r}'t') = -\left\langle\mathrm{T}_t\left[\hat{\psi}_{K\uparrow}(\mathbf{r},t)\hat{\psi}_{K\downarrow}(\mathbf{r}',t')\right]\right\rangle, \tag{2.36b}$$

$$\mathscr{F}^{\dagger}(\mathbf{r}t, \mathbf{r}'t') = -\left\langle\mathrm{T}_t\left[\hat{\psi}^{\dagger}_{K\downarrow}(\mathbf{r},t)\hat{\psi}^{\dagger}_{K\uparrow}(\mathbf{r}',t')\right]\right\rangle, \tag{2.36c}$$

where T_t indicates the time ordered product of the operators, where operators acting at earlier times are moved to the right, including the sign change due to any anticommutation relations, but ignoring the right hand side of the anticommutation relations. We also define the superconducting gap function, Δ, implicitly through the definition of the complex conjugate of the gap function

$$\Delta^*(\mathbf{r}) = -g\left\langle\hat{\psi}^{\dagger}_{\downarrow}(\mathbf{r})\hat{\psi}^{\dagger}_{\uparrow}(\mathbf{r})\right\rangle \tag{2.37}$$

$$= g\mathscr{F}^{\dagger}(\mathbf{r}t^+, \mathbf{r}t), \tag{2.38}$$

where t^+ indicates that this time coordinate is evaluated in the limit that it goes to t from above, which is needed to fix the ordering of the operators in the time ordered product.

The existence of the gap function is the main property that determines if a material is superconducting. The definition shows that this gap is the expectation value of having an electron pair at the location $\mathbf{r}$. We will see that this function is called the gap because it is the magnitude of a gap which opens up in the single particle excitation spectrum.

Taking the time derivative of the Green functions and using the previously calculated equations of motion for the creation and annihilation operators immediately allow us to find the equations of motion for these Green functions.

$$\left[-\hbar \frac{\partial}{\partial t} - \frac{1}{2m} \left(-\mathrm{i}\hbar\nabla + \frac{e\mathbf{A}(\mathbf{r})}{c} \right)^2 + \mu \right] \mathscr{G}(\mathbf{r}t, \mathbf{r}'t')$$

$$+ \Delta(\mathbf{r})\mathscr{F}^\dagger(\mathbf{r}t, \mathbf{r}'t') = \hbar\delta(t - t')\delta(\mathbf{r} - \mathbf{r}'),$$

(2.39a)

$$\left[\hbar \frac{\partial}{\partial t} - \frac{1}{2m} \left(-\mathrm{i}\hbar\nabla + \frac{e\mathbf{A}(\mathbf{r})}{c} \right)^2 - \mu \right] \mathscr{F}^\dagger(\mathbf{r}t, \mathbf{r}'t') = \Delta^*(\mathbf{r})\mathscr{G}(\mathbf{r}t, \mathbf{r}'t'). \quad (2.39b)$$

We therefore have a pair of coupled differential equations.

2.2.1 Solutions

To find solutions of these equations, we first note that the Green functions are antiperiodic with antiperiod $\beta\hbar$. To see this, we choose $0 < t' < \beta\hbar$ and evaluate the Green function at $t = 0$.

$$\begin{aligned}
\mathscr{G}(\mathbf{r}0, \mathbf{r}'t') &= -\mathrm{e}^{\beta\Omega}\mathrm{Tr}\left\{ \mathrm{e}^{-\beta\hat{K}_{\mathrm{eff}}} \mathrm{T}_t \left[\hat{\psi}_{K\uparrow}(\mathbf{r}0)\hat{\psi}_{K\uparrow}^\dagger(\mathbf{r}'t') \right] \right\} \\
&= \mathrm{e}^{\beta\Omega}\mathrm{Tr}\left\{ \mathrm{e}^{-\beta\hat{K}_{\mathrm{eff}}} \hat{\psi}_{K\uparrow}^\dagger(\mathbf{r}'t')\hat{\psi}_{K\uparrow}(\mathbf{r}0) \right\} \\
&= \mathrm{e}^{\beta\Omega}\mathrm{Tr}\left\{ \hat{\psi}_{K\uparrow}(\mathbf{r}0)\mathrm{e}^{-\beta\hat{K}_{\mathrm{eff}}} \hat{\psi}_{K\uparrow}^\dagger(\mathbf{r}'t') \right\} \\
&= \mathrm{e}^{\beta\Omega}\mathrm{Tr}\left\{ \hat{\psi}_\uparrow(\mathbf{r})\mathrm{e}^{-\beta\hat{K}_{\mathrm{eff}}} \hat{\psi}_{K\uparrow}^\dagger(\mathbf{r}'t') \right\} \\
&= \mathrm{e}^{\beta\Omega}\mathrm{Tr}\left\{ \mathrm{e}^{-\beta\hat{K}_{\mathrm{eff}}}\mathrm{e}^{\beta\hat{K}_{\mathrm{eff}}} \hat{\psi}_\uparrow(\mathbf{r})\mathrm{e}^{-\beta\hat{K}_{\mathrm{eff}}} \hat{\psi}_{K\uparrow}^\dagger(\mathbf{r}'t') \right\} \\
&= \mathrm{e}^{\beta\Omega}\mathrm{Tr}\left\{ \mathrm{e}^{-\beta\hat{K}_{\mathrm{eff}}} \hat{\psi}_\uparrow(\mathbf{r}(\beta\hbar))\hat{\psi}_{K\uparrow}^\dagger(\mathbf{r}'t') \right\} \\
&= -\mathscr{G}(\mathbf{r}(\beta\hbar), \mathbf{r}'t').
\end{aligned}$$

(2.40)

In the case where the Hamiltonian is time-independent (the superconductor is in a static applied magnetic field), the Green functions only depend on the difference $t - t'$. Using the antiperiodic property, we can then make the Fourier expansion with odd coefficients

$$\mathscr{G}(\mathbf{r}t, \mathbf{r}'t') = (\beta\hbar)^{-1} \sum_n \mathrm{e}^{(-\mathrm{i}\omega_n(t-t'))}\mathscr{G}_{\omega_n}(\mathbf{r}, \mathbf{r}'), \quad (2.41a)$$

$$\mathscr{F}^\dagger(\mathbf{r}t, \mathbf{r}'t') = (\beta\hbar)^{-1} \sum_n \mathrm{e}^{(-\mathrm{i}\omega_n(t-t'))}\mathscr{F}_{\omega_n}^\dagger(\mathbf{r}, \mathbf{r}'), \quad (2.41b)$$

where $\omega_n = (2n + 1)\pi/\beta\hbar$ is the fermionic Matsubara frequency which guarantees the antiperiodicity. If we also look at the case where there is no applied magnetic field, then the Green functions are also translation invariant and depend only on the

difference $\mathbf{r} - \mathbf{r}'$. We can therefore write these as a function of the difference between these two points, and then perform a Fourier transform.

$$\mathscr{G}_{\omega_n}(\mathbf{r}) = \frac{1}{(2\pi)^3} \int \mathrm{d}\mathbf{k}\, \mathrm{e}^{\mathrm{i}\mathbf{k}.\mathbf{r}} \mathscr{G}_{\omega_n}(\mathbf{k}), \tag{2.42a}$$

$$\mathscr{F}^{\dagger}_{\omega_n}(\mathbf{r}) = \frac{1}{(2\pi)^3} \int \mathrm{d}\mathbf{k}\, \mathrm{e}^{\mathrm{i}\mathbf{k}.\mathbf{r}} \mathscr{F}^{\dagger}_{\omega_n}(\mathbf{k}). \tag{2.42b}$$

Defining $\varepsilon_{\mathbf{k}} = \frac{\hbar^2 k^2}{2m} - \mu$, the differential equations reduce to algebraic equations

$$[\mathrm{i}\hbar\omega_n - \varepsilon_{\mathbf{k}}]\, \mathscr{G}_{\omega_n}(\mathbf{k}) + \Delta \mathscr{F}^{\dagger}_{\omega_n}(\mathbf{k}) = \hbar, \tag{2.43a}$$

$$[-\mathrm{i}\hbar\omega_n - \varepsilon_{\mathbf{k}}]\, \mathscr{F}^{\dagger}_{\omega_n}(\mathbf{k}) - \Delta^* \mathscr{G}_{\omega_n}(\mathbf{k}) = 0. \tag{2.43b}$$

These are easily solved

$$\mathscr{G}_{\omega_n}(\mathbf{k}) = \frac{-\hbar(\mathrm{i}\hbar\omega_n + \varepsilon_{\mathbf{k}})}{\hbar^2\omega_n^2 + \varepsilon_{\mathbf{k}}^2 + |\Delta|^2}, \tag{2.44a}$$

$$\mathscr{F}^{\dagger}_{\omega_n}(\mathbf{k}) = \frac{\hbar\Delta^*}{\hbar^2\omega_n^2 + \varepsilon_{\mathbf{k}}^2 + |\Delta|^2}. \tag{2.44b}$$

Using the definition for the gap Δ (equation (2.38)), we find the self-consistent gap equation

$$\Delta = \frac{g}{\beta\hbar} \sum_n \int \mathrm{d}\mathbf{k}\, \frac{1}{(2\pi)^3} \frac{\hbar\Delta}{\hbar^2\omega_n^2 + \varepsilon_{\mathbf{k}}^2 + |\Delta|^2} \tag{2.45}$$

$$= g \int \mathrm{d}\mathbf{k}\, \frac{1}{(2\pi)^3} \frac{\Delta}{2\sqrt{\varepsilon_{\mathbf{k}}^2 + |\Delta|^2}} \tanh\left(\frac{\sqrt{\varepsilon_{\mathbf{k}}^2 + |\Delta|^2}}{2k_{\mathrm{B}}T}\right) \tag{2.46}$$

$$\approx gN(0) \int_{\infty}^{\infty} \mathrm{d}\varepsilon\, \frac{\Delta}{2\sqrt{\varepsilon^2 + |\Delta|^2}} \tanh\left(\frac{\sqrt{\varepsilon^2 + |\Delta|^2}}{2k_{\mathrm{B}}T}\right), \tag{2.47}$$

where $N(0)$ is the density of states at the Fermi surface. However this integral diverges logarithmically. To produce a meaningful result, the integral must be cut off. We can perform the cut off by recalling that the interaction is mediated by an exchange of phonons. This has a maximum energy given by the Debye energy, $\hbar\omega_{\mathrm{D}}$. Therefore only states within this energy of the Fermi surface participate in the interaction. The integrand is also symmetric in the integration variable, so we can write this as

$$\Delta = gN(0) \int_0^{\hbar\omega_{\mathrm{D}}} \mathrm{d}\varepsilon\, \frac{\Delta}{\sqrt{\varepsilon^2 + |\Delta|^2}} \tanh\left(\frac{\sqrt{\varepsilon^2 + |\Delta|^2}}{2k_{\mathrm{B}}T}\right). \tag{2.48}$$

Alternatively it is possible to perform renormalisation of the interaction strength g to remove the divergent contribution.

Two important limits of this equation are $T \to 0$ and $\Delta \to 0$. In the first case we find

$$\Delta_0 = gN(0) \int_0^{\hbar\omega_{\mathrm{D}}} \mathrm{d}\varepsilon \, \frac{\Delta_0}{\sqrt{\varepsilon^2 + |\Delta_0|^2}} \tag{2.49}$$

$$= \Delta_0 gN(0) \ln \left(\frac{\sqrt{\Delta_0^2 + \hbar\omega_{\mathrm{D}}^2} + \hbar\omega_{\mathrm{D}}}{\Delta_0} \right), \tag{2.50}$$

$$\therefore \Delta_0 = \frac{\hbar\omega_{\mathrm{D}}}{\sinh\left(\frac{1}{gN(0)}\right)} \tag{2.51}$$

$$\approx 2\hbar\omega_{\mathrm{D}} \exp\left(-\frac{1}{gN(0)}\right), \quad \hbar\omega_{\mathrm{D}} \gg \Delta. \tag{2.52}$$

Note that the condition $\hbar\omega_{\mathrm{D}} \gg \Delta$ is equivalent to $gN(0) \ll 1$. Since BCS theory only applies to superconductivity in the weak coupling regime, this approximation is valid. The second limit, $\Delta \to 0$, allows us to simplify the integral as

$$1 = gN(0) \int_0^{\hbar\omega_{\mathrm{D}}} \mathrm{d}\varepsilon \, \frac{1}{\varepsilon} \tanh\left(\frac{\varepsilon}{2k_{\mathrm{B}}T_{\mathrm{c}}}\right) \tag{2.53}$$

$$\approx \ln\left(\frac{2\hbar\omega_{\mathrm{D}}\mathrm{e}^{\Gamma}}{k_{\mathrm{B}}T_{\mathrm{c}}\pi}\right), \tag{2.54}$$

$$\therefore k_{\mathrm{B}}T_{\mathrm{c}} = \frac{2\hbar\omega_{\mathrm{D}}\mathrm{e}^{\Gamma}}{\pi} \exp\left(-\frac{1}{gN(0)}\right), \tag{2.55}$$

with $\Gamma \approx 0.5772$ the Euler-Mascheroni constant. Comparing these two limits we see that the ratio does not depend on the parameters of the theory, giving the universal BCS value

$$\frac{\Delta_0}{k_{\mathrm{B}}T_{\mathrm{c}}} = \pi\mathrm{e}^{-\Gamma} \approx 1.76388. \tag{2.56}$$

There are many other properties that can be evaluated within the BCS theory. These include thermodynamic properties, such as the critical field, heat capacity, entropy and others. The current can also be examined for a weak field, and this can be used to show that this theory contains the Meissner effect. Some of these will be shown later in chapter 3 in the generalised multiband theory.

2.3 Derivation of Ginzburg-Landau Equations from BCS

GL theory is a phenomenological theory known for its success for practical applications. BCS theory is a microscopic theory that can explain the basis of superconductivity from the formation of Cooper pairs. Therefore there was a need to find the connection between GL theory and BCS.

In 1959, Gor'kov [36] showed that the phenomenological GL theory can be derived from the BCS theory as an expansion near T_c with Δ assumed small, and a slowly varying vector potential. In this way the order parameter of GL theory, $\Psi(\mathbf{r})$, was directly related to the superconducting gap, $\Delta(\mathbf{r})$, from BCS theory. Since in chapter 4 we will use this technique to extend the GL theory, we will include the details of this connection here and omit most of the details later.

To perform the connection, we begin with the equations of motion for the Green function $\mathscr{G}$ and anomalous Green function $\mathscr{F}^\dagger$.

$$\left[i\hbar\omega_n + \frac{\hbar^2}{2m}\left(\nabla + \frac{ie\mathbf{A}(\mathbf{r})}{\hbar c}\right)^2 + \mu \right]\mathscr{G}_{\omega_n}(\mathbf{r}, \mathbf{r}') + \Delta(\mathbf{r})\mathscr{F}^\dagger_{\omega_n}(\mathbf{r}, \mathbf{r}') = \hbar\delta^3(\mathbf{r} - \mathbf{r}'),$$

$$(2.57\mathrm{a})$$

$$\left[-i\hbar\omega_n + \frac{\hbar^2}{2m}\left(\nabla + \frac{ie\mathbf{A}(\mathbf{r})}{\hbar c}\right)^2 + \mu \right]\mathscr{F}^\dagger_{\omega_n}(\mathbf{r}, \mathbf{r}') - \Delta^*(\mathbf{r})\mathscr{G}_{\omega_n}(\mathbf{r}, \mathbf{r}') = 0. \qquad (2.57\mathrm{b})$$

We also introduce the temperature Green function for electrons in the normal state, which satisfies the equation of motion

$$\left[i\hbar\omega_n + \frac{\hbar^2}{2m}\left(\nabla + \frac{ie\mathbf{A}(\mathbf{r})}{\hbar c}\right)^2 + \mu \right]\mathcal{G}_{\omega_n}(\mathbf{r}, \mathbf{r}') = \hbar\delta^3(\mathbf{r} - \mathbf{r}'), \qquad (2.58\mathrm{a})$$

$$\left[-i\hbar\omega_n + \frac{\hbar^2}{2m}\left(\nabla - \frac{ie\mathbf{A}(\mathbf{r})}{\hbar c}\right)^2 + \mu \right]\widetilde{\mathcal{G}}_{\omega_n}(\mathbf{r}, \mathbf{r}') = \hbar\delta^3(\mathbf{r} - \mathbf{r}'), \qquad (2.58\mathrm{b})$$

where $\widetilde{\mathcal{G}}_{\omega_n}(\mathbf{r}, \mathbf{r}') = \mathcal{G}_{-\omega_n}(\mathbf{r}', \mathbf{r})$.

The original differential equations can then be written as a pair of coupled integral equations,

$$\mathscr{G}_{\omega_n}(\mathbf{r}, \mathbf{r}') = \mathcal{G}_{\omega_n}(\mathbf{r}, \mathbf{r}') - \hbar^{-1}\int d\mathbf{y}\, \mathcal{G}_{\omega_n}(\mathbf{r}, \mathbf{y})\Delta(\mathbf{y})\mathscr{F}^\dagger_{\omega_n}(\mathbf{y}, \mathbf{r}'), \qquad (2.59\mathrm{a})$$

$$\mathscr{F}^\dagger_{\omega_n}(\mathbf{r}, \mathbf{r}') = \hbar^{-1}\int d\mathbf{y}\, \widetilde{\mathcal{G}}_{\omega_n}(\mathbf{r}, \mathbf{y})\Delta^*(\mathbf{y})\mathscr{G}_{\omega_n}(\mathbf{y}, \mathbf{r}'). \qquad (2.59\mathrm{b})$$

By substituting these equations back into the differential equations (equation (2.57)) and using the fact that the normal Green functions satisfy their differential equations (equation (2.58)) we see that these integral equations satisfy the original differential equations.

These linear coupled integral equations can be written as the uncoupled nonlinear

integral equations

$$\mathcal{G}_{\omega_n}(\mathbf{r}, \mathbf{r}') = \mathcal{G}_{\omega_n}(\mathbf{r}, \mathbf{r}')$$
$$- \hbar^{-2} \int d\mathbf{y} \int d\mathbf{z}\, \mathcal{G}_{\omega_n}(\mathbf{r}, \mathbf{y}) \Delta(\mathbf{y}) \widetilde{\mathcal{G}}_{\omega_n}(\mathbf{y}, \mathbf{z}) \Delta^*(\mathbf{z}) \mathcal{G}_{\omega_n}(\mathbf{z}, \mathbf{r}'), \tag{2.60a}$$

$$\mathscr{F}^\dagger_{\omega_n}(\mathbf{r}, \mathbf{r}') = \hbar^{-1} \int d\mathbf{y}\, \widetilde{\mathcal{G}}_{\omega_n}(\mathbf{r}, \mathbf{y}) \Delta^*(\mathbf{y}) \mathcal{G}_{\omega_n}(\mathbf{y}, \mathbf{r}')$$
$$- \hbar^{-2} \int d\mathbf{y} \int d\mathbf{z}\, \widetilde{\mathcal{G}}_{\omega_n}(\mathbf{r}, \mathbf{y}) \Delta^*(\mathbf{y}) \mathcal{G}_{\omega_n}(\mathbf{y}, \mathbf{z}) \Delta(\mathbf{z}) \mathscr{F}^\dagger_{\omega_n}(\mathbf{z}, \mathbf{r}'). \tag{2.60b}$$

To proceed, it is assumed that $\Delta \ll \pi k_{\mathrm{B}} T$ (the factor originates from $\Delta \ll \hbar \omega_n, \forall n$). This assumption holds close to the critical temperature T_{c}. With this assumption, we can perform an expansion in small Δ, and truncate the resulting expression at order Δ^3. With this approximation, the Green functions become

$$\mathcal{G}_{\omega_n}(\mathbf{r}, \mathbf{r}') = \mathcal{G}_{\omega_n}(\mathbf{r}, \mathbf{r}')$$
$$- \hbar^{-2} \int d\mathbf{y} \int d\mathbf{z}\, \mathcal{G}_{\omega_n}(\mathbf{r}, \mathbf{y}) \Delta(\mathbf{y}) \widetilde{\mathcal{G}}_{\omega_n}(\mathbf{y}, \mathbf{z}) \Delta^*(\mathbf{z}) \mathcal{G}_{\omega_n}(\mathbf{z}, \mathbf{r}'), \tag{2.61a}$$

$$\mathscr{F}^\dagger_{\omega_n}(\mathbf{r}, \mathbf{r}') = \hbar^{-1} \int d\mathbf{y}\, \widetilde{\mathcal{G}}_{\omega_n}(\mathbf{r}, \mathbf{y}) \Delta^*(\mathbf{y}) \mathcal{G}_{\omega_n}(\mathbf{y}, \mathbf{r}')$$
$$- \hbar^{-3} \int d\mathbf{y} \int d\mathbf{z} \int d\mathbf{w}\, \widetilde{\mathcal{G}}_{\omega_n}(\mathbf{r}, \mathbf{y}) \Delta^*(\mathbf{y}) \mathcal{G}_{\omega_n}(\mathbf{y}, \mathbf{z}) \tag{2.61b}$$
$$\times \Delta(\mathbf{z}) \widetilde{\mathcal{G}}_{\omega_n}(\mathbf{z}, \mathbf{w}) \Delta^*(\mathbf{w}) \mathcal{G}_{\omega_n}(\mathbf{w}, \mathbf{r}').$$

Putting equation (2.61b) back into the definition for the superconducting gap (equation (2.38)) we get the self-consistent gap equation

$$g^{-1} \Delta^*(\mathbf{r}) = \int d\mathbf{y}\, Q(\mathbf{r}, \mathbf{y}) \Delta^*(\mathbf{y})$$
$$+ \int d\mathbf{y} \int d\mathbf{z} \int d\mathbf{w}\, R(\mathbf{r}, \mathbf{y}, \mathbf{z}, \mathbf{w}) \Delta^*(\mathbf{y}) \Delta(\mathbf{z}) \Delta^*(\mathbf{w}), \tag{2.62}$$

with the kernels given by

$$Q(\mathbf{r}, \mathbf{y}) = \frac{1}{\beta \hbar^2} \sum_n \widetilde{\mathcal{G}}_{\omega_n}(\mathbf{r}, \mathbf{y}) \mathcal{G}_{\omega_n}(\mathbf{y}, \mathbf{r}), \tag{2.63a}$$

$$R(\mathbf{r}, \mathbf{y}, \mathbf{z}, \mathbf{w}) = \frac{1}{\beta \hbar^4} \sum_n \widetilde{\mathcal{G}}_{\omega_n}(\mathbf{r}, \mathbf{y}) \mathcal{G}_{\omega_n}(\mathbf{y}, \mathbf{z}) \widetilde{\mathcal{G}}_{\omega_n}(\mathbf{z}, \mathbf{w}) \mathcal{G}_{\omega_n}(\mathbf{w}, \mathbf{r}). \tag{2.63b}$$

To bound the behaviour of these kernels we need to assume that $T_{\mathrm{c}} - T \ll T_{\mathrm{c}}$, since then Δ and $\mathbf{A}$ vary slowly over the range of the kernels. With the additional assumption that the magnetic field varies with a length scale $\lambda(T) \gg k_{\mathrm{F}}^{-1}$, then the leading contribution from the magnetic field will appear as a slowly varying phase factor

$$\mathcal{G}_{\omega_n}(\mathbf{r}, \mathbf{r}') = \exp(i\varphi(\mathbf{r}, \mathbf{r}')) \mathcal{G}^0_{\omega_n}(\mathbf{r} - \mathbf{r}'), \tag{2.64}$$

where $\mathcal{G}^0_{\omega_n}(\mathbf{r} - \mathbf{r}')$ is the normal Green function in the absence of an applied magnetic field, which only depends on the difference $\mathbf{r} - \mathbf{r}'$. The Fourier transform of this Green function, $\mathcal{G}^0_{\omega_n}$, can easily be found by taking the Fourier transform of equation (2.58a) with $\mathbf{A}(\mathbf{r}) = 0$, and solving the resulting algebraic equation. The result is the simple fraction

$$\mathcal{G}^0_{\omega_n}(\mathbf{k}) = \frac{\hbar}{\mathrm{i}\hbar\omega_n - \varepsilon_{\mathbf{k}}}, \tag{2.65}$$

which can be transformed back to find the real space Green function. The phase factor in the presence of magnetic field (equation (2.64)) is then chosen so that the leading order term in $\nabla\varphi(\mathbf{r}, \mathbf{r}')$ cancels the leading order term in $\mathbf{A}(\mathbf{r})$ when this is placed in the normal Green function equations (equation (2.58)). Additionally the interaction with the magnetic field should have no effect on the local correlation function ($\mathbf{r} = \mathbf{r}'$). These conditions give two equations.

$$\varphi(\mathbf{r}, \mathbf{r}) = 0, \tag{2.66a}$$

$$\left(\nabla\varphi(\mathbf{r}, \mathbf{r}') + \frac{e\mathbf{A}(\mathbf{r})}{\hbar c}\right) \cdot (\mathbf{r} - \mathbf{r}') = 0. \tag{2.66b}$$

Finally, φ should be antisymmetric in $\mathbf{r}$ and $\mathbf{r}'$. This is enough to find the solution

$$\varphi(\mathbf{r}, \mathbf{r}') = -\frac{e}{2\hbar c}\left(\mathbf{A}(\mathbf{r}) + \mathbf{A}(\mathbf{r}')\right) \cdot (\mathbf{r} - \mathbf{r}'). \tag{2.67}$$

Since the normal Green function, $\mathcal{G}$, has been split into a phase factor and a Green function that is independent of the field, the kernel Q can also be separated into similar terms

$$Q(\mathbf{r}, \mathbf{y}) = \frac{1}{\beta\hbar^2} \sum_n \exp\left(2\mathrm{i}\varphi(\mathbf{r}, \mathbf{y})\right) \widetilde{\mathcal{G}}^0_{\omega_n}(\mathbf{r} - \mathbf{y})\mathcal{G}^0_{\omega_n}(\mathbf{r} - \mathbf{y})$$

$$= \exp\left(2\mathrm{i}\varphi(\mathbf{r}, \mathbf{y})\right) Q^0(\mathbf{y} - \mathbf{r}). \tag{2.68}$$

Returning to the full form for the integral (equation (2.62)), we make the change of coordinates to $\mathbf{z} = \mathbf{y} - \mathbf{r}$. The exponential is expanded in powers of φ, and we perform a Taylor series of the resultant expression around $z = 0$. This is valid since $Q^0(\mathbf{z})$ decays exponentially such that only within the range of the Pippard coherence

length ($z \lesssim \xi_0 = \hbar v_{\mathrm{F}}/\pi k_{\mathrm{B}} T_{\mathrm{c}}$) contributes significantly to the integral.

$$
\begin{aligned}
\int \mathrm{d}\mathbf{y}\, Q(\mathbf{r}, \mathbf{y})\Delta^*(\mathbf{y}) &= \int \mathrm{d}\mathbf{z}\, Q^0(\mathbf{z}) \exp\left[-\frac{\mathrm{i}e}{\hbar c}\left(\mathbf{A}(\mathbf{r}) + \mathbf{A}(\mathbf{r}+\mathbf{z})\right)\cdot\mathbf{z}\right]\Delta^*(\mathbf{r}+\mathbf{z}) \\
&= \int \mathrm{d}\mathbf{z}\, Q^0(\mathbf{z})\left[1 - \frac{\mathrm{i}e}{\hbar c}\left(\mathbf{A}(\mathbf{r}) + \mathbf{A}(\mathbf{r}+\mathbf{z})\right)\cdot\mathbf{z}\right. \\
&\quad \left. - \frac{1}{2}\left(\frac{e}{\hbar c}\right)^2\left(\left(\mathbf{A}(\mathbf{r}) + \mathbf{A}(\mathbf{r}+\mathbf{z})\right)\cdot\mathbf{z}\right)^2\right]\Delta^*(\mathbf{r}+\mathbf{z}) \\
&= \Delta^*(\mathbf{r})\int \mathrm{d}\mathbf{z}\, Q^0(\mathbf{z}) \\
&\quad + \frac{1}{6}\left[\nabla - \frac{2\mathrm{i}e\mathbf{A}(\mathbf{r})}{\hbar c}\right]^2\Delta^*(\mathbf{r})\int \mathrm{d}\mathbf{z}\, \mathbf{z}^2 Q^0(\mathbf{z}).
\end{aligned} \tag{2.69}
$$

There are now two remaining integrals to perform for this term. The first term is equivalent to the BCS integral in the limit $\Delta \to 0$. This integral diverges logarithmically and must be cut off in momentum space at the Debye frequency.

$$
\begin{aligned}
\int \mathrm{d}\mathbf{z}\, Q^0(\mathbf{z}) &= \frac{1}{\beta\hbar^2}\int \mathrm{d}\mathbf{k}\sum_n \tilde{\mathcal{G}}^0_{\omega_n}(\mathbf{k})\mathcal{G}^0_{\omega_n}(\mathbf{k}) \\
&= \frac{1}{\beta\hbar^2}\int \mathrm{d}\mathbf{k}\sum_n \frac{1}{(\hbar\omega_n)^2 + \varepsilon_{\mathbf{k}}^2} \\
&= N(0)\int_0^{\hbar\omega_{\mathrm{D}}} \mathrm{d}\varepsilon\, \frac{1}{\varepsilon}\tanh\left(\frac{\varepsilon}{2k_{\mathrm{B}}T}\right) \\
&\approx N(0)\ln\left(\frac{2\hbar\omega_{\mathrm{D}}\mathrm{e}^{\Gamma}}{\pi k_{\mathrm{B}}T}\right) \\
&= N(0)\ln\left(\frac{T_{\mathrm{c}}}{T}\right) + N(0)\ln\left(\frac{2\hbar\omega_{\mathrm{D}}\mathrm{e}^{\Gamma}}{\pi k_{\mathrm{B}}T_{\mathrm{c}}}\right) \tag{2.70} \\
&\approx N(0)\left(1 - \frac{T}{T_{\mathrm{c}}}\right) + g^{-1}, \tag{2.71}
\end{aligned}
$$

where the defining equation for T_{c} from BCS theory, $1 = gN(0)\ln(2\hbar\omega_{\mathrm{D}}\mathrm{e}^{\Gamma}/\pi k_{\mathrm{B}}T_{\mathrm{c}})$ (equation (2.54)), has been used, and the logarithm has been expanded near $T = T_{\mathrm{c}}$.

The second integral in equation (2.69) does not have the divergence issues and decays sufficiently fast at large $\mathbf{k}$ so the integral can be evaluated without a cut-off. First, the Green function is evaluated as a function of position

$$
\begin{aligned}
\mathcal{G}^0_{\omega_n}(\mathbf{r}) &= \frac{\hbar}{(2\pi)^3}\int \mathrm{d}\mathbf{k}\, \frac{\exp(\mathrm{i}\mathbf{k}\cdot\mathbf{r})}{\mathrm{i}\hbar\omega_n - \varepsilon_{\mathbf{k}}} \\
&\approx \frac{\hbar N(0)}{k_{\mathrm{F}}r}\int_{-\infty}^{\infty} \mathrm{d}\varepsilon\, \frac{1}{\mathrm{i}\hbar\omega_n - \varepsilon}\sin\left(k_{\mathrm{F}}r + \frac{\varepsilon r}{\hbar v_{\mathrm{F}}}\right) \\
&= \frac{\pi\hbar N(0)}{k_{\mathrm{F}}r}\exp\left[\mathrm{i}k_{\mathrm{F}}r\,\mathrm{sign}(\omega_n) - \frac{|\omega_n|\,r}{v_{\mathrm{F}}}\right]. \tag{2.72}
\end{aligned}
$$

This form of the Green function is then used to find an explicit form for the kernel, Q^0

$$
\begin{aligned}
Q^0(\mathbf{r}) &= \frac{1}{\beta\hbar^2}\sum_n \tilde{\mathcal{G}}^0_{\omega_n}(\mathbf{r})\mathcal{G}^0_{\omega_n}(\mathbf{r}) \\
&= \left(\frac{\pi N(0)}{k_{\mathrm{F}}r}\right)^2 \frac{1}{\beta}\sum_n \exp\left[-\frac{2\,|\omega_n|\,r}{v_{\mathrm{F}}}\right] \\
&= \left(\frac{\pi N(0)}{k_{\mathrm{F}}r}\right)^2 \frac{1}{\beta\sinh\left(2\pi r/\beta\hbar v_{\mathrm{F}}\right)}.
\end{aligned}
\tag{2.73}
$$

With this, the second integral can be performed directly.

$$
\begin{aligned}
\int \mathrm{d}\mathbf{z}\,\mathbf{z}^2 Q^0(\mathbf{z}) &= \left(\frac{\pi N(0)}{k_{\mathrm{F}}}\right)^2 \frac{1}{\beta}\int \mathrm{d}\mathbf{z}\,\frac{1}{\sinh\left(2\pi\,|\mathbf{z}|\,/\beta\hbar v_{\mathrm{F}}\right)} \\
&= N(0)\frac{4\pi^3}{k_{\mathrm{F}}^2}\frac{mk_{\mathrm{F}}}{2\pi^2\hbar^2}\frac{1}{\beta}\left(\frac{\beta\hbar v_{\mathrm{F}}}{2\pi}\right)^3\int_0^\infty \mathrm{d}y\,y^2\frac{1}{\sinh\left(y\right)} \\
&= \frac{7}{8}N(0)\left(\frac{\hbar v_{\mathrm{F}}}{\pi k_{\mathrm{B}}T_{\mathrm{c}}}\right)^2\zeta(3),
\end{aligned}
\tag{2.74}
$$

where we have set $T \approx T_{\mathrm{c}}$ in the last line.

We now have everything we need for the first term. For the second term in equation (2.62), we note that the term is cubic in Δ, which is a small nonlinear correction. This term is evaluated to lowest order, setting $\mathcal{G} \approx \mathcal{G}^0$, $\Delta(\mathbf{y}) \approx \Delta(\mathbf{r})$, and $T \approx T_{\mathrm{c}}$.

$$
\begin{aligned}
\int \mathrm{d}\mathbf{y}\int \mathrm{d}\mathbf{z}\int \mathrm{d}\mathbf{w}\,R(\mathbf{r},\mathbf{y},\mathbf{z},\mathbf{w})&\Delta^*(\mathbf{y})\Delta(\mathbf{z})\Delta^*(\mathbf{w}) \\
&= \Delta^*(\mathbf{r})\,|\Delta(\mathbf{r})|^2\int \mathrm{d}\mathbf{y}\int \mathrm{d}\mathbf{z}\int \mathrm{d}\mathbf{w}\,R(\mathbf{r},\mathbf{y},\mathbf{z},\mathbf{w}),
\end{aligned}
\tag{2.75}
$$

and, concentrating on the remaining integral,

$$
\begin{aligned}
\int \mathrm{d}\mathbf{y}\int \mathrm{d}\mathbf{z}\int \mathrm{d}\mathbf{w}\,R(\mathbf{r},\mathbf{y},\mathbf{z},\mathbf{w}) &= -\frac{1}{\beta_c\hbar^4}\frac{1}{(2\pi)^3}\int \mathrm{d}\mathbf{k}\sum_n \mathcal{G}^0_{\omega_n}(\mathbf{k})^2\tilde{\mathcal{G}}^0_{\omega_n}(\mathbf{k})^2 \\
&= -\frac{N(0)}{\beta_c}\sum_n\int_{-\infty}^\infty \mathrm{d}k\,\frac{1}{\left((\hbar\omega_n)^2+\varepsilon_{\mathbf{k}}^2\right)^2} \\
&= -\frac{N(0)}{\beta_c}\sum_n\frac{\pi}{2\,|\hbar\omega_n|} \\
&= -N(0)\left(\frac{1}{\pi k_{\mathrm{B}}T_{\mathrm{c}}}\right)^2\sum_{n=0}^\infty\frac{1}{(2n+1)^3} \\
&= -N(0)\left(\frac{1}{\pi k_{\mathrm{B}}T_{\mathrm{c}}}\right)^2\frac{7\zeta(3)}{8}.
\end{aligned}
\tag{2.76}
$$

Finally, putting all of this back together, rearranging terms, and taking the complex conjugate, the self-consistent equation (equation (2.62)) becomes

$$0 = N(0)\left(1 - \frac{T}{T_c}\right)\Delta(\mathbf{r}) - \frac{7\zeta(3)}{6}\frac{N(0)\epsilon_F^0}{\pi^2 k_B^2 T_c^2}\frac{1}{4m}\left[-i\hbar\nabla + \frac{2e\mathbf{A}(\mathbf{r})}{c}\right]^2\Delta(\mathbf{r})$$
$$- \frac{7\zeta(3)}{8\pi^2 k_B^2 T_c^2}N(0)\left|\Delta(\mathbf{r})\right|^2\Delta(\mathbf{r}). \tag{2.77}$$

This is very reminiscent of the first equation of GL theory and can in fact be identified with this equation. Identifying the parameters of the GL theory with these results in the relations

$$a(T) = -\frac{6}{7\zeta(3)}\frac{\pi^2(k_B T_c)^2}{\epsilon_F^0}\left(1 - \frac{T}{T_c}\right), \tag{2.78a}$$

$$b = \frac{6}{7\zeta(3)}\frac{\pi^2(k_B T_c)^2}{\epsilon_F^0 n}, \tag{2.78b}$$

$$\Psi = \left(\frac{7\zeta(3)n}{8\pi^2(k_B T_c)^2}\right)^{1/2}\Delta, \tag{2.78c}$$

$$m^* = 2m, \tag{2.78d}$$

$$e^* = 2e. \tag{2.78e}$$

With this identification we find that the effective mass and effective charge are double the electron mass and charge. This agrees well with the measured value for the flux quantum, φ_0. In order to make direct comparisons between BCS and GL theory predictions we will usually undo the scaling of Ψ so that the order parameter and the gap can be displayed on the same scale.

The BCS and GL results are compared in (figure 2.4). The agreement near T_c shows that the coefficients calculated allow for the connection of these theories in this limit, and a good agreement between the two theories is found in this region. However the agreement does not hold over the entire temperature range.

To complete the connection to the GL theory, we also need to find the equation of motion for the vector potential, $\mathbf{A}$. To find this, we want to use $\mathscr{G}$ to find the current. The current operator in the BCS theory is given by

$$\hat{\mathbf{j}}(\mathbf{r}) = \sum_\sigma -\frac{e}{2m}\left(\hat{\psi}_\sigma^\dagger(\mathbf{r})\left(-i\hbar\nabla + \frac{e\mathbf{A}(\mathbf{r})}{c}\right)\hat{\psi}_\sigma(\mathbf{r}) + \left[\left(-i\hbar\nabla + \frac{e\mathbf{A}(\mathbf{r})}{c}\right)\hat{\psi}_\sigma(\mathbf{r})\right]^\dagger\hat{\psi}_\sigma(\mathbf{r})\right)$$
$$= \sum_\sigma -\frac{e\hbar}{2mi}\left(\hat{\psi}_\sigma^\dagger(\mathbf{r})\nabla\hat{\psi}_\sigma(\mathbf{r}) - (\nabla\hat{\psi}_\sigma^\dagger(\mathbf{r}))\hat{\psi}_\sigma(\mathbf{r})\right) - \frac{e^2}{mc}\mathbf{A}(\mathbf{r})\hat{\psi}_\sigma^\dagger(\mathbf{r})\hat{\psi}_\sigma(\mathbf{r}). \tag{2.79}$$
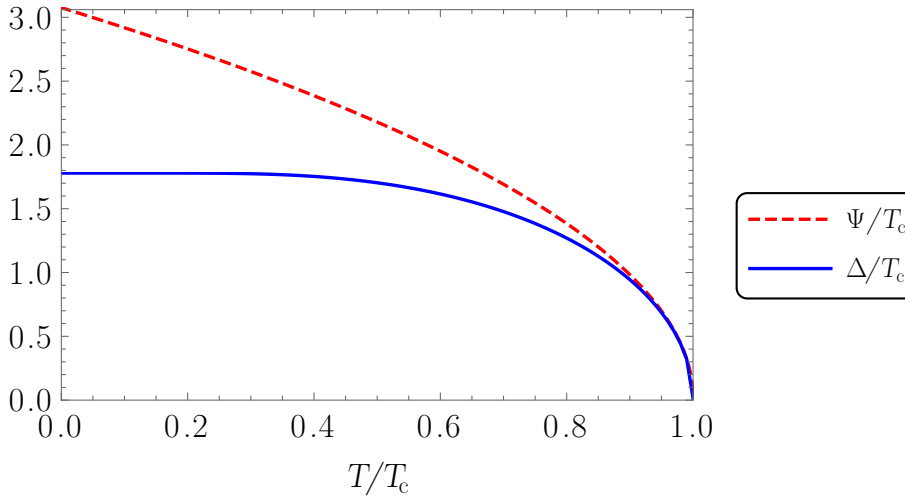
Figure 2.4: A comparison of the BCS gap to the GL order parameter as a function of T after scaling. It is clear that the GL result approximates the BCS result near the critical temperature T_c. The GL result fails to be a good approximation below about $0.9T_c$.

We can therefore relate the expectation value of the current operator to the Green function

$$\left\langle \hat{\mathbf{j}}(\mathbf{r},t) \right\rangle = -\frac{e\hbar}{m\mathrm{i}}\left(\nabla_{\mathbf{r}} - \nabla_{\mathbf{r}'}\right)\mathscr{G}(\mathbf{r}t^+,\mathbf{r}'t)|_{\mathbf{r}=\mathbf{r}'} - \frac{2e^2}{mc}\mathbf{A}(\mathbf{r})\mathscr{G}(\mathbf{r}t^+,\mathbf{r}t). \tag{2.80}$$

Using similar methods to the first GL equation calculation, and the expansion of the Green function (equation (2.61a)), this can be shown to reduce to the GL equation for the current (equation (2.6)). We omit this derivation since there are no free parameters in the GL equation for the current. The justification for this equation can however be found in [36, 140] and many other sources.

2.4 Summary

In this chapter we have given a brief overview of the main features of the two most successful theories of superconductivity – BCS theory and GL theory.

In GL theory we showed how the theory was created, first suggesting a complex order parameter, then using symmetry arguments to refine the form of the free energy. From this we found the GL equations. Looking at these in more detail we found two important length scales – ξ and λ. After scaling the equations to dimensionless quantities, we showed that the equations are only dependent on a single parameter, κ, the Ginzburg-Landau parameter. We then looked at two solutions of these equations, the interface solution and vortex states. The energy of both of these solutions changes sign at the critical value of $\kappa = 1/\sqrt{2}$, and this divides

superconductors into two classes with different magnetic properties. These are type I and type II superconductors.

Next we looked at BCS theory. We began with the BCS Hamiltonian with the contact approximation to the electron interaction. Taking a specific mean-field approximation, we eventually found the self-consistent BCS equations. These nonlinear integral equations must in general be solved numerically, however two important limits are found – the critical temperature and the gap at zero temperature.

The Gor'kov connection between the two theories allows for a comparison of the predictions from the two theories. This shows that the two theories are in agreement around the critical temperature, and the range where GL theory can be relied upon.

CHAPTER THREE

Multiband BCS Theory

Having examined the BCS case, we now generalise the theory to allow an arbitrary number of bands. This leads to separate superconducting band gaps, however the presence of interactions between these bands means that there is only a single critical temperature, as was shown by Suhl et al. in the two-band case [95].

In the two-band theory we calculate the critical temperature. We also simplify the equation for the gaps at zero temperature. However, unlike the one-band case, these cannot be solved in general. Numerical solutions across all temperatures are shown for a range of interband couplings. We also examine a perturbation in the interband coupling. This works well in the region between the critical temperatures of the uncoupled bands.

The three-band case is more interesting due to the presence of the TRSB state. In this section we derive the intriguing result that, in the TRSB state, the three-band self-consistent BCS equations reduce to uncoupled one-band BCS equations with a modified interaction strength. Additionally we derive a set of conditions using the one-band gap solutions such that the TRSB state exists if and only if these conditions are satisfied.

We finish the chapter by examining some thermodynamic observables. Plots of these observables as a function of temperature show additional features which are not present in one-band materials, and these can therefore be used as evidence of multiband effects in superconductors.

To simplify the notation, we will use an over arrow, $\vec{A}$, to indicate a band vector with components A_ν, and a check mark, $\check{A}$, to indicate a band matrix with components $A_{\nu,\nu'}$, where ν and ν' are band indices. This is distinguished from a vector in position or momentum space, which are set in bold face, $\mathbf{r}$.

3.1 The Multiband BCS Equations

To generalise the BCS theory to multiband superconductors, a band index ν is added to the electron operators and the bands are coupled by an interband Josephson coupling term. The Hamiltonian is written in momentum space as [95]

$$
\begin{aligned}
\hat{H} = &\sum_{\mathbf{k}\nu\sigma}(\epsilon_{\nu\sigma}(\mathbf{k}) - \mu)\hat{c}^\dagger_{\nu\sigma}(\mathbf{k})\hat{c}_{\nu\sigma}(\mathbf{k}) \\
&+ \frac{1}{2}\sum_{\mathbf{kk}'\nu\nu'\sigma\sigma'} V_{\nu\nu'}(\mathbf{k},\mathbf{k}')\hat{c}^\dagger_{\nu'\sigma}(\mathbf{k})\hat{c}^\dagger_{\nu'\sigma'}(\mathbf{k}')\hat{c}_{\nu\sigma'}(\mathbf{k}')\hat{c}_{\nu\sigma}(\mathbf{k}),
\end{aligned}
\tag{3.1}
$$

where $\epsilon_{\nu\sigma}(\mathbf{k})$ is the energy of the noninteracting state, $\sigma =\uparrow,\downarrow$ indicates the spin state, ν, ν' are band indices, $\hat{c}_{\nu\sigma}(\mathbf{k})$ $(\hat{c}^\dagger_{\nu\sigma}(\mathbf{k}))$ are the electron annihilation (creation) operators in momentum space, μ is the chemical potential, $V_{\nu\nu'}(\mathbf{k},\mathbf{k}')$ is the general momentum dependent intraband ($\nu = \nu'$) and interband ($\nu \neq \nu'$) coupling strengths. The Hamiltonian can also be written in real space, with the effective Hamiltonian given by

$$
\begin{aligned}
\hat{K}_{eff} = &\sum_\nu\sum_\sigma \int d\mathbf{r}\,\hat{\psi}^\dagger_{\nu\sigma}(\mathbf{r})\left\{\frac{1}{2m_\nu}\left[-i\hbar\nabla + \frac{e\mathbf{A}(\mathbf{r})}{c}\right]^2 - \mu\right\}\hat{\psi}_{\nu\sigma}(\mathbf{r}) \\
&- \frac{1}{2}\sum_{\nu\nu'}\sum_{\sigma\sigma'} g_{\nu\nu'}\int d\mathbf{r}\left[\left\langle\hat{\psi}^\dagger_{\nu\sigma}(\mathbf{r})\hat{\psi}^\dagger_{\nu\sigma'}(\mathbf{r})\right\rangle\hat{\psi}_{\nu'\sigma'}(\mathbf{r})\hat{\psi}_{\nu'\sigma}(\mathbf{r}) + h.c.\right],
\end{aligned}
\tag{3.2}
$$

where the usual cut off in momentum space is assumed.

From this we can find the equations of motion for the creation and annihilation operators in the imaginary time Heisenberg picture. These equations of motion couple the operators in the separate bands due to the Josephson coupling. The temperature Green function and anomalous Green function are defined as averages of the time ordered product of these operators

$$
\mathscr{G}_\nu(\mathbf{r}t,\mathbf{r}'t') = -\left\langle T_t\left[\hat{\psi}_{K\nu\uparrow}(\mathbf{r}t)\hat{\psi}^\dagger_{K\nu\uparrow}(\mathbf{r}'t')\right]\right\rangle,
\tag{3.3a}
$$
$$
\mathscr{F}_\nu(\mathbf{r}t,\mathbf{r}'t') = -\left\langle T_t\left[\hat{\psi}_{K\nu\uparrow}(\mathbf{r}t)\hat{\psi}_{K\nu\downarrow}(\mathbf{r}'t')\right]\right\rangle.
\tag{3.3b}
$$

The equation of motion for these Green functions shows that the definition for the superconducting gap should now be taken to be a sum over the anomalous amplitudes in the form

$$
\Delta^*_\nu(\mathbf{r}) = -\sum_{\nu'} g_{\nu\nu'}\left\langle\hat{\psi}^\dagger_{\nu'\downarrow}(\mathbf{r})\hat{\psi}^\dagger_{\nu'\uparrow}(\mathbf{r})\right\rangle
\tag{3.4a}
$$
$$
= \sum_{\nu'} g_{\nu\nu'}\mathscr{F}^\dagger_{\nu'}(\mathbf{r}t^+,\mathbf{r}t),
\tag{3.4b}
$$

where t^+ indicates that this time coordinate is evaluated in the limit that it goes to t from above, which is needed to fix the ordering of the operators in the time ordered product.

Following the methods of section 2.2.1, assuming a uniform solution, we find the multiband self-consistent equations for the superconducting gaps:

$$\Delta_\nu = \sum_{\nu'} g_{\nu\nu'} N_{\nu'}(0) \int_0^{\hbar\omega_D} d\varepsilon \, \frac{\Delta_{\nu'}}{\sqrt{\varepsilon^2 + |\Delta_{\nu'}|^2}} \tanh \left[\frac{\sqrt{\varepsilon^2 + |\Delta_{\nu'}|^2}}{2k_B T} \right]. \tag{3.5}$$

This form confirms that the quantity defined in equation (3.4) is the gap we are interested in as it is this quantity that appears as a gap in the excitation spectra in the energy integrals.

This equation can be written in a more compact form by defining $\check{N}(0)$ to be a diagonal matrix with elements $N_\nu(0)$, and $\check{I}(\vec{\Delta}, T)$ to be another diagonal matrix with elements

$$I_{\nu\nu}(\vec{\Delta}, T) = \int_0^{\hbar\omega_D} d\varepsilon \, \frac{1}{\sqrt{\varepsilon^2 + |\Delta_\nu|^2}} \tanh \left[\frac{\sqrt{\varepsilon^2 + |\Delta_\nu|^2}}{2k_B T} \right]. \tag{3.6}$$

We also define the effective coupling matrix, $\check{\Lambda} = \check{g}\check{N}(0)$. With these we may write the self-consistent equation in matrix form as

$$\vec{\Delta} = \check{\Lambda}\check{I}(\vec{\Delta}, T)\vec{\Delta}, \tag{3.7}$$

which may be solved for any temperature. However, assuming that $\check{\Lambda}$ is invertible, it is often simpler to work with the equation

$$0 = \left(\check{\Lambda}^{-1} - \check{I}(\vec{\Delta}, T) \right) \vec{\Delta}, \tag{3.8}$$

since in this form the integrals only appear on the diagonal.

The critical temperature may be calculated by finding the largest temperature T_c which solves the equation

$$\det \left(\check{\Lambda}^{-1} - \check{I}(\vec{0}, T_c) \right) = 0. \tag{3.9}$$

This is the largest temperature for which there is a nontrivial solution to the matrix equation. In this limit the integral is the same for all bands and is the same integral which appears in this limit in the one-band theory. The approximate solution, which we define to be $\mathcal{A}$, is

$$\mathcal{A} = I_{\nu\nu}(\vec{0}, T_c) = \int_0^{\hbar\omega_D} \frac{d\varepsilon}{\varepsilon} \tanh \left(\frac{\varepsilon}{2k_B T_c} \right)$$
$$= \ln \left(\frac{2\hbar\omega_D e^\Gamma}{\pi k_B T_c} \right). \tag{3.10}$$

Here $\Gamma \approx 0.577216$ is the Euler-Mascheroni constant and ω_{D} is the Debye frequency.

The equation at $T = 0$ can also be simplified. In this limit, the integrals can be performed exactly

$$I_{\nu\nu}(\vec{\Delta}_0, 0) = \ln \left(\frac{\hbar\omega_{\mathrm{D}} + \sqrt{\hbar\omega_{\mathrm{D}}^2 + |\Delta_{0\nu}|^2}}{|\Delta_{0\nu}|} \right). \tag{3.11}$$

However, while in the one-band case we can solve the resulting equation exactly, in the multiband case the resulting equations must be solved by numerical iteration or by some other numerical method.

3.2 Two-band BCS

To find explicit solutions, we first restrict ourselves to a two-band BCS system. For the two-band system, the BCS equations can be written explicitly as

$$\Lambda^{-1}{}_{11}\Delta_1 + \Lambda^{-1}{}_{12}\Delta_2 = \int_0^{\hbar\omega_{\mathrm{D}}} \mathrm{d}\varepsilon \, \frac{\Delta_1}{\sqrt{\varepsilon^2 + |\Delta_1|^2}} \tanh\left(\frac{\sqrt{\varepsilon^2 + |\Delta_1|^2}}{2k_{\mathrm{B}}T} \right), \tag{3.12a}$$

$$\Lambda^{-1}{}_{21}\Delta_1 + \Lambda^{-1}{}_{22}\Delta_2 = \int_0^{\hbar\omega_{\mathrm{D}}} \mathrm{d}\varepsilon \, \frac{\Delta_2}{\sqrt{\varepsilon^2 + |\Delta_2|^2}} \tanh\left(\frac{\sqrt{\varepsilon^2 + |\Delta_2|^2}}{2k_{\mathrm{B}}T} \right), \tag{3.12b}$$

where again $\Lambda_{ij} = g_{ij}N_j(0)$. From this, it is evident that in the presence of a nonzero interband coupling strength, if either Δ_1 or Δ_2 is nonzero, then both are nonzero. In this way, a band can be induced into a superconducting state above its (one band) critical temperature by the presence of a second superconducting band. Additionally, we shall see that the critical temperature of both bands is always increased above the one band values.

The equation for T_{c} (equation (3.9)) can be computed explicitly for a two-band superconductor. The equation can be simplified to the form

$$k_{\mathrm{B}}T_{\mathrm{c}} = \frac{2\mathrm{e}^\Gamma}{\pi} \hbar\omega_{\mathrm{D}} \exp\left[-\frac{\Lambda_{11} + \Lambda_{22} - \sqrt{(\Lambda_{11} - \Lambda_{22})^2 + 4\Lambda_{12}\Lambda_{21}}}{2(\Lambda_{11}\Lambda_{22} - \Lambda_{12}\Lambda_{21})} \right] \tag{3.13}$$

$$= \frac{2\mathrm{e}^\Gamma}{\pi} \hbar\omega_{\mathrm{D}} \exp\left[-\frac{2}{(\Lambda_{11} + \Lambda_{22}) + \sqrt{(\Lambda_{11} - \Lambda_{22})^2 + 4\Lambda_{12}\Lambda_{21}}} \right] \tag{3.14}$$

$$\approx T_{1\mathrm{c}} \left(1 + \frac{\Lambda_{12}\Lambda_{21}}{\Lambda_{11}^2(\Lambda_{11} - \Lambda_{22})} + \mathcal{O}\left(\Lambda_{12}^2\Lambda_{21}^2 \right) \right), \tag{3.15}$$

when $\Lambda_{11} > \Lambda_{22}$, where $T_{1\mathrm{c}}$ is the critical temperature of the uncoupled first band, which is assumed to be the dominant band.

In the limit $T \to 0$ the integral is again simplified since $\tanh\left(\frac{\sqrt{\xi^2+\Delta^2}}{2k_{\mathrm{B}}T}\right) \to 1$. The equations then become

$$\Lambda^{-1}{}_{11}\Delta_{10} + \Lambda^{-1}{}_{12}\Delta_{20} = \int_0^{\hbar\omega_{\mathrm{D}}} \mathrm{d}\varepsilon \, \frac{\Delta_{10}}{\sqrt{\varepsilon^2 + |\Delta_{10}|^2}}, \tag{3.16a}$$

$$\Lambda^{-1}{}_{21}\Delta_{10} + \Lambda^{-1}{}_{22}\Delta_{20} = \int_0^{\hbar\omega_{\mathrm{D}}} \mathrm{d}\varepsilon \, \frac{\Delta_{20}}{\sqrt{\varepsilon^2 + |\Delta_{20}|^2}}. \tag{3.16b}$$

These cannot be solved exactly. However, writing the ratio of the gaps as χ, and making the weak coupling approximation $\Delta_{10}, \Delta_{20} \ll \hbar\omega_{\mathrm{D}}$, this can be simplified to the equations

$$\Lambda^{-1}{}_{11} + \Lambda^{-1}{}_{12}\chi = \ln\left(\frac{2\omega_{\mathrm{D}}}{|\Delta_{20}|}\right) + \ln(\chi), \tag{3.17a}$$

$$\Lambda^{-1}{}_{21}\frac{1}{\chi} + \Lambda^{-1}{}_{22} = \ln\left(\frac{2\omega_{\mathrm{D}}}{|\Delta_{20}|}\right). \tag{3.17b}$$

If the gaps are nearly equal, then the $\ln(\chi)$ term can be expanded around $\chi = 1$ to then obtain the required accuracy. At the lowest order, $\chi = 1$ and

$$\Delta_{10} = \Delta_{20} = 2\hbar\omega_{\mathrm{D}} \exp\left[-\frac{2}{(\Lambda_{11} + \Lambda_{22}) + \sqrt{(\Lambda_{11} - \Lambda_{22})^2 + 4\Lambda_{12}\Lambda_{21}}}\right]. \tag{3.18}$$

Comparing this to the equation for T_{c} (equation (3.14)) shows that the universal BCS relation between Δ_0 and T_{c} is recovered in this limit. However, as χ moves away from 1, this no longer holds. Corrections for the gap at $T = 0$ can be found by keeping more terms in the expansion of the $\ln$ term, or by solving the equations numerically.

We also note that there is a symmetry in the full two-band BCS equations. Performing the following transformation on the self-consistent equations has the same solutions

$$\Delta_2 \to -\Delta_2, \quad g_{12} \to -g_{12}. \tag{3.19}$$

Therefore changing the sign of the interband coupling does not change the magnitude of either of the gaps, but changes whether the gaps are in phase or out of phase with each other. We can therefore consider g_{12} to be positive without loss of generality.

In figure 3.1 a numerical two-band solution is plotted for a typical set of parameters and varying interband coupling g_{12}. At low interband coupling the first band is effectively unperturbed. However the second band is perturbed significantly near the uncoupled critical temperature. The smaller band also has its critical temperature
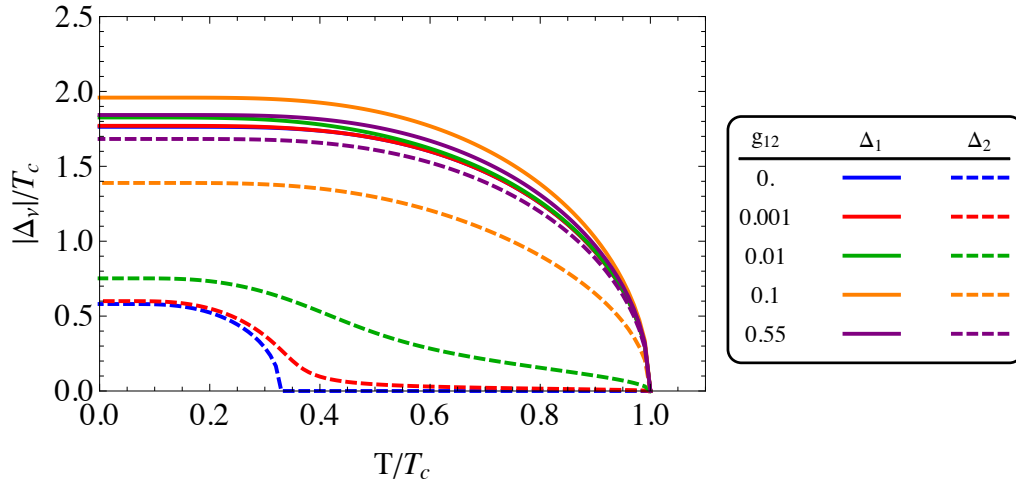
Figure 3.1: Numerical solutions to the two-band BCS equations with varying interband coupling constants g_{12}. We have used the parameters $N_1(0) = N_2(0) = 0.3$, $g_{11} = 0.6$, $g_{22} = 0.5$. In the limit of small coupling, the second band is very small above its uncoupled T_c, while at large interband coupling, both bands begin to look similar to a one-band BCS curve.

increased to that of the dominant one. The second band is said to be induced in the region above its uncoupled critical temperature and below the critical temperature of the combined system.

3.2.1 Perturbation Expansion

If the interband coupling is small enough, we can perform a perturbation expansion in g_{12} which performs well for some temperatures. This provides an insight into the leading behaviour of the interband coupling.

Let us assume that band one is the dominant band. Then the region where this perturbation expansion is possible is in the region between T_{2c}, the critical temperature of the uncoupled second band, and T_c, the critical temperature of the combined system. In the uncoupled limit, the T_c of the combined system is just the critical temperature of the first band, T_{1c}.

We expand the gaps as

$$\Delta_\nu = \Delta_\nu^{(0)} + g_{12}\Delta_\nu^{(1)} + \mathcal{O}\left(g_{12}^2\right). \tag{3.20}$$

Then we know that in this region $\Delta_2^{(0)} = 0$. So that we can solve the system all the way to T_c, we scale the temperature by the full critical temperature as $t = T/T_c$, where we are interested in the region $T_{2c}/T_c < t < 1$. We then expand the critical

temperature in the same way as the gaps.

$$T_c = T_c^{(0)} + g_{12}T_c^{(1)} + \mathcal{O}\left(g_{12}{}^2\right). \tag{3.21}$$

However, we have already computed this expansion (equation (3.15)). We therefore know that $T_c^{(0)} = T_{1c}$ and $T_c^{(1)} = 0$. Putting these into the self-consistent BCS equations and keeping terms of order 1 results in the one-band equation for the first band, for which we know how to compute the solution. In the region we are interested in, the second equation only has the trivial solution, so $\Delta_2^{(0)} = 0$ in this region.

Keeping the terms linear in g_{12} we find two equations

$$\frac{\Delta_1^{(1)}}{g_{11}N_1(0)} = \Delta_1^{(1)} \int_0^{\hbar\omega_D} d\varepsilon \, \frac{1}{2tT_c^{(0)}(\Delta_1^{(0)2} + \varepsilon^2)^{3/2}} \text{sech}\left(\frac{\sqrt{\Delta_1^{(0)2} + \varepsilon^2}}{2tT_c^{(0)}}\right)$$
$$\times \left[\Delta_1^{(0)2}\sqrt{\Delta_1^{(0)2} + \varepsilon^2} + tT_c^{(0)}\varepsilon^2 \sinh\left(\frac{\sqrt{\Delta_1^{(0)2} + \varepsilon^2}}{2tT_c^{(0)}}\right)\right], \tag{3.22a}$$

$$\frac{\Delta_2^{(1)}}{g_{22}N_2(0)} - \frac{\Delta_1^{(0)}}{g_{11}g_{22}N_2(0)} = \Delta_2^{(1)} \int_0^{\hbar\omega_D} d\varepsilon \, \frac{1}{\varepsilon} \tanh\left(\frac{\varepsilon}{2tT_c^{(0)}}\right), \tag{3.22b}$$

which need to hold for all temperatures. The first of these has $\Delta_1^{(1)}$ appear only as a multiplicative factor on both sides. So either the equality holds for all temperatures and $\Delta_1^{(1)}$ is not restricted, or the equality does not hold and $\Delta_1^{(1)} = 0$. Looking more closely we find that this equation is distinct from the equation solved by $\Delta_1^{(0)}$, so that we have $\Delta_1^{(1)} = 0$.

For the second equation, we see that we know how to compute the integral. We can therefore immediately solve the equation to find

$$\Delta_2^{(1)} = \frac{\Delta_1^{(0)}}{g_{11}\left(1 - N_2(0)g_{22}\left[\ln\left(\frac{2\hbar\omega_D}{\pi tT_c^{(0)}}\right) + \Gamma\right]\right)} \tag{3.23}$$

$$= \frac{\Delta_1^{(0)}}{g_{11}\left(1 - N_2(0)g_{22}\left[\frac{1}{g_{11}N_1(0)} - \ln(t)\right]\right)}. \tag{3.24}$$

We can immediately see that this approximation fails at $t = T_{2c}/T_c^{(0)}$ since the denominator goes to zero at this point.

Within the context of GL, Komendová et al. [119] showed that at the point T_{2c} the second gap is of order $g_{12}{}^{1/3}$, so it is unsurprising that this method fails, since this method assumes that the leading correction is of order g_{12}.
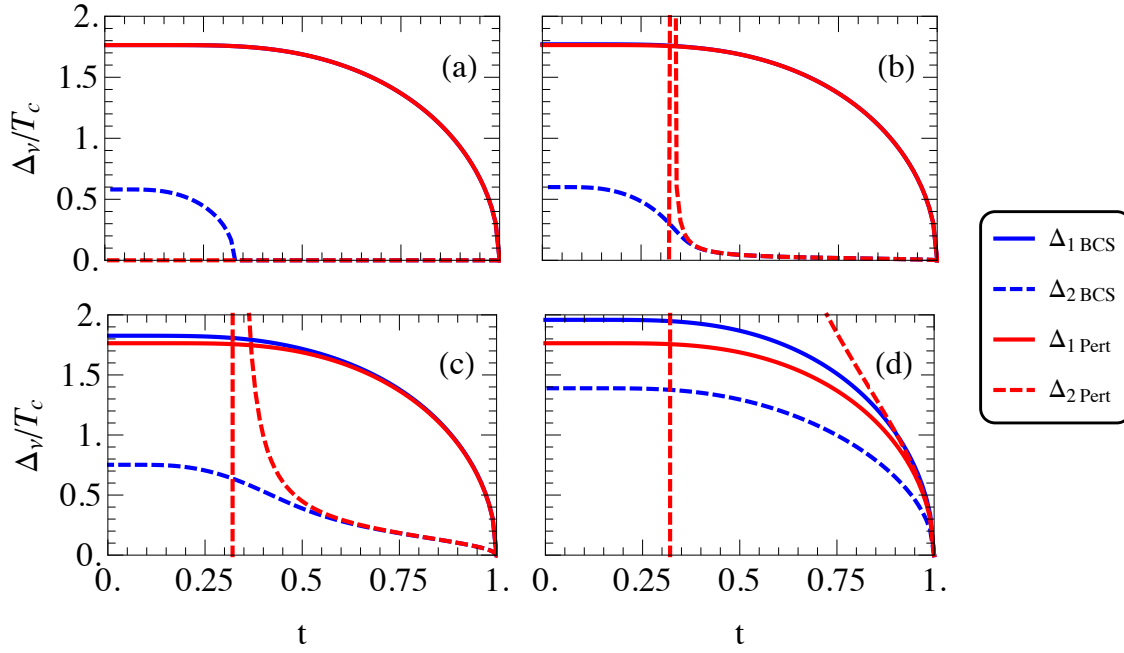
Figure 3.2: A comparison of the perturbation approximation to numerical solutions to the two-band BCS equations. In all plots we use $N_1(0) = N_2(0) = 0.3$, $g_{11} = 0.6$, $g_{22} = 0.5$. The interband coupling varies in the plots with a) $g_{12} = 0.$, b) $g_{12} = 0.001$, c) $g_{12} = 0.01$, and d) $g_{12} = 0.1$.

With this expansion, we can calculate the one-band solution once, and then use this to find the first order correction for the second band for many different parameter sets.

At the next order, we find that $\Delta_2^{(2)} = 0$. To solve the equation for $\Delta_1^{(2)}$ we would need to be able to perform the integral

$$\int_a^\infty \mathrm{d}x \frac{x\mathrm{sech}^2(x) - \tanh(x)}{x^3},$$

where the lower limit on the integral, a, depends on the value of $\Delta_1^{(0)}$. While this integral can be performed numerically, this would need to be performed for each temperature since the integral depends on the temperature through the lower bound. While this is an added cost that makes this method less applicable, the method would still be faster than a solution of the full equations, or could be used as a first approximation for a numerical method.

An example application of this is shown in figure 3.2. The perturbation approximation is compared to numerical solutions of the multiband BCS equations. In the absence of interband coupling the perturbation simply returns the one-band solution for the dominant band with no contribution from the second band. At low
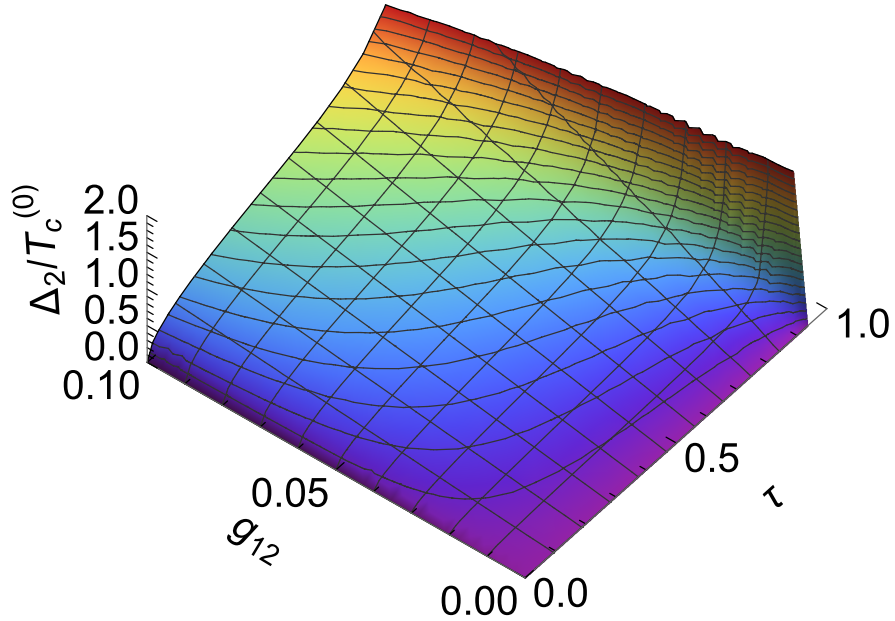
Figure 3.3: A plot showing the perturbation expansion solution for the second band as a function of the interband coupling. The parameters used here are $N_1(0) = N_2(0) = 0.3$, $g_{11} = 0.6$, $g_{22} = 0.4$. This exploration of parameter space is much faster with the perturbation expansion than working directly with the full multiband equations.

interband coupling, the approximation works very well until near T_{2c}, where the approximation diverges. At larger interband coupling the approximation no longer provides a good approximation to the full solution. This is expected since higher terms in the perturbation expansion become important at higher interband coupling.

We also note that the perturbation converges to the true solution in the limit that the interband coupling goes to zero, but it does not converge uniformly.

In figure 3.3 the magnitude of the second gap in the perturbation expansion is shown as a function of the interband coupling. This shows how the second band is induced above the one-band critical temperature by the coupling to the first band. For any nonzero coupling, the critical temperature immediately increases.

3.3 Three-band BCS and the TRSB State

We now look at a three-band BCS system. With three bands there is the possibility of additional physics. The critical temperature is found in the same way as the

two-band case. The simplest form for the T_c equation is

$$0 = \begin{vmatrix} \Lambda^{-1}{}_{11} - \mathcal{A} & \Lambda^{-1}{}_{12} & \Lambda^{-1}{}_{13} \\ \Lambda^{-1}{}_{21} & \Lambda^{-1}{}_{22} - \mathcal{A} & \Lambda^{-1}{}_{23} \\ \Lambda^{-1}{}_{31} & \Lambda^{-1}{}_{32} & \Lambda^{-1}{}_{33} - \mathcal{A} \end{vmatrix}, \tag{3.25}$$

where again $\mathcal{A} = \ln\left(\frac{2\hbar\omega_D e^\Gamma}{\pi k_B T_c}\right)$ is the result of the integral at zero temperature. This is a cubic in $\mathcal{A}$ which can be solved exactly, but the resulting expression is rather complicated. We can also calculate Δ_0, the gap at zero temperature. In this limit, the integral can be performed exactly with the result

$$\int_0^{\hbar\omega_D} \frac{d\varepsilon}{\sqrt{\varepsilon^2 + \Delta_0^2}} = \ln\left(\frac{\hbar\omega_D + \sqrt{\hbar\omega_D^2 + |\Delta_0|^2}}{|\Delta_0|}\right) \tag{3.26}$$

$$\approx \ln\left(\frac{2\hbar\omega_D}{|\Delta_0|}\right). \tag{3.27}$$

Then the gap at $T = 0$ is found by solving the set of equations

$$\sum_\nu \Lambda^{-1}{}_{\nu\nu'}\Delta_{0\nu} = \Delta_{0\nu'} \ln\left(\frac{\hbar\omega_D + \sqrt{\hbar\omega_D^2 + |\Delta_{0\nu'}|^2}}{|\Delta_{0\nu'}|}\right). \tag{3.28}$$

This is most easily done using an iterative method.

For the three-band system, the BCS equations are invariant under the transformation

$$\Delta_i \to -\Delta_i, \quad \Lambda_{ij} \to -\Lambda_{ij}, \quad \Lambda_{ik} \to -\Lambda_{ik}, \tag{3.29}$$

with $i \neq j \neq k$. There are therefore two independent cases to consider – one with all $\Lambda_{\nu\nu'}$ positive and one with all $\Lambda_{\nu\nu'}$ negative, as we can perform this transformation to find the solution to the other cases. The case where all interactions are repulsive is very interesting as this can lead to frustration between the three gaps.

Numerical solutions for a three-band case over all T are shown in figure 3.4. For this plot we use the parameters: $\hbar\omega_D = 0.9$, $g_{11} = 0.7$, $g_{22} = 0.75$, $g_{33} = 0.6$, $g_{12} = g_{13} = g_{23} = -0.1$, $N_1(0) = 0.4$, $N_2(0) = 0.5$, $N_3(0) = 0.6$. With these parameters, a kink appears in the gap at about $T/T_c = 0.45$. This kink is more pronounced in the smallest gap, but is present in all three bands. Above this temperature, the phase difference between the gaps must either be 0 or π. In this region the superconductor is in a conventional BCS state. Below this point $(T/T_c < 0.45)$ the phase difference will be between 0 and π, and the superconductor is in the TRSB state (also see [108, 109]).
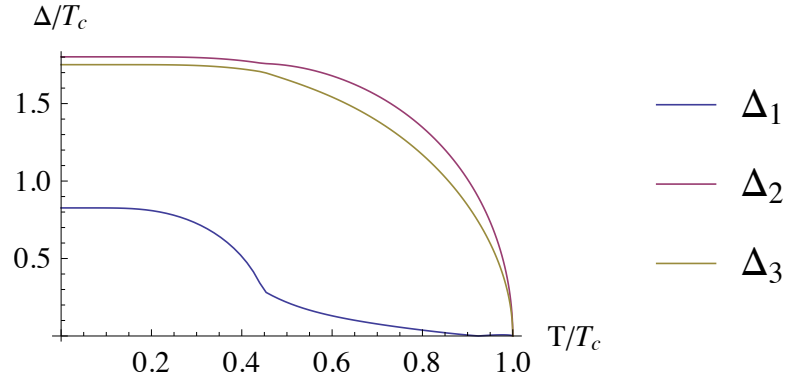
Figure 3.4: A numerical solution to the three-band BCS equations. Notice the kink at $T/T_c \approx 0.45$. Below this point the superconductor is in the TRSB state.

In addition to this kink, the gap in band one also vanishes at a single point at about $T/T_c \approx 0.9$. We denote this temperature T^0 and will later show that this corresponds to a change of phase, where the gaps change from being in phase with each other to having one out of phase. The conditions required for the existence of this point are related to the conditions for the TRSB state, and the two are often (although not always) found on the same plot as a function of temperature.

3.3.1 Calculation of the TRSB State

For a three-band superconductor, most solutions of the self-consistent multiband BCS equations have the three gaps either in phase or out of phase with each other. However, for some input parameters and below a critical temperature T^*, there exists a solution to the BCS self-consistent equations (equation (3.8)) where the three bands have relative phases other than 0 or π due to frustration of the interaction between the three gap functions. These gap functions are therefore described by a complex amplitude even in the uniform case. When this happens the ground state is doubly degenerate because the complex conjugate of the gap functions is also a solution to equation (3.8). The gap functions are therefore in a chiral ground state, and the time-reversal symmetry is spontaneously broken.

Considering the gap functions as vectors in the complex plane (figure 3.5), we see that the two possible ground states have different chirality. This induces a breaking of the mirror symmetry in the phase plane, which also induces the breaking of the time-reversal-symmetry.

Here we show how to calculate the magnitude of the gap in the TRSB state in terms of a set of one-band BCS gap equations, and find the condition for the
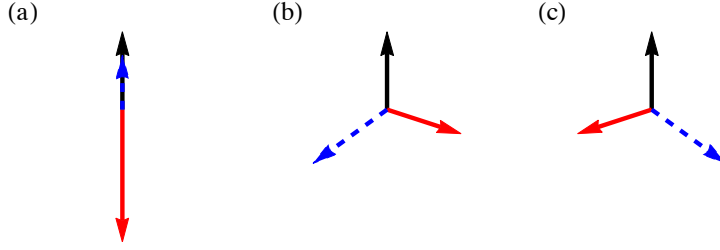
Figure 3.5: (a) For most ground state solutions, all band gaps are in phase or out of phase with each other. After removing an arbitrary phase, the gap at a point can be described by a real number. (b)-(c) In the TRSB state, the gaps can have any phase between them. In this case, after removal of the an arbitrary phase, the gaps are still described by a complex number. The ground state is thus doubly degenerate, with the ground states being complex conjugates of each other.

appearance of the TRSB state.

For the three-band case, the self-consistent BCS equations (equation (3.8)) can be written in matrix form as

$$
\begin{bmatrix}
I(\Delta_1, T) - \Lambda^{-1}{}_{11} & -\Lambda^{-1}{}_{21} & -\Lambda^{-1}{}_{31} \\
-\Lambda^{-1}{}_{12} & I(\Delta_2, T) - \Lambda^{-1}{}_{22} & -\Lambda^{-1}{}_{32} \\
-\Lambda^{-1}{}_{13} & -\Lambda^{-1}{}_{23} & I(\Delta_3, T) - \Lambda^{-1}{}_{33}
\end{bmatrix}
\begin{bmatrix}
\Delta_1 \\
\Delta_2 \\
\Delta_3
\end{bmatrix} = \vec{0}, \quad (3.30)
$$

where there is an arbitrary global phase. We can choose the global phase such that $\Delta_1 = |\Delta_1|$. Then, taking the imaginary part, we find

$$
\begin{bmatrix}
I(\Delta_2, T) - \Lambda^{-1}{}_{22} & -\Lambda^{-1}{}_{32} \\
-\Lambda^{-1}{}_{23} & I(\Delta_3, T) - \Lambda^{-1}{}_{33}
\end{bmatrix}
\begin{bmatrix}
\mathrm{Im}(\Delta_2) \\
\mathrm{Im}(\Delta_3)
\end{bmatrix} = \vec{0}. \quad (3.31)
$$

If we are interested in the TRSB states, then the imaginary components of these gaps must be nonzero. Hence the determinant of the matrix must equal zero. We will denote a magnitude of the gap that satisfies this requirement $\overline{\Delta_i}$. This leads to the constraint equation

$$
(I(\overline{\Delta_2}, T) - \Lambda^{-1}{}_{22})(I(\overline{\Delta_3}, T) - \Lambda^{-1}{}_{33}) - \Lambda^{-1}{}_{23}\Lambda^{-1}{}_{32} = 0. \quad (3.32)
$$

We can make similar demands for the other gaps, resulting in two other similar conditions. These have the solution

$$
I(\overline{\Delta_j}, T) = \Lambda^{-1}{}_{jj} \pm \sqrt{\frac{\Lambda^{-1}{}_{jk}\Lambda^{-1}{}_{lj}}{\Lambda^{-1}{}_{lk}}} \sqrt{\frac{\Lambda^{-1}{}_{jl}\Lambda^{-1}{}_{kj}}{\Lambda^{-1}{}_{kl}}} \quad (3.33)
$$

$$
= \Lambda^{-1}{}_{jj} \pm \frac{\Lambda^{-1}{}_{jk}\Lambda^{-1}{}_{lj}}{\Lambda^{-1}{}_{lk}}, \quad (3.34)
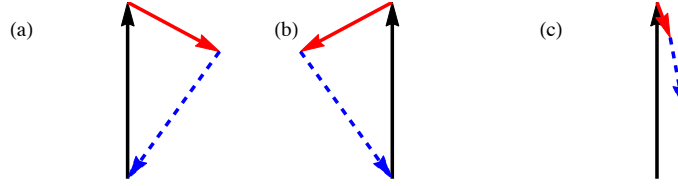$$

Figure 3.6: The triangle inequality can be viewed as a restriction on the ability to form a triangle with three vectors of a given length. (a) &(b). If the triangle inequality is satisfied, then two triangles can be formed which are mirror images of each other. (c) If the triangle inequality is not satisfied, then it is not possible to form a triangle with the vectors of that length because one of the vectors is too long.

for all permutations $j, k, l = 1, 2, 3$ where we have used the definition of Λ and the fact that $g_{ij} = g_{ji}$. These equations are now decoupled one-band BCS self-consistent equations for the superconducting gaps with modified interaction strengths.

We only need to keep the negative solution because the TRSB state is only stable when one or all three coupling parameters are negative, $\Lambda_{12}\Lambda_{13}\Lambda_{23} < 0$, so that the interactions between the bands are frustrated. We can now substitute equation (3.33) into equation (3.30) to find

$$
\begin{bmatrix}
-\frac{\Lambda^{-1}{}_{12}\Lambda^{-1}{}_{31}}{\Lambda^{-1}{}_{32}} & -\Lambda^{-1}{}_{21} & -\Lambda^{-1}{}_{31} \\
-\Lambda^{-1}{}_{12} & -\frac{\Lambda^{-1}{}_{21}\Lambda^{-1}{}_{32}}{\Lambda^{-1}{}_{31}} & -\Lambda^{-1}{}_{32} \\
-\Lambda^{-1}{}_{13} & -\Lambda^{-1}{}_{23} & -\frac{\Lambda^{-1}{}_{31}\Lambda^{-1}{}_{23}}{\Lambda^{-1}{}_{21}}
\end{bmatrix}
\begin{bmatrix}
\overline{\Delta_1} \\
\overline{\Delta_2} \\
\overline{\Delta_3}
\end{bmatrix} = 0,
\tag{3.35}
$$

which results in a single condition which must be met for a stable solution. This can be rewritten in the form

$$
\frac{\overline{\Delta_1}}{g^{-1}{}_{23}} + \frac{\overline{\Delta_2}}{g^{-1}{}_{13}} + \frac{\overline{\Delta_3}}{g^{-1}{}_{12}} = 0,
\tag{3.36}
$$

where the $\overline{\Delta_\nu}$ are complex with unknown phase differences. The existence of a solution to this constraint equation is only possible if the triangle inequality

$$
\left| \frac{\overline{\Delta_j}}{g^{-1}{}_{kl}} \right| \leq \left| \frac{\overline{\Delta_k}}{g^{-1}{}_{lj}} \right| + \left| \frac{\overline{\Delta_l}}{g^{-1}{}_{jk}} \right|,
\tag{3.37}
$$

holds for all permutations of $\{j, k, l\}$ (figure 3.6). In this way we can find the existence and position of the time-reversal-symmetry breaking by finding the solution to equation (3.33), then finding the regions over which equation (3.37) holds.

To the best of our knowledge we were the first to derive this reduction of the multiband BCS equations to a set of one-band BCS equations, along with the condition for when this is the stable solution [1]. We note that a similar condition has been derived for a TRSB superconductor in multiband GL by Hu and Wang [141], and later for a multiband BCS superconductor by Takahashi et al. [142].
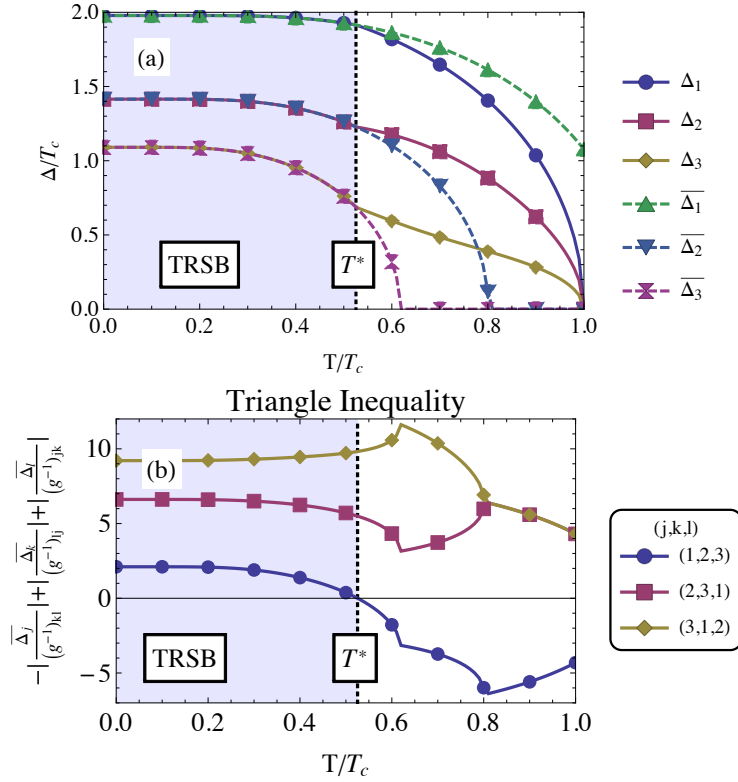
Figure 3.7: a) A direct solution to the three-band BCS equations (solid lines), as well as solutions to the one-band reduced equations for the TRSB state (dashed lines). In the TRSB state the multiband solution agrees with a reduced one-band solution, and the solutions diverge at T^*. b) The triangle inequality for the scaled reduced one-band gaps is plotted as a function of temperature. The point where the triangle equality fails is the same location as where the one-band solution departs from the multiband solution in the previous plot, T^*.

In figure 3.7 we perform this procedure explicitly with the parameters $\hbar\omega_{\mathrm{D}} = 0.09$, $g_{11} = g_{22} = g_{33} = 0.7$, $g_{12} = g_{13} = g_{23} = -0.1$, $N_1(0) = 0.35$, $N_2(0) = 0.32$, $N_3(0) = 0.3$. This set of parameters are arbitrary, yet reasonable for a three-band case. Similar results are found with other parameters. Figure (a) shows a direct multiband solution to the BCS equations, Δ, plotted with the one-band reduced BCS solutions, $\overline{\Delta}$. In figure (b) the triangle inequality for the three permutations are plotted as a function of temperature. These plots show that in the region where the inequalities hold, the multiband solution is precisely the solution $\overline{\Delta}$. At the point where the inequality is no longer satisfied there is a kink in the multiband solution as it ceases to be in the TRSB state. The point where the equality holds is the critical transition point T^*, and is the point that separates the TRSB state from the conventional BCS state.

At the point T^*, the full multiband solution separates from the reduced one-band
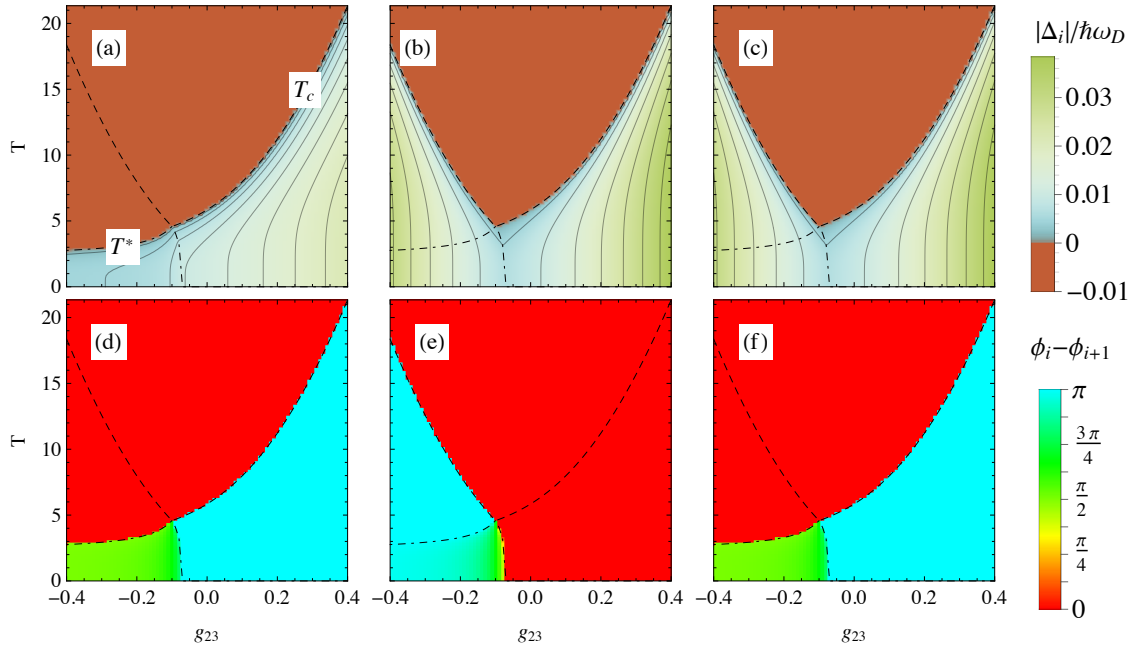
Figure 3.8: Phase diagram with equal bands. $\hbar\omega_{\mathrm{D}} = 0.09$, $N_i(0) = 0.2$, $g_{\nu\nu} = 0.8$, $g_{12} = g_{13} = -0.1$. (a)-(c) The gaps in bands 1-3, $|\Delta_\nu|$, respectively. (d)-(f) The phase difference between the gaps. (d) $\phi_1 - \phi_2$. (e) $\phi_2 - \phi_3$. (f) $\phi_3 - \phi_1$.

solution with a discontinuity in the derivative of the gaps. This discontinuity would lead to a jump in the heat capacity of the superconductor and other experimentally measurable quantities.

Looking at the TRSB triangle inequality (equation (3.37)), we see that there can be points above T^* where the permutation below zero changes sign, and another permutation drops below zero. At the point where they cross, the triangle inequality holds as an equality for the two permutations, and therefore the solution is again the reduced one-band BCS solution. As one of the one-band solutions is zero at this point, this allows the phase of this gap to change relative to the other two. We denote this point T^0, and note that this point can be seen most readily as a phase discontinuity.

3.3.2 Results

With the choice of a base set of parameters, we can vary a single parameter and observe the effect on the magnitude and relative phase of the gaps, as well as on the critical temperature T_{c}, the presence of the TRSB state, and the existence of a T^0 point.

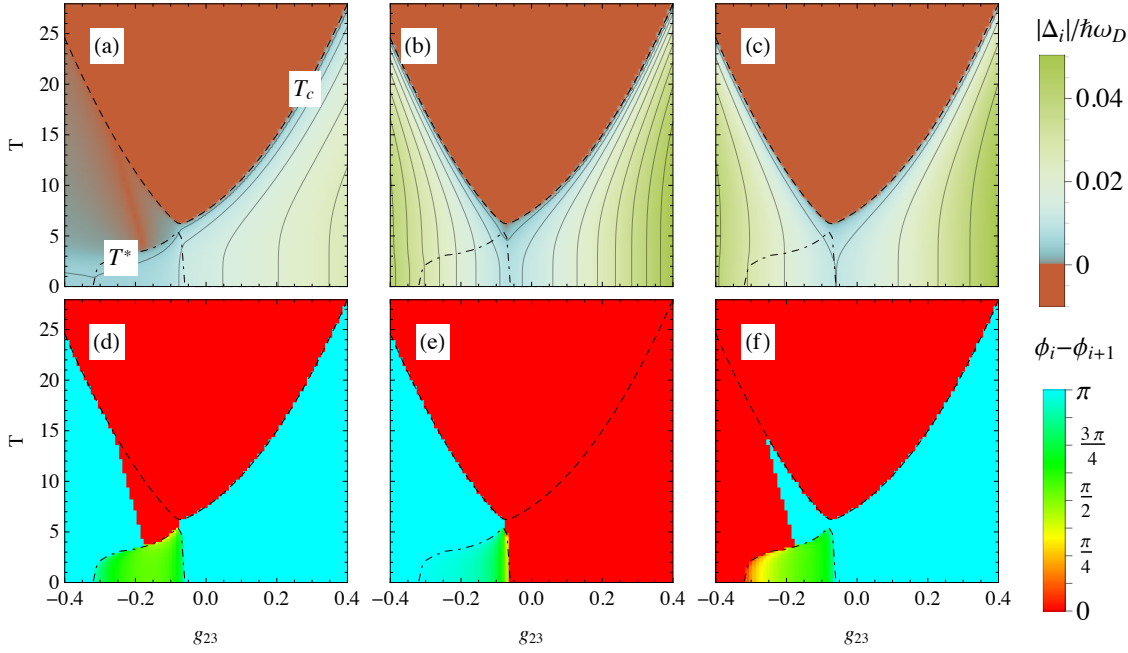We first choose the case where the parameters of all the bands are equal other

Figure 3.9: Phase diagram with nearly equal bands showing two phase discontinuities. $\hbar\omega_D = 0.09$, $N_1(0) = 0.2$, $N_2(0) = 0.21$, $N_3(0) = 0.22$, $g_{\nu\nu} = 0.8$, $g_{12} = -0.11$, $g_{13} = -0.1$. (a)-(c) The gaps in bands 1-3, $|\Delta_\nu|$, respectively. (d)-(f) The phase difference between the gaps. (d) $\phi_1 - \phi_2$. (e) $\phi_2 - \phi_3$. (f) $\phi_3 - \phi_1$.

than the parameter g_{23} (figure 3.8). We choose the parameters $\hbar\omega_D = 0.09$, $g_{11} = g_{22} = g_{33} = 0.8$, $g_{12} = g_{13} = -0.1$, $N_1(0) = N_2(0) = N_3(0) = 0.2$. In this case the parameter space divides into four regimes: at the top is the normal state, on the right is the simple three-band superconductivity, bottom left is the TRSB state, and at the top left the first band is identically zero, so that two-band superconductivity remains here. These four regions are separated by the phase transition lines T_c and T^*, which touch at the point $g_{23} = g_{12} = g_{13}$, which coincides with a minimum in T_c.

Due to bands 2 and 3 being identical, we see that the TRSB state continues to exist to $g_{23} = -\infty$, since any nonzero value for $|\Delta_1|$ will satisfy the triangle inequality. Moreover, when $|\Delta_1| = 0$ the triangle inequality is still satisfied as an equality, and thus the condition for T^0 is satisfied in the entire region above T^* left of the point $T^* = T_c$. Therefore the gap in the first band $|\Delta_1|$ equals zero in this region, and the phase difference for bands 2 and 3 is flipped to account for the repulsive interaction between these bands.

Next we look at the case where the parameters in all three bands are nearly equal (figure 3.9). Here we set $\hbar\omega_D = 0.09$, $g_{11} = g_{22} = g_{33} = 0.8$, $g_{12} = -0.11$, $g_{13} = -0.1$, $N_1(0) = 0.2$, $N_2(0) = 0.21$, $N_3(0) = 0.22$. With these parameters the two-band

superconductivity regime disappears, the TRSB regime is confined to a finite region, and a gap opens between the T^* line and the T_c line.

The two-band superconductivity regime disappears due to the finite difference between the bands Δ_2 and Δ_3. Therefore, as the temperature is increased, the $\overline{\Delta_1}$ term eventually becomes too small to satisfy the triangle inequality, and is therefore no longer forced to zero for the majority of this region. However, it remains heavily suppressed.

The finite region containing the TRSB state is also a consequence of the finite difference between the bands Δ_2 and Δ_3. As the coupling g_{23} is moved to $-\infty$, it enhances $\overline{\Delta_2}$ and $\overline{\Delta_3}$ equally, and hence the difference between them, while $\overline{\Delta_1}$ approaches a constant. Therefore, at some critical value of g_{23}, the magnitude of $\overline{\Delta_1}$ is too small to satisfy the triangle inequality, even at $T = 0$, and so the TRSB state disappears.

The gap opens between the T^* line and the T_c line because for these two points to touch there must be a location where all the terms in the triangle inequality are identical for all temperatures such that the TRSB state can extend all the way to T_c. However, the T_c and T^* lines are connected by two T^0 lines, one where $\Delta_1 = 0$, and one where $\Delta_2 = 0$. These lines are most easily seen in the phase plots as a sudden jump from a phase difference of 0 to π or vice versa, but the line for Δ_1 is also visible in the magnitude plot. We also note that the TRSB state is mainly found near the minimum in T_c.

Finally we look for a set of parameters that results in only a single T^0 line. We find that the parameters $\hbar\omega_D = 0.09$, $g_{11} = g_{22} = g_{33} = 0.7$, $g_{12} = -0.11$, $g_{13} = -0.1$, $N_1(0) = 0.3$, $N_2(0) = 0.21$, $N_3(0) = 0.22$ create this behaviour (figure 3.10). The T^0 line is again most easily seen in the phase plots, which show that in this case it is Δ_3 which goes to zero in this case.

The first gap is again suppressed in the upper left region, as was the case in the previous examples. The TRSB state again appears only near the minimum in T_c.

3.4 Thermodynamic Critical Field and Other Thermodynamic Observables

In this section we perform calculations of the thermodynamic critical field, as well as the entropy and the heat capacity, for a range of multiband BCS parameters. The form of the equations for the thermodynamic observables are derived from the
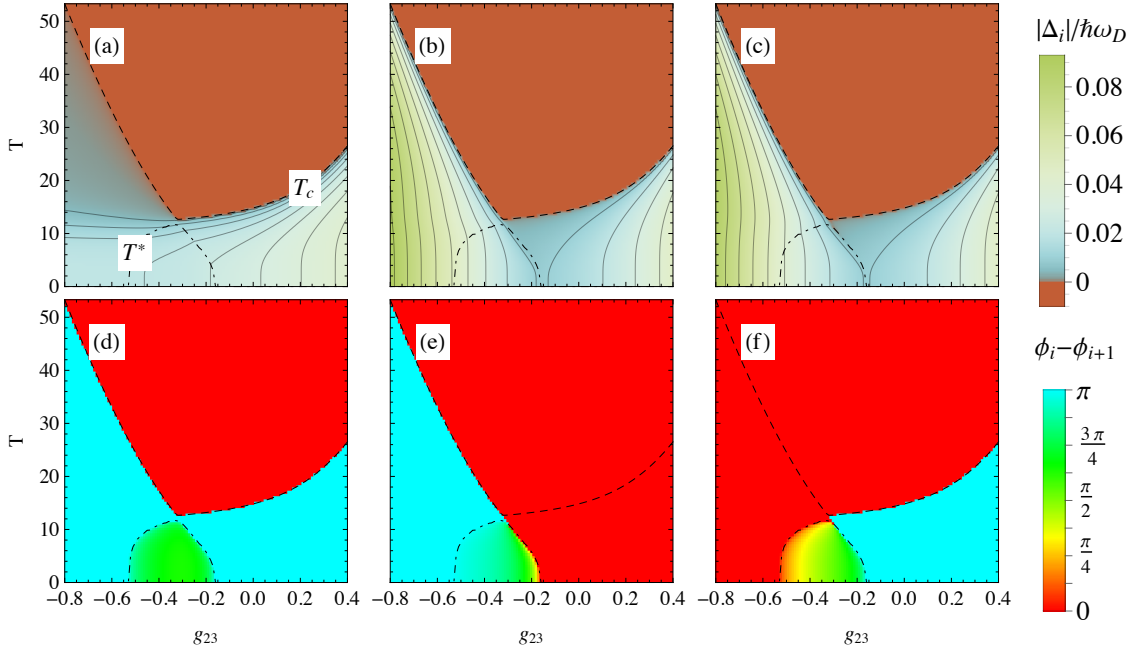
Figure 3.10: Phase diagram with nearly equal bands with one phase discontinuity. $\hbar\omega_{\mathrm{D}} = 0.09$, $N_1(0) = 0.3$, $N_2(0) = 0.21$, $N_3(0) = 0.22$, $g_{\nu\nu} = 0.7$, $g_{12} = -0.11$, $g_{13} = -0.1$. (a)-(c) The gaps in bands 1-3, $|\Delta_\nu|$, respectively. (d)-(f) The phase difference between the gaps. (d) $\phi_1 - \phi_2$. (e) $\phi_2 - \phi_3$. (f) $\phi_3 - \phi_1$.

formulas given in [143].

3.4.1   Free Energy Density

In the absence of an applied magnetic field, the electronic contribution to the free energy density of a multiband superconductor can be written as

$$\mathrm{F}_{\mathrm{s0}} = \vec{\Delta}^* \cdot \breve{g}^{-1} \cdot \vec{\Delta} + k_{\mathrm{B}}T \sum_\nu \int \mathrm{d}\varepsilon \, N_\nu(\varepsilon) \ln\left(f_\nu(\varepsilon)(1 - f_\nu(\varepsilon)) \right), \qquad (3.38)$$

with $f_\nu(\varepsilon)$ the modified Fermi function given by

$$f_\nu(\varepsilon) = \frac{1}{1 + \exp\left(\frac{\sqrt{\varepsilon^2 + |\Delta_\nu|^2}}{k_{\mathrm{B}}T} \right)}. \qquad (3.39)$$

Note that minimising the free energy with respect to $\vec{\Delta}^*$ with the approximation $N_\nu(\varepsilon) \approx N_\nu(0)$ recovers the self-consistent BCS equations. This approximation is appropriate as only states near the Fermi energy contribute appreciably to the integral at low temperatures. We also see that when the gaps are set to zero, the result is the normal state free energy. This confirms the form of the free energy density.

The free energy density of the normal state can be found in the same way by setting the gap to zero. Therefore the difference in the free energy densities of the superconducting and normal states is given by

$$\delta\mathrm{F}_0 = \vec{\Delta}^* \cdot \breve{g}^{-1} \cdot \vec{\Delta} - k_\mathrm{B}T \sum_\nu \int \mathrm{d}\varepsilon \, N_\nu(\varepsilon) \ln \left(\frac{1 + \cosh\left(\sqrt{\varepsilon^2 + |\Delta_\nu|^2}/k_\mathrm{B}T\right)}{1 + \cosh\left(\varepsilon/k_\mathrm{B}T\right)}\right). \tag{3.40}$$

3.4.2 Thermodynamic Critical Field

The thermodynamic critical field H_c can be found from the condensation energy of the superconductor, i.e. the difference in the free energy between the superconducting and normal states.

$$\frac{1}{8\pi}H_\mathrm{c}^2 = \delta F_0$$
$$= \vec{\Delta} \cdot \breve{g}^{-1} \cdot \vec{\Delta}$$
$$- 2k_\mathrm{B}T \sum_\nu N_\nu(0) \int_0^{\hbar\omega_\mathrm{D}} \mathrm{d}\varepsilon \, \ln \left(\frac{1 + \cosh\left(\sqrt{\varepsilon^2 + |\Delta_\nu|^2}/k_\mathrm{B}T\right)}{1 + \cosh\left(\varepsilon/k_\mathrm{B}T\right)}\right). \tag{3.41}$$

As in the one-band case, the critical field decays linearly to zero near T_c. However, due to the sudden increase in the smaller band at a lower temperature, the critical field in the two-band case can increase above the linear approximation.

At low interband coupling the critical field is the sum of two one-band results, with a very noticeable sudden increase near the second temperature $T_{2\mathrm{c}}$, due to the change from an induced to an intrinsic gap in the subdominant band. Observation of this feature provides easily accessible evidence of multiband superconductivity. At large interband coupling the temperature dependence of the critical field approximates that of a one-band material with a larger density of states.

3.4.3 Specific Heat Capacity

To find the specific heat it is easiest to first find the entropy. This has the form

$$S = -2T \sum_\nu N_\nu(0) \int_{-\infty}^{\infty} \mathrm{d}\varepsilon \, \left[(1 - f_\nu(\varepsilon)) \ln\left(1 - f_\nu(\varepsilon)\right) + f_\nu(\varepsilon) \ln\left(f_\nu(\varepsilon)\right)\right]. \tag{3.42}$$

At $T = T_\mathrm{c}$ the gaps go to zero. This allows the entropy at this point can be calculated explicitly, with the result

$$S(T_\mathrm{c}) = \frac{4\pi^2 T_\mathrm{c} \sum_\nu N_\nu(0)}{6}. \tag{3.43}$$

The specific heat is related to the entropy in the usual way,

$$C_v = T\frac{\partial S}{\partial T}. \tag{3.44}$$

However, since we only have the entropy at discrete temperatures, this needs to be approximated by a discrete derivative.

While this is useful for calculating the general form of the heat capacity over all temperatures, it unfortunately does not allow us to resolve the jump discontinuity in the heat capacity due to the TRSB phase transition. However, we can see from the definition of the heat capacity and the entropy that a discontinuity in the derivative of the gap should lead to a jump in the heat capacity, confirming that the TRSB transition is a phase transition rather than a crossover.

3.4.4 Results

In figure 3.11 these thermodynamic observables are plotted as a function of temperature with changing interband coupling. For these plots we use the parameters $g_{11} = 0.6$, $g_{22} = 0.5$, $N_1(0) = N_2(0) = 0.3$. Similar plots are also given in figure 3.11, where instead the density of states of the second band is varied, with the parameters $g_{11} = 0.6$, $g_{22} = 0.5$, $g_{12} = 0.01$, $N_1(0) = 0.6$.

In figure 3.11 (a) the critical magnetic field is plotted. When the bands are decoupled, the total critical field is just the critical field of two one-band models. This is seen as a slight anomaly in the slope. However with the second gap being so much weaker in this case, the deviation is fairly small. At intermediate coupling, the anomaly is smoothed over the central region. However the critical field at low temperatures is enhanced over that expected from the behaviour near T_c. At large interband coupling, the total critical field approaches that of a one-band model with a higher density of states.

In figure 3.12 (a) the two-band nature is most evident for $N_2(0) = 0.6$, as at this point the critical temperature of the uncoupled second band is about $0.5T_c$, and the deviation is strong.

Note that in the last sample, $N_2(0) = 0.8$, the second band becomes the dominant band, causing a sudden increase in the critical temperature. Since the critical temperature was included in the scaling, this causes this sample to not follow the general pattern seen in the other plots.

The entropy is shown for typical values in figure 3.11 (b) and figure 3.12 (b). Other than the discontinuous derivative in the uncoupled case in figure 3.11 this
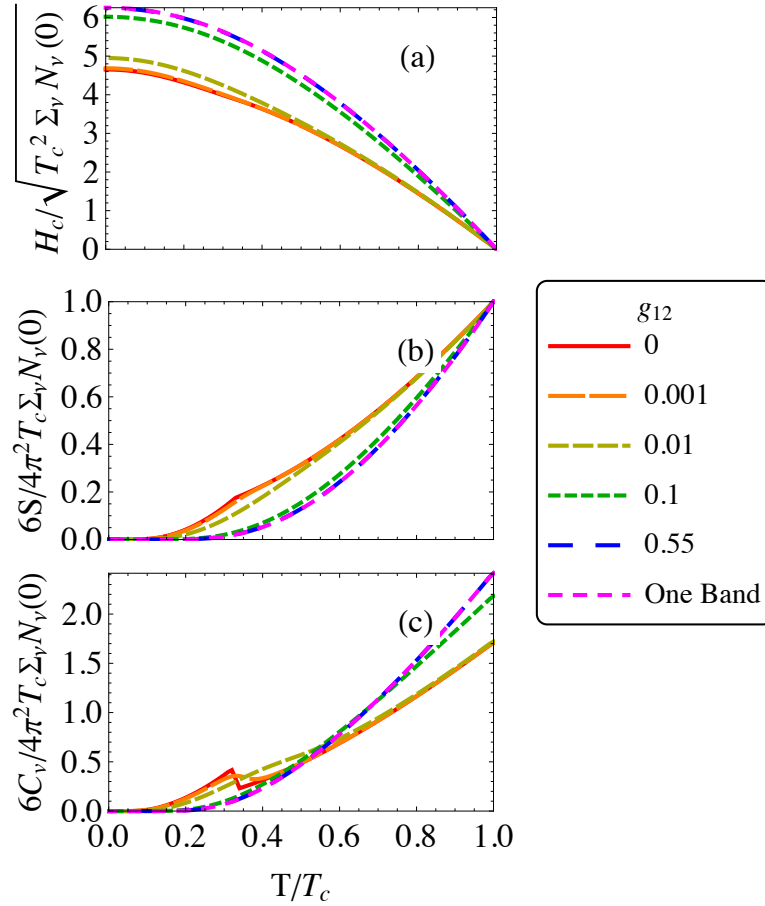
Figure 3.11: A selection of thermodynamic functions for a two-band superconductor showing the dependence on the interband coupling g_{12}. a) The thermodynamic critical field. b) The entropy. c) The specific heat. At large interband couplings, the observables approach the form of a one-band superconductor with density of states equal to the total density of states.

shows that the entropy in the two-band model is not vastly different from the one-band model, and this, combined with the fact that it is difficult to measure the entropy of a system, means that it is not possible to use this directly as evidence for multiband superconductivity.

In figure 3.11 (c) we see that initially there is an additional jump at about $T = 0.33T_c$ due to the appearance of the second band. As the interband coupling is increased, this jump transitions to a peak, then a shoulder. At large interband coupling, the heat capacity approaches the form of the one-band model.

In figure 3.12 (c) the heat capacity is shown for a weakly interacting system as the density of states of band 2 is increased. This clearly shows a shoulder in
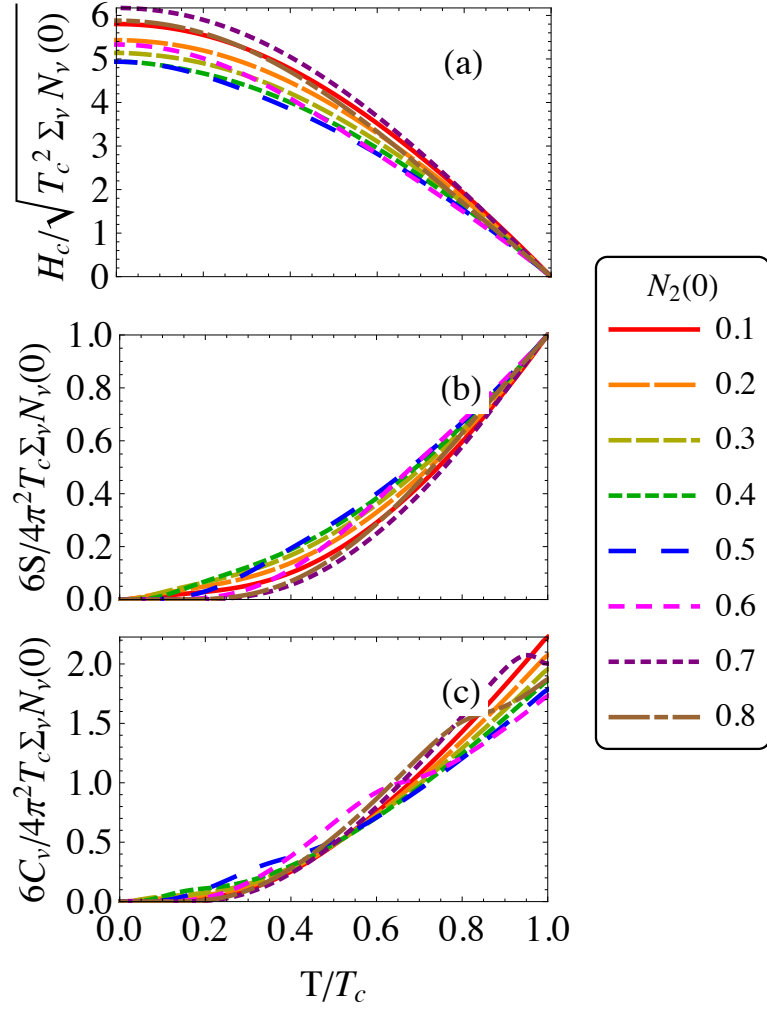
Figure 3.12: A selection of thermodynamic functions for two weakly interacting bands for a range of values of the density of states of the second band. a) The thermodynamic critical field. b) The entropy. c) The specific heat. A large shoulder is visible in most of the specific heat plots that is not visible in single band BCS theory. See for example $0.3T_c$ for $g_{12} = 0.5$, $0.6T_c$ for $g_{12} = 0.6$, and $0.95T_c$ for $g_{12} = 0.7$ (which in this case is more of a peak than a shoulder). These shoulders are most prominent when attempting to fit a one-band model to the data from a two-band superconductor.

the heat capacity, with only the location of the shoulder changing as the density of states changes. This feature of the heat capacity for weakly interacting two-band superconductors is one of the clearest experimental proofs for the existence of multiband superconductors. This shoulder has been seen in MgB_2 [76].

3.5 Summary

In this chapter we have generalised the BCS theory to multiband superconductors. We have shown how the self-consistent BCS equations generalise to the multiband theory. From this we have shown how to calculate the critical temperature and the magnitude of the gap at zero temperature.

Numerical solutions to the gap equations were then shown for the two-band case, showing how the interband interaction induces superconductivity in the smaller band above the one-band critical temperature. We also presented a perturbation expansion in this induced region which allows us to explicitly see how the smaller gap transitions to a lower critical temperature as the interband coupling goes to zero.

We then considered an application to three-band superconductors. We showed that in this case there are two additional related phenomena that are not seen in the two-band case – the gaps can move to the TRSB state where there is a nontrivial phase between the bands, and the gaps can go to zero below the critical temperature at the point T^0 as the phase between the bands switches. A method was presented which determined whether the ground state was the TRSB state, and gave the magnitude of the gaps in this case. This method reduces the problem of solving the full multiband BCS equations to the problem of solving three uncoupled one-band equations. The same approach also determines the existence and location of any T^0 points.

We presented a number of scans of the parameter space of the three-band BCS model and show that the regions calculated with this approach match the numerical calculations. This also shows which regions of parameter space are likely to exist in the TRSB state. The TRSB state only appears in a very small region of parameter space, where the interactions between the bands are of similar order. This allows the frustrated repulsive interaction to form the TRSB state. The frustrated repulsion also results in a lowering of the superconducting critical temperature T_c, and thus we expect to find these interesting properties near the minimum of T_c in parameter space. This is very useful for experimental searches for the existence of the TRSB state.

Finally we calculated a number of thermodynamic observables in the multiband BCS theory. We showed that the clearest observable which confirms the presence of multiband superconductors is the large shoulder that occurs in the heat capacity in weakly interacting multiband superconductors. We also argued that there is a

jump in the heat capacity at the transition to the TRSB state, indicating that this is indeed a phase transition.

CHAPTER FOUR

Multiband Ginzburg-Landau Theory

Multiband GL theory has existed since the work of Tilley [100] in two-band GL theory, but interest has been renewed in the theory only recently. The Ginzburg-Landau theory remains important even after the BCS theory due to its conceptual simplicity, computational speed, and applications to vortex and other magnetic states, while the strong connection to the more fundamental BCS theory enhances the reliability of the results.

In this chapter we look at two formulations of multiband GL theory. First we look at what we call traditional multiband GL theory. This has the same form as the theory as originally proposed by Tilley. This form looks very similar to the one-band model, with the addition of an interband coupling term and a band label on the order parameters. We also revisit some properties within this theory.

In addition we study an extended version of multiband GL theory, which is inspired by a series of papers by Peeters and co-workers [56–58], but the extension we employ goes much further in the order of corrections found. We use this to investigate the suggestion by Komendová et al. [119] that there exists a hidden criticality in multiband superconductors below the critical temperature. To the best of our knowledge this is the first time an investigation of these high order corrections has been performed in either the one-band or multiband theory.

4.1 Traditional Multiband Ginzburg-Landau Theory

4.1.1 The Multiband Ginzburg-Landau Equations

To find the multiband GL equations, the standard approach is to follow the phenomenological approach used to find the one-band equations. To do this, we argue that the free energy can again be expanded, as before, in a series in the order parameters. We assign one order parameter to each superconducting band. As in the one-band case, we truncate the free energy at fourth order.

In addition to the terms that appear in the one-band model, a Josephson interband coupling term is also included. This term is reminiscent of the Josephson coupling term which arises when two superconductors are separated in real space by a thin insulating material, where the Josephson coupling term would allow Cooper pairs to tunnel through the insulator and into the other superconductor. The same picture is applicable to the multiband superconductors, where the bands are instead separated in momentum space, and the Cooper pairs tunnel between the Fermi sheets.

There is also the possibility of including other interband coupling terms, such as density-density, and gradient-gradient coupling terms. These are not ruled out by symmetry arguments about the free energy, however we neglect them here as we shall see that these do not arise in clean multiband superconductors, as confirmed by the Gor'kov connection to multiband BCS theory. These do need to be considered in the theory of dirty superconductors, or if other coupling terms are included in the microscopic Hamiltonian.

With the inclusion of the additional coupling term, the free energy density can be expanded in an analogous way to the one-band theory, with the form

$$
\begin{aligned}
\mathrm{F_s} = \mathrm{F_{n0}} &+ \frac{\mathbf{B(r)}^2}{8\pi} + \sum_\nu \left[a_\nu \left| \Psi_\nu(\mathbf{r}) \right|^2 + \frac{1}{2} b_\nu \left| \Psi_\nu(\mathbf{r}) \right|^4 + \frac{1}{2m_\nu^*} \left| \Pi(\mathbf{r}) \Psi_\nu(\mathbf{r}) \right|^2 \right] \\
&+ \sum_{\nu' < \nu} \gamma_{\nu\nu'} \left(\Psi_\nu^*(\mathbf{r}) \Psi_{\nu'}(\mathbf{r}) + \Psi_{\nu'}^*(\mathbf{r}) \Psi_\nu(\mathbf{r}) \right),
\end{aligned}
\tag{4.1}
$$

where

$$
\Pi(\mathbf{r}) = \left(-\mathrm{i}\hbar\nabla + \frac{e^*\mathbf{A(r)}}{c} \right),
\tag{4.2}
$$

$$
\mathbf{B(r)} = \nabla \times \mathbf{A(r)},
\tag{4.3}
$$

and we have introduced the band index ν on the coefficients as well as on the order parameters. $\gamma_{\nu\nu'}$ will be termed the interband coupling, and when considering the two-band case will sometimes be written simply as γ.

The Gibbs free energy is found by the usual transformation. Making variations of the Gibbs free energy with respect to the complex conjugate of the order parameters, $\Psi_\nu^*(\mathbf{r})$, and the vector potential, $\mathbf{A}(\mathbf{r})$, then setting the result equal to zero,

$$\frac{\delta \mathrm{G}_\mathrm{s}}{\delta \Psi_\nu^*} = 0, \tag{4.4a}$$

$$\frac{\delta \mathrm{G}_\mathrm{s}}{\delta \mathbf{A}} = 0, \tag{4.4b}$$

we find the multiband GL equations.

$$a_\nu \Psi_\nu(\mathbf{r}) + b_\nu \left|\Psi_\nu(\mathbf{r})\right|^2 \Psi_\nu(\mathbf{r}) + \frac{1}{2m_\nu^*}\Pi(\mathbf{r})^2\Psi_\nu(\mathbf{r}) + \sum_{\nu' \neq \nu} \gamma_{\nu\nu'}\Psi_\nu'(\mathbf{r}) = 0, \tag{4.5a}$$

$$\frac{c}{4\pi}\nabla \times \nabla \times \mathbf{A}(\mathbf{r}) = $$
$$\sum_\nu \left[-\frac{e^*\hbar}{2im_\nu^*}\left(\Psi_\nu^*(\mathbf{r})\nabla\Psi_\nu(\mathbf{r}) - \Psi_\nu(\mathbf{r})\nabla\Psi_\nu^*(\mathbf{r})\right) - \frac{e^{*2}}{m_\nu^* c}\left|\Psi_\nu(\mathbf{r})\right|^2 \mathbf{A}(\mathbf{r})\right]. \tag{4.5b}$$

This also produces the boundary conditions

$$\hat{\mathbf{n}} \cdot \left(-\mathrm{i}\hbar\nabla + \frac{e^*\mathbf{A}}{c}\right)\Psi_\nu = 0, \tag{4.6a}$$

$$\hat{\mathbf{n}} \times (\mathbf{B}(\mathbf{r}) - \mathbf{H}(\mathbf{r})) = 0, \tag{4.6b}$$

where $\hat{\mathbf{n}}$ is the unit normal to the surface. Note that these boundary conditions are identical to the boundary conditions found in the one-band case, with the addition of the subscript ν on the order parameters.

Comparing equation (4.5b) with Ampere's law, we can identify the supercurrents associated with each of the bands

$$\mathbf{j}_\nu(\mathbf{r}) = -\frac{ie^*\hbar}{2m_\nu^*}\left(\Psi_\nu^*(\mathbf{r})\nabla\Psi_\nu(\mathbf{r}) - \Psi_\nu(\mathbf{r})\nabla\Psi_\nu^*(\mathbf{r})\right) - \frac{e^{*2}}{m_\nu^* c}\left|\Psi_\nu(\mathbf{r})\right|^2 \mathbf{A}(\mathbf{r}). \tag{4.7}$$

The problem with this approach to the derivation of multiband GL is that, unlike in the one-band theory, it is not clear what temperature dependence to assign to the coefficients. We expect that the temperature dependence of a should still be linear, and b should be a constant, but it is not clear what temperature dependence should be included in γ, or the exact temperature dependence of a. To overcome this we need to connect the multiband GL to the multiband BCS theory.

4.1.2   Multiband BCS Theory To Multiband GL Theory

It is possible to link the microscopic multiband BCS theory to the multiband GL theory by repeating the Gor'kov technique. To perform this connection, we begin with the equations of motion for the superconducting Green function, $\mathscr{G}_{\nu,\omega_n}$, the anomalous Green function, $\mathscr{F}_{\nu,\omega_n}$, and a normal state Green function, $\mathcal{G}_{\nu,\omega_n}$,

$$\left[\mathrm{i}\hbar\omega_n - \frac{1}{2m_\nu}\Pi(\mathbf{r})^2 + \mu_\nu\right]\mathscr{G}_{\nu,\omega_n}(\mathbf{r},\mathbf{r}') + \Delta_\nu(\mathbf{r})\mathscr{F}^\dagger_{\nu,\omega_n}(\mathbf{r},\mathbf{r}') = \hbar\delta(\mathbf{r}-\mathbf{r}'), \qquad (4.8a)$$

$$\left[-\mathrm{i}\hbar\omega_n - \frac{1}{2m_\nu}\Pi(\mathbf{r})^2 + \mu_\nu\right]\mathscr{F}^\dagger_{\nu,\omega_n}(\mathbf{r},\mathbf{r}') - \Delta^*_\nu(\mathbf{r})\mathscr{G}_{\nu,\omega_n}(\mathbf{r},\mathbf{r}') = 0, \qquad (4.8b)$$

$$\left[\mathrm{i}\hbar\omega_n - \frac{1}{2m_\nu}\Pi(\mathbf{r})^2 + \mu_\nu\right]\mathcal{G}_{\nu,\omega_n}(\mathbf{r},\mathbf{r}') = \hbar\delta(\mathbf{r}-\mathbf{r}'). \qquad (4.8c)$$

Note that there is no direct coupling of the band gaps in this differential form – each of the equations only contains a single band index ν. We may rewrite this as a set of coupled integral equations, which we can interpret as an expansion in Δ_ν, which we truncate at order Δ_ν^3. The Green function and the anomalous Green function may then be written as

$$\mathscr{G}_{\nu,\omega_n}(\mathbf{r},\mathbf{r}') = \mathcal{G}_{\nu,\omega_n}(\mathbf{r},\mathbf{r}')$$
$$- \hbar^{-2}\int \mathrm{d}\mathbf{y}\int \mathrm{d}\mathbf{z}\,\mathcal{G}_{\nu,\omega_n}(\mathbf{r},\mathbf{y})\Delta_\nu(\mathbf{y})\widetilde{\mathcal{G}}_{\nu,\omega_n}(\mathbf{y},\mathbf{z})\Delta^*_\nu(\mathbf{z})\mathcal{G}_{\nu,\omega_n}(\mathbf{z},\mathbf{r}'),$$

$$(4.9a)$$

$$\mathscr{F}^\dagger_{\nu,\omega_n}(\mathbf{r},\mathbf{r}') = \hbar^{-1}\int \mathrm{d}\mathbf{y}\,\widetilde{\mathcal{G}}_{\nu,\omega_n}(\mathbf{r},\mathbf{y})\Delta^*_\nu(\mathbf{y})\mathcal{G}_{\nu,\omega_n}(\mathbf{y},\mathbf{r}')$$
$$- \hbar^{-3}\int \mathrm{d}\mathbf{y}\int \mathrm{d}\mathbf{z}\int \mathrm{d}\mathbf{w}\,\widetilde{\mathcal{G}}_{\nu,\omega_n}(\mathbf{r},\mathbf{y})\Delta^*_\nu(\mathbf{y})\mathcal{G}_{\nu,\omega_n}(\mathbf{y},\mathbf{z})\Delta_\nu(\mathbf{z}) \qquad (4.9b)$$
$$\times\,\widetilde{\mathcal{G}}_{\nu,\omega_n}(\mathbf{z},\mathbf{w})\Delta^*_\nu(\mathbf{w})\mathcal{G}_{\nu,\omega_n}(\mathbf{w},\mathbf{r}').$$

Now, all of these integrals are only dependent on individual bands. Therefore we can compute these integrals in the same way as the one-band theory. There are two main differences with the one-band theory. One occurs when we impose the self-consistency condition:

$$\sum_{\nu'} g^{-1}{}_{\nu\nu'}\Delta^*_{\nu'} = \frac{1}{\beta\hbar}\lim_{\eta\to0^+}\sum_n \mathrm{e}^{-\mathrm{i}\omega_n\eta}\mathscr{F}^\dagger_{\nu,\omega_n}(\mathbf{r},\mathbf{r}), \qquad (4.10)$$

where now the left-hand side of the self-consistency condition couples the gaps in the separate bands.

The second is in the evaluation of the a term. In the one-band theory we found a term $N(0)\mathcal{A}\Delta$ (equation (2.70)), with $\mathcal{A} = \ln\left(\frac{2\hbar\omega_\mathrm{D}\mathrm{e}^\Gamma}{\pi k_\mathrm{B}T_\mathrm{c}}\right)$, and then used the BCS result (equation (2.54)) to evaluate this to $g^{-1}\Delta$. In the multiband case we also

have a term $N_\nu(0)\mathcal{A}\Delta_\nu$, however we cannot make the same identification because the analogous result does not hold. Instead we must retain the full form.

With the same approximations as in the one-band method, the self-consistent gap equation may be written as

$$\sum_{\nu'} g^{-1}{}_{\nu\nu'}\Delta_{\nu'}(\mathbf{r}) = N_\nu(0)\left(\frac{7\zeta(3)\epsilon_F^0}{6\pi^2(k_BT_c)^2}\frac{1}{4m_\nu}\Pi(\mathbf{r})^2\right.$$
$$\left. + \left(1 - \frac{T}{T_c} + \mathcal{A}\right) + \frac{7\zeta(3)}{8\pi^2(k_BT_c)^2}|\Delta_\nu(\mathbf{r})|^2\right)\Delta_\nu(\mathbf{r}). \quad (4.11)$$

In one-band GL, the term $g^{-1}\Delta$ cancels off exactly with the term $N(0)\mathcal{A}\Delta$. We then remove the overall scale $N(0)$, and identify the resulting equation with the GL equation for the order parameter. In the multiband case however, this term does not cancel off exactly. To maintain the same units as the one-band GL theory, we could divide through by $N_\nu(0)$. However, this prevents the interband coupling from being symmetric. Instead we divide the resulting equations by $N_T(0) = \sum_\nu N_\nu(0)$.

Comparing this to the GL equations, we identify the following values with the GL parameters:

$$a_\nu = \frac{N_\nu(0)}{N_T(0)}\frac{6}{7\zeta(3)}\frac{\pi^2(k_BT_c)^2}{\epsilon_F^0}\left(1 - \frac{T}{T_c} + \mathcal{A} - \frac{g^{-1}{}_{\nu\nu}}{N_\nu(0)}\right), \quad (4.12\text{a})$$

$$b_\nu = \frac{N_\nu(0)}{N_T(0)}\frac{6}{7\zeta(3)}\frac{\pi^2(k_BT_c)^2}{\epsilon_F^0 n}, \quad (4.12\text{b})$$

$$\gamma_{\nu\nu'} = -\frac{6}{7\zeta(3)}\frac{\pi^2(k_BT_c)^2}{\epsilon_F^0}\frac{g^{-1}{}_{\nu\nu'}}{N_T(0)}, \quad (4.12\text{c})$$

$$\Psi_\nu = \left(\frac{7\zeta(3)n}{8\pi^2(k_BT_c)^2}\right)^{1/2}\Delta_\nu, \quad (4.12\text{d})$$

$$m_\nu^* = 2m_\nu\frac{N_T(0)}{N_\nu(0)}, \quad (4.12\text{e})$$

$$e^* = 2e. \quad (4.12\text{f})$$

Similar identification of the multiband GL with the BCS coefficients has been made by other authors [110, 144].

We see that the temperature dependence of $\gamma_{\nu\nu'}$ is a constant, and unlike the one-band case, the parameters a_ν do not disappear at the critical temperature due to the remaining terms not cancelling off. Instead, at the critical temperature, the remaining linear terms are equivalent to the equation for T_c in BCS,

$$\frac{6}{7\zeta(3)}\frac{\pi^2(k_BT_c)^2}{N_T(0)\epsilon_F^0}(\mathcal{A}\check{N}(0) - \check{g}^{-1})\cdot\vec{\Psi} = 0. \quad (4.13)$$

The determinant of the term in brackets was shown to go to zero at the critical temperature. This is therefore the highest temperature for which there is a nontrivial solution for the order parameters, and the order parameters go to zero at this point as expected.

The procedure for the derivation of the GL equation for the vector potential follows through in exactly the same way as for the one-band theory. The Green functions are each related to a supercurrent. These are then summed over to find the total current, and then this is related to the vector potential through Ampere's law.

This connection to the BCS theory gives multiband GL microscopic support. The range of validity of the theory can be assessed correctly, and the assumptions implicit in the theory are now clear. The explicit form of the coefficients also allows the theory to be applied to real world parameters.

4.1.3 Bulk Solutions

Now that we have a correct form for the multiband GL equations, we wish to study their properties. We first look for uniform solutions. Setting $\mathbf{A}$ to zero, as well as all derivatives of Ψ, we get the bulk GL equations

$$a_\nu \Psi_\nu + b_\nu \left| \Psi_\nu \right|^2 \Psi_\nu + \sum_{\nu' \neq \nu} \gamma_{\nu\nu'} \Psi_\nu' = 0. \tag{4.14}$$

Writing the order parameters as a magnitude, f_ν, and phase factor, $e^{i\phi_\nu}$, we get two sets of equations by taking real and imaginary parts

$$a_\nu f_\nu + b_\nu f_\nu^3 + \sum_{\nu' \neq \nu} \gamma_{\nu\nu'} f_{\nu'} \cos(\phi_{\nu'} - \phi_\nu) = 0, \tag{4.15a}$$

$$\sum_{\nu' \neq \nu} \gamma_{\nu\nu'} f_{\nu'} \sin(\phi_{\nu'} - \phi_\nu) = 0. \tag{4.15b}$$

For the two-band case, the second equation only has a solution if the bands are entirely in phase or out of phase. Considering the free energy, we see that the most stable state is the one where $\gamma_{12} \cos(\phi_1 - \phi_2) < 0$.

We then have two equations to solve

$$0 = a_1 f_1 + b_1 f_1^3 - \left| \gamma_{12} \right| f_2, \tag{4.16a}$$

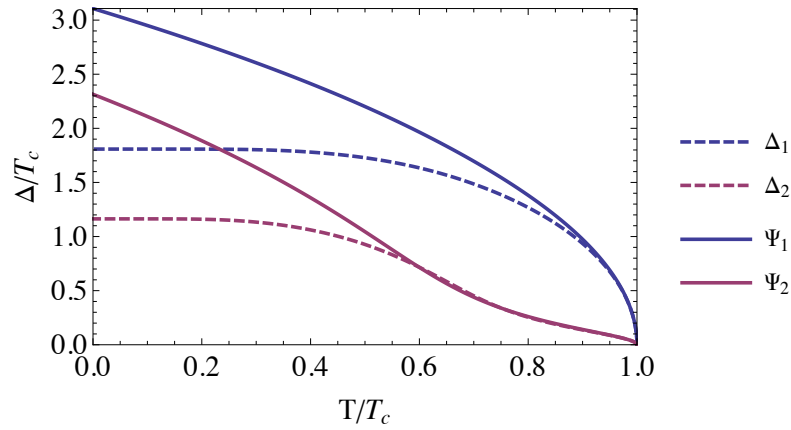$$0 = a_2 f_2 + b_2 f_2^3 - \left| \gamma_{21} \right| f_1. \tag{4.16b}$$

Figure 4.1: A solution to the two-band GL equations compared to the solution of the equivalent two-band BCS equations. The GL solution for the dominant band is only accurate very close to T_c, and is only reliable above about $0.95T_c$.

Letting $\chi = f_2/f_1$ and using $\gamma_{12} = \gamma_{21}$, we find

$$0 = a_1 + b_1 f_1^2 - |\gamma_{12}|\,\chi, \tag{4.17a}$$

$$0 = a_2\chi + \frac{b_2}{b_1}\chi^3(-a_1 + |\gamma_{12}|\,\chi) - |\gamma_{12}|\,, \tag{4.17b}$$

resulting in a quartic equation for χ, which can be solved exactly. Having found χ, we find the magnitude of the order parameters

$$f_1 = \sqrt{-a_1 + |\gamma_{12}|\,\chi}, \tag{4.18a}$$

$$f_2 = \chi\sqrt{-a_1 + |\gamma_{12}|\,\chi}$$

$$= \sqrt{-a_2 + |\gamma_{12}|\,/\chi}. \tag{4.18b}$$

An example of a two-band solution is shown in figure 4.1, and is compared to a BCS solution. The dominant band is largely unperturbed by the second band, and the region where the two theories agree is similar for this band. The second band seems to have a larger region of validity, but this is mostly coincidental. The difference between the two solutions oscillates around zero, with the GL solution passing above, below, and then above again before substantially diverging. The solution is only truly valid close to T_c.

With three or more bands, solutions can exist where the sin terms are not zero, but merely add up to zero (equation (4.15)). Therefore, with three or more bands, the relative phases of the gaps are not necessarily fixed to be 0 or π, but instead can take on any value that satisfies equation (4.15).

In cases where the gaps are not phase-locked, there exists at least two degenerate ground states. Changing the sign of all phase differences in equation (4.15) creates
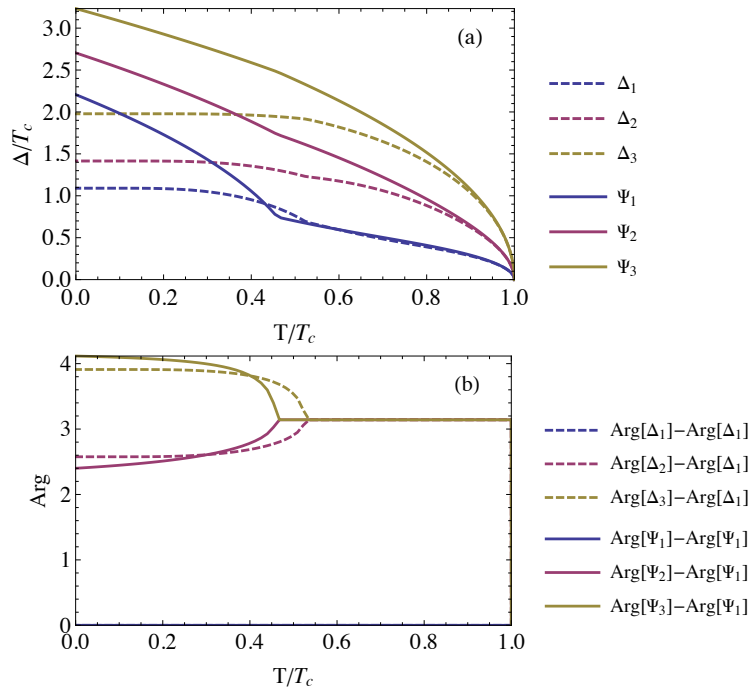
Figure 4.2: (a) A comparison of the three-band GL solution and a solution to the equivalent three-band BCS equations. (b) The phase of the gaps relative to the phase of the first gap in the BCS and GL models. In the standard superconducting state the phases are locked at π. At the TRSB phase transition the phases evolve to other values. While the GL solution is only valid very close to T_c, the GL solution correctly predicts the emergence of the TRSB state, though it disagrees with the precise location of the transition.

another solution to these equations due to the symmetric (antisymmetric) nature of cos (sin). These are the GL states corresponding to the TRSB states we saw in multiband BCS theory.

This configuration is seen in figure 4.2 where a three-band GL solution with a TRSB transition is compared to the BCS solution. The GL solution again only agrees quantitatively with the BCS result near T_c. However both show a TRSB transition near $0.5T_c$, where a discontinuity in the derivative is visible. This is also visible in the relative phase plots in b). But the precise location of the transition in the GL theory does not match the location in the BCS theory.

4.1.4   Interface Solution, Decay Lengths and Surface Energy

The simplest nonuniform solution of the multiband GL equations is a semi-infinite superconductor in equilibrium with a semi-infinite normal metal, where an applied magnetic field suppresses superconductivity in the normal metal.

We can again find a surface free energy of such a solution. To do so we introduce

the ansatz solutions

$$\Psi_\nu(\mathbf{r}) = \Psi_\nu(z), \tag{4.19a}$$

$$\mathbf{A}(\mathbf{r}) = A(z)\hat{\mathbf{e}}_x. \tag{4.19b}$$

Putting these into the GL equations, we find

$$0 = -\frac{\hbar^2}{2m_\nu^*}\frac{\mathrm{d}^2\Psi_\nu(z)}{\mathrm{d}z^2} + A^2(z)\Psi_\nu(z) + a_\nu\Psi_\nu(z) + b_\nu\left|\Psi_\nu(z)\right|^2\Psi_\nu(z)$$
$$+ \sum_{\nu'\neq\nu}\gamma_{\nu\nu'}\Psi_{\nu'}(z), \tag{4.20a}$$

$$0 = \frac{c}{4\pi}\frac{\mathrm{d}^2A(z)}{\mathrm{d}z^2} - \sum_\nu\frac{e^{*2}}{m_\nu^* c}\left|\Psi_\nu(z)\right|^2 A(z). \tag{4.20b}$$

We examine these equations in two limits in order to find the coherence length and the penetration depth. First we consider equation (4.20b) for the case where the order parameters are fixed at their equilibrium values, $\Psi_{\nu 0}$. We immediately see that the length scale of interest is

$$\lambda = \sqrt{\frac{c^2}{4\pi e^{*2}\sum_\nu\left|\Psi_{\nu 0}\right|^2/m_\nu^*}}. \tag{4.21}$$

This can be written in the simpler form

$$\lambda = \left(\sum_\nu\frac{1}{\lambda_\nu^2}\right)^{-1/2}, \tag{4.22}$$

$$\lambda_\nu = \sqrt{\frac{c^2 m_\nu^*}{4\pi e^{*2}\left|\Psi_{\nu 0}\right|^2}}. \tag{4.23}$$

In this form it is evident how the penetration depths from the individual bands combine to produce a single penetration depth for the material. Note however that the multiband nature has an effect on the individual penetration depths through the dependence on the bulk values of the order parameters, $\Psi_{\nu 0}$.

The method to find the coherence length is more procedural. We will again assume that the superconductor is not in the TRSB state and that the relative phases of the order parameters are fixed to be in phase or out of phase. We then make an ansatz for the long range behaviour of the order parameters

$$\Psi_\nu(z) = \Psi_{\nu 0} + c_\nu\exp\left(\frac{\sqrt{2}z}{\xi}\right), \tag{4.24}$$

where $\Psi_{\nu 0}$ are chosen to satisfy the uniform GL equations, and the factor of $\sqrt{2}$ is chosen so that the one-band result reproduces the standard one-band coherence

length. Putting this into equation (4.20a) and retaining only the leading order terms results in the equations

$$-\frac{\hbar^2}{m_\nu^* \xi^2} c_\nu + a_\nu c_\nu + b_\nu \left(2 \left| \Psi_{\nu 0} \right|^2 c_\nu + \Psi_{\nu 0}^2 c_\nu^* \right) + \sum_{\nu' \neq \nu} \gamma_{\nu\nu'} c_{\nu'} = 0. \tag{4.25}$$

If the phase of c_ν is the same as $\Psi_{\nu 0}$, then this reduces to the simpler form

$$\left(-\frac{\hbar^2}{m_\nu^* \xi^2} + a_\nu + 3 b_\nu \left| \Psi_{\nu 0} \right|^2 \right) c_\nu + \sum_{\nu' \neq \nu} \gamma_{\nu\nu'} c_{\nu'} = 0, \tag{4.26}$$

which then needs to be solved for the coherence length ξ. Defining the $\vec{c}$ to be a vector with components c_ν and $\check{M}$ to be a matrix with the components

$$M_{\nu\nu'} = \begin{cases} -\frac{\hbar^2}{m_\nu^* \xi^2} + a_\nu + 3 b_\nu \left| \Psi_{\nu 0} \right|^2, & \nu = \nu', \\ \gamma_{\nu\nu'}, & \nu \neq \nu', \end{cases} \tag{4.27}$$

we can rewrite this simply as

$$\check{M} \cdot \vec{c} = 0. \tag{4.28}$$

Since we require nontrivial solutions, we therefore choose ξ to be the largest solution such that

$$\det(\check{M}) = 0. \tag{4.29}$$

In the two-band case, the resulting equation for the coherence length can be written as

$$\left(a_1 + 3 b_1 \left| \Psi_{10} \right|^2 - \frac{\hbar^2}{m_1^* \xi^2} \right) \left(a_2 + 3 b_2 \left| \Psi_{20} \right|^2 - \frac{\hbar^2}{m_2^* \xi^2} \right) - \gamma_{12}^2 = 0. \tag{4.30}$$

This has two positive solutions, and we identify the largest of these with the coherence length.

As in the one-band case, we can define the surface free energy per unit area by a line integral of the Gibbs free energy minus the Gibbs free energy of the superconducting state [131, 145]

$$\sigma_{\mathrm{ns}} = \int_{-\infty}^{\infty} \mathrm{d}z \left[\mathrm{G}(z) - \mathrm{G}_{\mathrm{n0}} + \frac{H_{\mathrm{c}}^2}{8\pi} \right] = \int_{-\infty}^{\infty} \mathrm{d}z \left[\mathrm{G}(z) - \mathrm{G}_{\mathrm{s0}} \right]$$

$$= \int_{-\infty}^{\infty} \mathrm{d}z \sum_\nu \left[a_\nu \left| \Psi_\nu(\mathbf{r}) \right|^2 + \frac{1}{2} b_\nu \left| \Psi_\nu(\mathbf{r}) \right|^4 + \frac{1}{2m_\nu^*} \left| \Pi(\mathbf{r}) \Psi_\nu(\mathbf{r}) \right|^2 \right.$$

$$\left. + \sum_{\nu' < \nu} \gamma_{\nu\nu'} \left(\Psi_\nu^*(\mathbf{r}) \Psi_{\nu'}(\mathbf{r}) + \Psi_{\nu'}^*(\mathbf{r}) \Psi_\nu(\mathbf{r}) \right) + \frac{1}{8\pi} \left(H_{\mathrm{c}} - B(z) \right)^2 \right]. \tag{4.31}$$

This can be simplified by multiplying equation (4.5a) by $\Psi_\nu^*(\mathbf{r})$, summing over ν and integrating over all z to find

$$
\begin{aligned}
0 = \int_{-\infty}^{\infty} \mathrm{d}z \sum_\nu & \left[a_\nu \left| \Psi_\nu(\mathbf{r}) \right|^2 + b_\nu \left| \Psi_\nu(\mathbf{r}) \right|^4 + \frac{1}{2m_\nu^*} \left| \Pi(\mathbf{r}) \Psi_\nu(\mathbf{r}) \right|^2 \right. \\
& \left. + \sum_{\nu' < \nu} \gamma_{\nu\nu'} \left(\Psi_\nu^*(\mathbf{r}) \Psi_{\nu'}(\mathbf{r}) + \Psi_{\nu'}^*(\mathbf{r}) \Psi_\nu(\mathbf{r}) \right) \right].
\end{aligned}
\tag{4.32}
$$

Then, subtracting this from equation (4.31), we find the surface free energy may be written as

$$
\sigma_{\mathrm{ns}} = \int_{-\infty}^{\infty} \mathrm{d}z \left[-\frac{1}{2} \sum_\nu b_\nu \left| f_\nu(z) \right|^4 + \frac{1}{8\pi} \left(H_{\mathrm{c}} - B(z) \right)^2 \right].
\tag{4.33}
$$

Then, deep in the normal material, we know that the order parameters go to zero. To calculate the field strength, we note that deep in the normal material, there is no contribution to the surface free energy. This gives us the boundary condition

$$
B(-\infty) = H_{\mathrm{c}}.
\tag{4.34}
$$

Similarly, there is no contribution to the surface deep in the superconductor. This allows us to calculate the critical field H_{c}

$$
\frac{H_{\mathrm{c}}^2}{8\pi} = \frac{1}{2} \sum_\nu b_\nu \left| f_{\nu 0} \right|^4.
\tag{4.35}
$$

The supercurrent at the multiband superconductor-normal material interface is

$$
\mathbf{j}_\nu(\mathbf{r}) = -\frac{1}{2m_\nu^*} \left| \Psi_\nu \right|^2 (z) A(z) \hat{\mathbf{e}}_x.
\tag{4.36}
$$

As in the one-band case, the multiband GL equations can be solved numerically in one-dimension with appropriate boundary conditions to find the behaviour of the order parameters in a magnetic field induced normal-superconductor interface. One such solution is shown in figure 4.3. While we have shown that deep within the superconducting state there exists a single coherence length and penetration depth, it is clear that in the interface region a number of different length scales can exist, and these interact in a complex way.

Varying the various parameters can affect the stability of the interface solution. An example of the dependence of the surface free energy, σ_{ns}, on the interband coupling strength, γ, for one set of parameters is shown in figure 4.4. In this example, creating additional interfaces is favoured over a uniform solution at low interband coupling, but the absence of interfaces is favoured at high interband coupling.
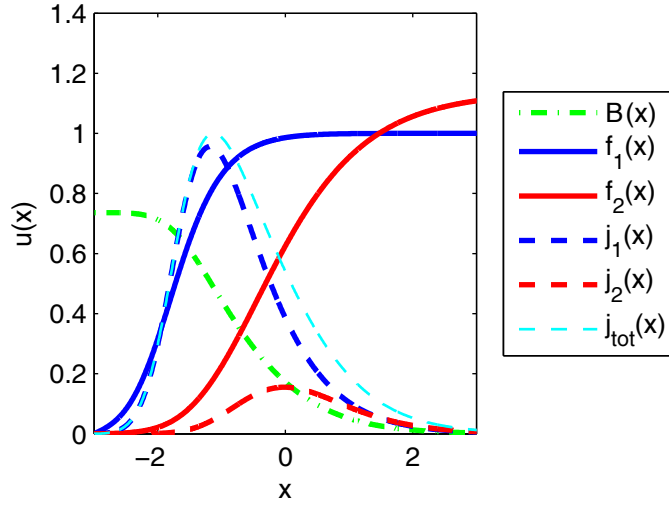
Figure 4.3: An interface solution to the two-band GL equations. This shows the supercurrent in each band flowing along the interface, the decay of the magnetic field into the bulk of the superconductor and the decay of the order parameters. The interface is the region where these variables are changing. Note that the locations of the peaks in the supercurrents occur at separate locations due to the different effective length scales in this region.
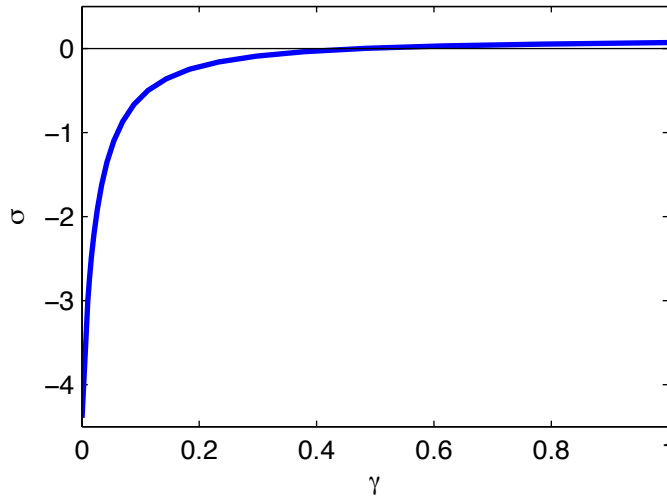

Figure 4.4: A plot of the surface free energy as a function of the interband Josephson coupling strength γ for two-band GL. This shows that a change in the interband coupling strength can change the stability of domain walls.

4.1.5 Summary

So far we have outlined the key aspects of traditional multiband GL theory. This theory has many advantages – it is conceptually simple, has the same qualitative features as multiband BCS theory, including the TRSB state, and is able to describe vortex states, which will be discussed in chapter 5.

The parameter space is far more diverse than the one-band theory. In one-band, the theory can be scaled in a simple way, revealing that there is only one fundamental parameter, the Ginzburg-Landau parameter, κ. No such scaling exists in the general multiband theory, and in the two-band theory four parameters remain after scaling.

The disadvantages of this theory are that it is only valid near T_c and usually overestimates the gaps at low temperature. For an arbitrary number of bands, even in the uniform limit, we must resort to numerics to solve for the order parameter, and this must be done separately for each temperature. Additionally, while it predicts the TRSB transition, the precise location of the transition does not agree with the multiband BCS prediction.

The other main issue with traditional multiband GL theory is that it includes some contributions to the gap function which are of order greater than $\tau^{1/2}$, which is what the theory claims to be accurate to. This is clear from the plots of the gaps as a function of temperature – the gaps are more complex than in the one-band case. This was pointed out by Kogan and Schmalian [126], where the authors showed that by neglecting the higher order corrections (which should be done since these corrections are not complete) the multiband equations reduce to a single equation which is identical to one-band GL.

4.2 Extended Ginzburg-Landau Theory

To achieve better agreement between multiband BCS and GL theories we would like to look for an extended GL theory. Extending traditional multiband GL theory to include higher orders in τ is difficult and must be calculated from scratch. The resulting equations cannot be solved analytically and must be solved numerically for each temperature.

An alternative approach proposed in a series of papers [56–58] re-derives the multiband GL theory from the BCS theory, keeping terms of order $\tau^{3/2}$ and dropping all higher order contributions. The approach outlined in the papers suggest that this method should be able to be extended to arbitrary order.

Inspired by this approach, we investigated this extension of multiband GL theory [2]. We performed this procedure for the uniform GL case and retained terms to very high order. This is the first time that these high order corrections to the expansion have been obtained.

4.2.1 Derivation of Extended Ginzburg-Landau Theory

To find a theory which can be extended to arbitrary order, we return to the equations of motion for the Green function, $\mathscr{G}_{\nu,\omega_n}(\mathbf{r},\mathbf{r}')$, anomalous Green function, $\mathscr{F}^{\dagger}_{\nu,\omega_n}(\mathbf{r},\mathbf{r}')$ and the normal state Green function, $\mathcal{G}_{\nu,\omega_n}(\mathbf{r},\mathbf{r}')$. We again use the Gor'kov technique to rewrite these as a pair of coupled integral equations [36, 138]:

$$
\begin{aligned}
\mathscr{G}_{\nu,\omega_n}(\mathbf{r},\mathbf{r}') &= \mathcal{G}_{\nu,\omega_n}(\mathbf{r},\mathbf{r}') \\
&\quad - \hbar^{-1}\int \mathrm{d}\mathbf{y}\,\mathcal{G}_{\nu,\omega_n}(\mathbf{r},\mathbf{y})\Delta_\nu(\mathbf{y})\mathscr{F}^{\dagger}_{\nu,\omega_n}(\mathbf{y},\mathbf{r}'),
\end{aligned}
\tag{4.37a}
$$

$$
\mathscr{F}^{\dagger}_{\nu,\omega_n}(\mathbf{r},\mathbf{r}') = \hbar^{-1}\int \mathrm{d}\mathbf{y}\,\widetilde{\mathcal{G}}_{\nu,\omega_n}(\mathbf{r},\mathbf{y})\Delta^*(\mathbf{y})\mathscr{G}_{\nu,\omega_n}(\mathbf{y},\mathbf{r}'),
\tag{4.37b}
$$

where $\widetilde{\mathcal{G}}_{\nu,\omega_n}(\mathbf{r},\mathbf{y}) = \mathcal{G}_{\nu,-\omega_n}(\mathbf{y},\mathbf{r})$, $\Delta_\nu(\mathbf{r})$ is the superconducting gap function in band ν, and the fermionic Matsubara frequency $\omega_n = (2n+1)\frac{\pi}{\beta\hbar}$, with $\beta = 1/k_\mathrm{B}T$. The normal Green functions satisfy the equations

$$
\left[\mathrm{i}\hbar\omega_n + \frac{\hbar^2}{2m_\nu}\left(\nabla + \frac{\mathrm{i}e\mathbf{A}(\mathbf{r})}{\hbar c}\right)^2 + \mu_\nu\right]\mathcal{G}_{\nu,\omega_n}(\mathbf{r},\mathbf{r}') = \hbar\delta^3(\mathbf{r}-\mathbf{r}'),
\tag{4.38a}
$$

$$
\left[-\mathrm{i}\hbar\omega_n + \frac{\hbar^2}{2m_\nu}\left(\nabla - \frac{\mathrm{i}e\mathbf{A}(\mathbf{r})}{\hbar c}\right)^2 + \mu_\nu\right]\widetilde{\mathcal{G}}_{\nu,\omega_n}(\mathbf{r},\mathbf{r}') = \hbar\delta^3(\mathbf{r}-\mathbf{r}').
\tag{4.38b}
$$

Using substitution, we can transform equations (4.37a) and (4.37b) into decoupled nonlinear integral equations, and by continued substitution we can write the anomalous Green function as a series expansion in the gap and the normal Green function

$$
\mathscr{F}^{\dagger}_{\nu,\omega_n}(\mathbf{r},\mathbf{r}') = \sum_{m=0}^{\infty}\frac{(-1)^m}{\hbar^{2m+1}}\left(\prod_{i=1}^{2m+1}\int \mathrm{d}\mathbf{y_i}\right)\widetilde{\mathcal{G}}_{\nu,\omega_n}(\mathbf{r},\mathbf{y_1})\Delta^*_\nu(\mathbf{y_1})
$$

$$
\times \left(\prod_{j=1}^{m}\mathcal{G}_{\nu,\omega_n}(\mathbf{y_{2j-1}},\mathbf{y_{2j}})\Delta(\mathbf{y_{2j}})\widetilde{\mathcal{G}}_{\nu,\omega_n}(\mathbf{y_{2j}},\mathbf{y_{2j+1}})\Delta^*_\nu(\mathbf{y_{2j+1}})\right)\mathcal{G}_{\nu,\omega_n}(\mathbf{y_{2m+1}},\mathbf{r}').
\tag{4.39}
$$

The gap is defined in terms of the anomalous Green function by

$$
\sum_{\nu'}g^{-1}{}_{\nu\nu'}\Delta^*_{\nu'}(\mathbf{r}) = \lim_{\eta\to 0^+}\sum_n \mathrm{e}^{-\mathrm{i}\omega_n\eta}\frac{1}{\beta\hbar}\mathscr{F}^{\dagger}_{\nu,\omega_n}(\mathbf{r},\mathbf{r}).
\tag{4.40}
$$

By requiring the gap to satisfy equation (4.40), and taking the complex conjugate, we obtain the self-consistent gap equation in matrix form

$$
\breve{g}^{-1}\cdot\vec{\Delta}(\mathbf{r}) = \vec{R}(\mathbf{r}),
\tag{4.41}
$$

where $\check{g}$ is the interband coupling matrix with elements $g_{\nu,\nu'}$, $\vec{\Delta}$ is a column vector with elements Δ_ν, and $\vec{R}$ is a column vector with elements given by

$$R_\nu(\mathbf{r}) = \sum_{m=0}^{\infty} P_{\nu,m}(\mathbf{r}), \tag{4.42}$$

$$P_{\nu,m}(\mathbf{r}) = \lim_{\substack{\mathbf{y_0} \to \mathbf{r} \\ \mathbf{y_{2m+2}} \to \mathbf{r}}} \left(\prod_{j=1}^{2m+1} \int d\mathbf{y_j} \right) Q_{\nu,m}(\{\mathbf{y}\}_{2m+2}), \tag{4.43}$$

$$
\begin{aligned}
Q_{\nu,m}(\{\mathbf{y}\}_{2m+2}) = {} & \frac{(-1)^m}{\beta \hbar^{2(m+1)}} \Delta_\nu(\mathbf{y_1}) \\
& \times \prod_{q=1}^{m} \left(\Delta_\nu^*(\mathbf{y_{2q}}) \Delta_\nu(\mathbf{y_{2q+1}}) \right) \\
& \times \sum_n \prod_{j=0}^{m} \left(\mathcal{G}_{\nu,\omega_n}(\mathbf{y_{2j}}, \mathbf{y_{2j+1}}) \widetilde{\mathcal{G}}_{\nu,\omega_n}(\mathbf{y_{2j+1}}, \mathbf{y_{2j+2}}) \right),
\end{aligned}
\tag{4.44}
$$

with $\{\mathbf{y}\}_m = \{\mathbf{y_0}, \mathbf{y_1} \ldots, \mathbf{y_m}\}$. Equation (4.41) is a coupled equation involving the gaps from all bands, ν. These equations must be solved simultaneously.

These expressions can be viewed as an expansion in small Δ. It is permissible to truncate the sum over m in R_ν (equation (4.42)) if the gaps, Δ_ν, are small enough, as originally argued by Gor'kov [36]. Traditional GL corresponds to a truncation at $m = 1$ with additional approximations about the field and the spatial variation of the gaps, and extended GL can be achieved by retaining higher order terms.

4.2.2 Uniform Field Free Case

In this section we are interested in finding a better approximation for the mean value of the gaps, so we will consider the case where the magnetic field is zero and the gap does not depend on $\mathbf{r}$. This is the uniform limit of the equations.

In the absence of a magnetic field, the equation for the normal Green function can be solved by performing a Fourier transform. The result is

$$\mathcal{G}_{\nu,\omega_n}(\mathbf{r}, \mathbf{r}') = \frac{1}{(2\pi)^3} \int d\mathbf{k} \, \frac{\hbar e^{i\mathbf{k} \cdot (\mathbf{r} - \mathbf{r}')}}{i\hbar \omega_n - \varepsilon_{\nu,k}}, \tag{4.45}$$

with $\varepsilon_{\nu,k} = \frac{\hbar^2 k^2}{2m_\nu} - \mu_\nu$. Performing each of the real space integrals in equation (4.44) produces a delta function, and these can be used to compute all but one of the k-space integrals, resulting in the simplified expression

$$
\begin{aligned}
P_{\nu,m} &= \frac{(-1)^m}{\beta} \sum_{n=-\infty}^{\infty} \int d\mathbf{k} \, \frac{\Delta_\nu |\Delta_\nu|^{2m}}{((\hbar \omega_n)^2 + \varepsilon_{\nu,k}^2)^{m+1}} \\
&= \frac{(-1)^m}{\beta} N_\nu(0) \sum_{n=-\infty}^{\infty} \int d\varepsilon \, \frac{\Delta_\nu |\Delta_\nu|^{2m}}{((\hbar \omega_n)^2 + \varepsilon^2)^{m+1}},
\end{aligned}
\tag{4.46}
$$

with $N_\nu(0)$ is the density of states in band ν. When $m = 0$ this integral diverges logarithmically, and so must be cut off at the Debye energy, $\hbar\omega_D$. In this case we find

$$P_{\nu,0} = \beta^{-1} N_\nu(0) \sum_{n=-\infty}^{\infty} \int_{-\hbar\omega_D}^{\hbar\omega_D} d\varepsilon \, \frac{\Delta_\nu}{(\hbar\omega_n)^2 + \varepsilon^2}$$
$$\approx N_\nu(0)\Delta_\nu \mathcal{A} - a_\nu \Delta_\nu \ln\left(\frac{1}{1-\tau}\right), \tag{4.47}$$

$$\mathcal{A} = \ln\left(\frac{2\hbar\omega_D e^\Gamma}{\pi k_B T_c}\right), \tag{4.48}$$

$$a_\nu = -N_\nu(0), \tag{4.49}$$

where $\Gamma \approx 0.5772$ is the Euler-Mascheroni constant and $\tau = 1 - T/T_c$ with T_c to be found later. The remaining terms with $m \geq 1$ may be computed directly

$$P_{\nu,m} = \frac{(-1)^m}{\beta} N_\nu(0) \sum_{n=-\infty}^{\infty} \int_{-\infty}^{\infty} d\varepsilon \, \frac{\Delta_\nu |\Delta_\nu|^{2m}}{((\hbar\omega_n)^2 + \varepsilon^2)^{m+1}}$$
$$= -b_{\nu,m} \Delta_\nu |\Delta_\nu|^{2m} \frac{1}{(1-\tau)^{2m}}, \tag{4.50}$$

$$b_{\nu,m} = -N_\nu(0)\frac{(-1)^m (2^{2m+1} - 1)(2m)!\zeta(2m+1)}{(4\pi)^{2m}(m!)^2(k_B T_c)^{2m}}, \tag{4.51}$$

where $\zeta(z)$ is the Riemann zeta function. Putting this back together we find

$$R_\nu = N_\nu(0)\mathcal{A}\Delta_\nu - a_\nu \ln\left(\frac{1}{1-\tau}\right)\Delta_\nu$$
$$- \sum_{m=1}^{\infty} b_{\nu,m} \frac{1}{(1-\tau)^{2m}} |\Delta_\nu|^{2m} \Delta_\nu. \tag{4.52}$$

We then regroup terms to rewrite equation (4.41) in the form

$$0 = \check{L} \cdot \vec{\Delta} + \vec{W}, \tag{4.53}$$

$$W_\nu = a_\nu \ln\left(\frac{1}{1-\tau}\right)\Delta_\nu + \sum_{m=1}^{\infty} b_{\nu,m} \frac{1}{(1-\tau)^{2m}} |\Delta_\nu|^{2m} \Delta_\nu, \tag{4.54}$$

with $\check{L} = \check{g}^{-1} - \check{N}(0)\mathcal{A}$, and $\check{N}(0)$ is a diagonal matrix with elements $N_\nu(0)$ on the diagonal.

4.2.3 Expansion in Small τ

Near the transition temperature, τ is a small parameter, so we will expand equation (4.53) in powers of τ. To truncate this expansion, keeping only terms up to $\mathcal{O}\left(\tau^{(2n+1)/2}\right)$, we first make the scaling

$$\Delta_\nu = \tau^{1/2} \widetilde{\Delta}_\nu. \tag{4.55}$$

After scaling and then dividing through by $\tau^{1/2}$ we find

$$0 = \check{L}.\vec{\widetilde{\Delta}} + \vec{\widetilde{W}}, \tag{4.56}$$

$$\widetilde{W}_\nu = a_\nu \ln\left(\frac{1}{1-\tau}\right)\widetilde{\Delta}_\nu + \sum_{m=1}^{\infty} b_{\nu,m}\frac{\tau^m}{(1-\tau)^{2m}}\left|\widetilde{\Delta}_\nu\right|^{2m}\widetilde{\Delta}_\nu. \tag{4.57}$$

Then the gap is expanded in powers of τ, as is all the other dependence on τ in $\widetilde{W}_\nu$. The $\widetilde{\Delta}_\nu$ and $\widetilde{W}_\nu$ expansions are given by

$$\widetilde{\Delta}_\nu(\tau) = \sum_{n=0}^{\infty} \Delta_\nu^{(n)}\tau^n, \tag{4.58}$$

$$\widetilde{W}_\nu = \sum_{p=1}^{\infty} W_\nu^{(p)}\tau^p. \tag{4.59}$$

We recover a set of equations for the coefficients $\Delta_\nu^{(n)}$ by collecting powers of τ in equation (4.56) and requiring that the equality holds for all τ. The leading order behaviour is a constant. Collecting these constant terms leads to the lowest order equation

$$0 = \check{L}\cdot\vec{\Delta}^{(0)}. \tag{4.60}$$

This has a nontrivial solution if $\det\check{L} = 0$. We recognise that this is just the BCS equation for the critical temperature T_{c}. We therefore satisfy this equation by choosing T_{c} to be the largest solution to this equation.

Now, since $\det\check{L} = 0$, there is at least one eigenvector of $\check{L}$ with a zero eigenvalue. We shall assume that this is nondegenerate, so that there is only one zero eigenvalue. We choose the base eigenvector to have the form

$$\vec{\eta}_1 = [\rho_1, \rho_2, \ldots, \rho_N]^T, \tag{4.61}$$

$$\rho_i = \frac{c_{1,i}}{c_{1,1}}, \tag{4.62}$$

$$c_{ijk\ldots,lmn\ldots} = (-1)^{i+j+k+\ldots+l+m+n+\cdots}M_{ijk\ldots,lmn\ldots}, \tag{4.63}$$

where $c_{ijk\ldots,lmn\ldots}$ is the cofactor of the matrix $\check{L}$, and $M_{ijk\ldots,lmn\ldots}$ is the minor of $\check{L}$, defined as the determinant of the matrix obtained by removing the rows $i, j, k, \ldots$ and columns $l, m, n, \ldots$ from $\check{L}$. Assuming all ρ_i are finite and nonzero, we can then obtain a complete basis with the remaining vectors

$$\vec{\eta}_i = [\rho_1, \rho_2, \ldots, -\rho_i, \ldots, \rho_N]^T. \tag{4.64}$$

The superconducting gaps can be written with this basis as

$$\vec{\Delta}^{(n)} = \sum_j \psi_j^{(n)}\vec{\eta}_j. \tag{4.65}$$

Putting this back into equation (4.60) and using the fact that $\check{L}.\vec{\eta}_1 = 0$ and $\check{L}.\vec{\eta}_j \neq 0$, $j \neq 1$, we find

$$\psi_j^{(0)} = 0, \quad j \neq 1, \tag{4.66}$$

$$\vec{\Delta}^{(0)} = \psi_1^{(0)} \vec{\eta}_1, \tag{4.67}$$

where $\psi_1^{(0)}$ is yet to be determined. The term linear in τ gives the equation

$$0 = \check{L}.\vec{\Delta}^{(1)} + \vec{W}^{(1)}, \tag{4.68}$$

$$W_\nu^{(1)} = a_\nu \Delta_\nu^{(0)} + b_{\nu,1} \Delta_\nu^{(0)} \left| \Delta_\nu^{(0)} \right|^2. \tag{4.69}$$

This mixes $\vec{\Delta}^{(0)}$ with $\vec{\Delta}^{(1)}$, however, as pointed out by Vagov et al. [58], we can remove the $\vec{\Delta}^{(1)}$ dependence using the fact that $\vec{\eta}_1^T.\check{L} = 0$. Projecting this equation on to $\vec{\eta}_1$ and using the solution for $\vec{\Delta}^{(0)}$ we find

$$0 = \sum_\nu a_\nu \eta_{1,\nu}^2 \psi_1^{(0)} + b_{\nu,1} \eta_{1,\nu}^4 \psi_1^{(0)} \left| \psi_1^{(0)} \right|^2 \tag{4.70}$$

$$= a\psi_1^{(0)} + b_1 \psi_1^{(0)} \left| \psi_1^{(0)} \right|^2, \tag{4.71}$$

with $a = \sum_\nu a_\nu \eta_{1,\nu}^2$ and $b_1 = \sum_\nu b_{\nu,1} \eta_{1,\nu}^4$. This has the same form as the one-band uniform GL equation. Kogan and Schmalian [126] pointed out that the gradient term is also the same as the one-band GL equation, and thus there is only one coherence length near T_c, and the order parameters are proportional to each other.

Projecting equation (4.68) onto the other basis vectors, $\vec{\eta}_i$, results in a further set of equations for the higher components, $\psi_j^{(1)}$.

$$0 = \left(\sum_{j \neq 1} \vec{\eta}_i^T.\check{L}.\vec{\eta}_j \psi_j^{(1)} \right)$$

$$+ \sum_\nu a_\nu \eta_{i,\nu} \eta_{1,\nu} \psi_1^{(0)} + b_{\nu,1} \eta_{i,\nu} \eta_{1,\nu}^3 \psi_1^{(0)} \left| \psi_1^{(0)} \right|^2 \tag{4.72}$$

$$= \sum_{j \neq 1} \gamma_{ij} \psi_j^{(1)} + \alpha_i \psi_1^{(0)} + \beta_{i,1} \psi_1^{(0)} \left| \psi_1^{(0)} \right|^2, \tag{4.73}$$

with $\gamma_{ij} = \vec{\eta}_i.\check{L}.\vec{\eta}_j$, $\alpha_i = \sum_\nu a_\nu \eta_{i,\nu} \eta_{1,\nu} = a - 2a_i \rho_i^2$ and $\beta_{i,1} = \sum_\nu b_{\nu,1} \eta_{i,\nu} \eta_{1,\nu}^3 = b - 2b_{i,1}\rho_i^4$. The indices i and j refer to the basis vectors, $\vec{\eta}_j$, not the band indices, ν.

This process can be continued recursively to find the GL approximation to any order. We provide the form for the terms $W_\nu^{(2)}$ and $W_\nu^{(3)}$.

$$W_\nu^{(2)} = a_\nu \Delta_\nu^{(1)} + b_{\nu,1} \left(2\Delta_\nu^{(1)} \left| \Delta_\nu^{(0)} \right|^2 + \Delta_\nu^{(0)2} \Delta_\nu^{(1)*} \right)$$

$$+ \frac{1}{2} a_\nu \Delta_\nu^{(0)} + 2b_{\nu,1} \Delta_\nu^{(0)} \left| \Delta_\nu^{(0)} \right|^2 + b_{\nu,2} \Delta_\nu^{(0)} \left| \Delta_\nu^{(0)} \right|^4, \tag{4.74}$$
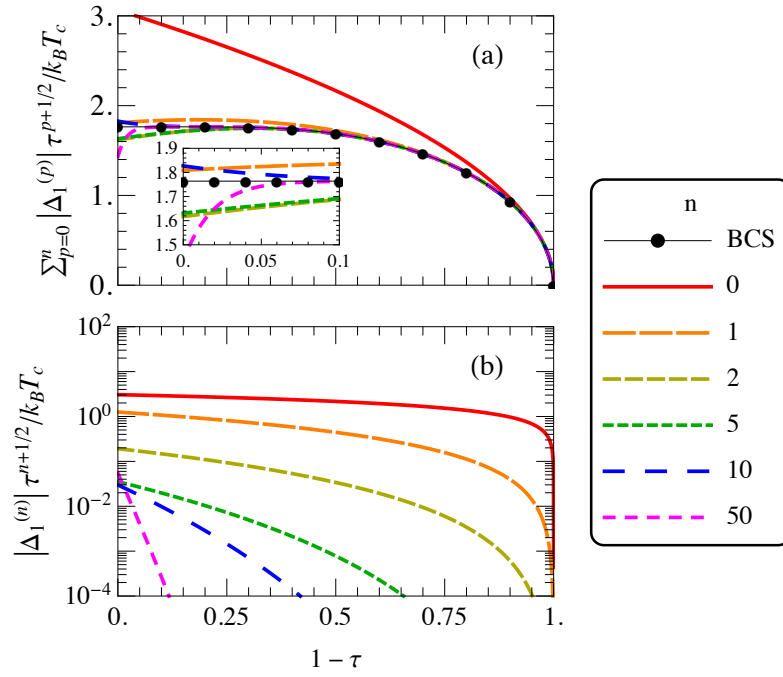
Figure 4.5: (a) The extended GL expansion is compared to a numerical calculation of the full BCS result. The extended GL converges to the true solution on the region $\tau < 1$ and for moderate τ it converges quickly to the BCS solution. Inset: A close up of the region near $\tau = 1$. There are singularities in the BCS function infinitesimally close to $\tau = 1$ which prevent the extended GL from converging at this point. (b) The magnitude of individual terms in the GL expansion are shown on a log plot. The magnitude of the higher terms decays quickly except near the point $\tau = 1$ where it remains finite. This shows that the expansion is converging on the region $\tau < 1$.

$$
\begin{aligned}
W_\nu^{(3)} = {} & a_\nu \Delta_\nu^{(2)} + b_{\nu,1} \left(2\Delta_\nu^{(2)} \left| \Delta_\nu^{(0)} \right|^2 + \Delta_\nu^{(0)2} \Delta_\nu^{(2)*} \right) \\
& + b_{\nu,1} \left(2\Delta_\nu^{(0)} \left| \Delta_\nu^{(1)} \right|^2 + \Delta_\nu^{(1)2} \Delta_\nu^{(0)*} \right) \\
& + \frac{1}{2} a_\nu \Delta_\nu^{(1)} + 2 b_{\nu,1} \left(2\Delta_\nu^{(1)} \left| \Delta_\nu^{(0)} \right|^2 + \Delta_\nu^{(0)2} \Delta_\nu^{(1)*} \right) \\
& + b_{\nu,2} \left(3\Delta_\nu^{(1)} \left| \Delta_\nu^{(0)} \right|^4 + 2 \left| \Delta_\nu^{(0)} \right|^2 \Delta_\nu^{(0)2} \Delta_\nu^{(1)*} \right) \\
& + \frac{1}{3} a_\nu \Delta_\nu^{(0)} + 3 b_{\nu,1} \Delta_\nu^{(0)} \left| \Delta_\nu^{(0)} \right|^2 + 4 b_{\nu,2} \Delta_\nu^{(0)} \left| \Delta_\nu^{(0)} \right|^4 \\
& + b_{\nu,3} \Delta_\nu^{(0)} \left| \Delta_\nu^{(0)} \right|^6 .
\end{aligned}
\tag{4.75}
$$

All higher order terms can similarly be produced from the full definition of $\widetilde{W}_\nu$.
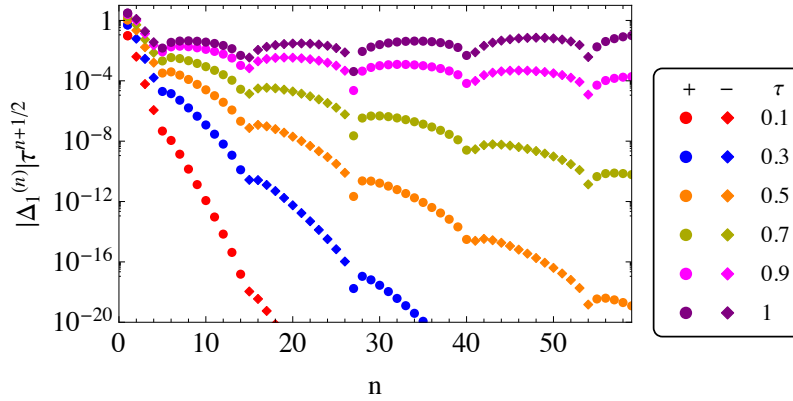
Figure 4.6: This plot shows the magnitude of each term in the one-band series as a function of n for a range of temperatures. The circles (diamonds) indicate that the sign of the term is positive (negative). As $\tau \to 1$, the convergence rate slows down and at $\tau = 1$ the terms no longer decay.

4.2.4 One-Band Ginzburg-Landau Theory

Applying this procedure to a one-band superconductor is fairly straight forward. The matrix $\check{L}$ becomes a number, and the equation for T_c becomes trivial to solve. The basis vector $\eta_1 = 1$ so that $\Delta^{(n)} = \psi_1^{(n)}$ in equation (4.65).

This procedure has been performed for the one-band case to high order, with the results shown in figure 4.5. The BCS solution is given by the bold black dots in the top plot. The thin red line that overshoots this is the conventional $\tau^{1/2}$ GL theory, while a selection of plots with higher order corrections up to $\tau^{(2n+1)/2}$ with $n = 50$ are also shown. The first correction, $\tau^{3/2}$ is seen as the dashed line just above the BCS solution [57], while higher order corrections are almost indistinguishable except near $\tau = 1$. Including a larger number of corrections increases the range of convergence, and it is presumed that the infinite sum will converge for all $\tau < 1$. However, for any large finite sum, the deviation near $\tau = 1$ is expected to remain large.

On the bottom plot of figure 4.5 we show the magnitude of each term in the sum. The error of any finite sum is approximately given by the magnitude of the next term in the sum, and so this plot can be viewed as an estimation of the error in any given finite sum. The magnitude of each term decreases in general except near $\tau = 1$, where, after the first few terms, it remains approximately constant.

For the one-band case, an exact form for each term in the expansion can be computed, though the number of terms needed increases rapidly. We show here the

$\Delta_1^{(0)}/k_\mathrm{B}T_\mathrm{c}$	3.06326
$\Delta_1^{(1)}/k_\mathrm{B}T_\mathrm{c}$	-1.25438
$\Delta_1^{(2)}/k_\mathrm{B}T_\mathrm{c}$	-0.191748
$\Delta_1^{(3)}/k_\mathrm{B}T_\mathrm{c}$	-0.0360503
$\Delta_1^{(4)}/k_\mathrm{B}T_\mathrm{c}$	0.014773
$\Delta_1^{(5)}/k_\mathrm{B}T_\mathrm{c}$	0.0353042
$\Delta_1^{(6)}/k_\mathrm{B}T_\mathrm{c}$	0.0431866
$\Delta_1^{(7)}/k_\mathrm{B}T_\mathrm{c}$	0.0444931
$\Delta_1^{(8)}/k_\mathrm{B}T_\mathrm{c}$	0.0418668
$\Delta_1^{(9)}/k_\mathrm{B}T_\mathrm{c}$	0.0366943

Table 4.1: Numeric values for the first ten terms in the one-band extended GL expansion.

exact result for the first three terms in the expansion.

$$\Delta_1^{(0)} = k_\mathrm{B}T_\mathrm{c}\sqrt{\frac{8\pi^2}{7\zeta(3)}}, \tag{4.76}$$

$$\Delta_1^{(1)} = \Delta_1^{(0)}\left(-\frac{3}{4} + \frac{93\zeta(5)}{196\zeta(3)^2}\right), \tag{4.77}$$

$$\Delta_1^{(2)} = \Delta_1^{(0)}\left(-\frac{11}{96} - \frac{93\zeta(5)}{784\zeta(3)^2} + \frac{8649\zeta(5)^2}{10976\zeta(3)^4} - \frac{635\zeta(7)}{1372\zeta(3)^3}\right). \tag{4.78}$$

The higher terms in the expansion quickly increase in complexity. We also show the numerical result for the first 10 terms scaled to $k_\mathrm{B}T_\mathrm{c}$ in table 4.1. During calculation these were retained to very high precision, since each higher term is dependent on the previous, causing the precision of the higher terms to degrade.

In figure 4.6 the magnitude of the terms $\Delta_1^{(n)}\tau^{(2n+1)/2}$ are shown as a function of n for various values of τ. This shows that as τ increases, the convergence decreases considerably, and near τ, the terms no longer decay. There is also a very noticeable oscillation in the sign of the terms, with the sign changing after $10-14$ terms. The sign change is indicated in the plot by the switch from circles to diamonds. For large n the terms seem to be bounded from above by an approximately linear envelope.

4.2.5 Two-Band Ginzburg-Landau Theory

In two-band GL, things progress in much the same way. However, there is now a larger range of possibilities due to three parameters in the interband coupling matrix,
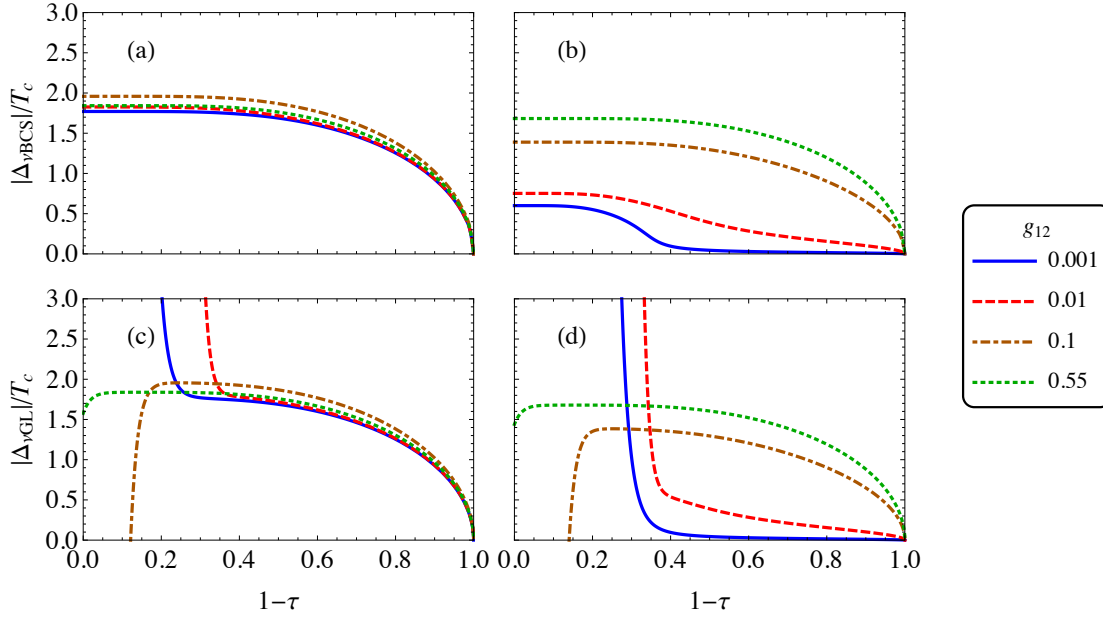
Figure 4.7: Numerical calculations of the BCS gap is compared to the high expansion in the extended GL theory. We use the parameters $g_{11} = 0.6$, $g_{22} = 0.5$, $N_1(0) = N_2(0) = 0.3$, $\hbar\omega_D = 0.09$. a) BCS solution band 1. b) BCS Solution band 2. c) GL solution band 1. d) GL solution band 2. The GL plots are calculated to order $\tau^{n+1/2}$ where $n = 50$.

$g_{\nu\nu'}$, especially the role of the interband interaction, g_{12}.

We know from BCS theory that in the limit that the interband coupling goes to zero, the two gaps are independent and each has their own critical temperatures, which we label T_{1c} and T_{2c} respectively. When the interband coupling is small but nonzero, there is still a large change in the behaviour of the smaller gap near the temperature T_{2c}. However the critical temperature of the combined system is an enhancement of the dominant band's critical temperature.

The exact lowest order solution can easily be calculated, with the result

$$\Delta_1^{(0)} = k_B T_c \frac{\sqrt{L_{22}^2 N_1(0) + L_{12}^2 N_2(0)}}{\sqrt{L_{22}^2 N_1(0) + \frac{L_{12}^4}{L_{22}^2} N_2(0)}} \sqrt{\frac{8\pi^2}{7\zeta(3)}}, \tag{4.79a}$$

$$\Delta_2^{(0)} = k_B T_c \frac{L_{12} \sqrt{L_{22}^2 N_1(0) + L_{12}^2 N_2(0)}}{L_{22} \sqrt{L_{22}^2 N_1(0) + \frac{L_{12}^4}{L_{22}^2} N_2(0)}} \sqrt{\frac{8\pi^2}{7\zeta(3)}}. \tag{4.79b}$$

The higher order terms become increasingly complicated, however the results for specific parameters are calculated numerically to high order.

In figure 4.7 we show plots of the BCS solution for a range of values for the interband coupling, g_{12}. In a) the first gap is plotted, and it is seen that the

interband coupling only has a weak effect on the behaviour of this band, while in b), the second gap shows a drastic change as g_{12} increases, especially near T_{2c}. With the increase of the coupling strength, the large up-swell of the second band near this critical temperature gets washed out, so that at large coupling the plot looks reminiscent of a one-band BCS plot.

Plots c) and d) depict the order parameters of band 1 and 2 respectively as calculated using the extended GL formalism derived earlier. For $1 - \tau \gtrsim 0.3$ the behaviour shown in the GL plots is similar to that of the BCS plots above. However, for $1 - \tau \lesssim 0.3$ the behaviour of the GL plots is drastically different from the BCS plots, with the difference appearing sooner for smaller g_{12}. The point where the solutions begin to disagree is very close to the location of T_{2c}, which in the small coupling limit is $T_{2c} \approx 0.33T_c$. While this finite summation approach does not prove that the series is divergent, it is clear that the sum has not converged in this range for the large number of terms computed. We expect that in general the sum will converge for all $T \gtrsim T_{2c}$, but converge very slowly or diverge for $T \lesssim T_{2c}$. Komendova et al. [119] argue that there is a possibility of hidden criticality near T_{2c} which becomes critical in the limit that the coupling goes to zero. This feature is likely to be associated with the anomalous behaviour of the GL gaps near this point, and is expected to prevent the series from converging below this point.

Surprisingly, while the BCS solution for the first band showed only a weak perturbation with the interband coupling, the nonconvergent behaviour seen in the GL solution of the smaller band also affects the dominant band. This occurs for any small nonzero interband coupling, even though the solution converges for all τ if the interband coupling is zero.

In figure 4.8 the first two columns compare the BCS solution to the extended GL expansion for band 1 and band 2 respectively as a function of $1 - \tau$ for various g_{12}. The second two columns show the magnitude of the individual terms for the two bands. We can see that as the number of terms included in the expansion is increased, the GL solution departs from the BCS solution, shown as dots, in the region $T \lesssim T_{2c}$, and increasing the number of terms increases this difference. Therefore, with this number of terms, the expansion is not converging to the true solution in this range.

As g_{12} increases the location of the nonconvergent point seems to move towards $T = 0$. However we know that T_{2c} is a constant. A possible reason for this behaviour of the pivot point is that as g_{12} increases, T_{2c} does indeed remain constant, but T_c increases, so that T_{2c}/T_c should move towards 0 as g_{12} increases. It is this increase in T_c that makes the nonconvergent point move towards zero as g_{12} increases.
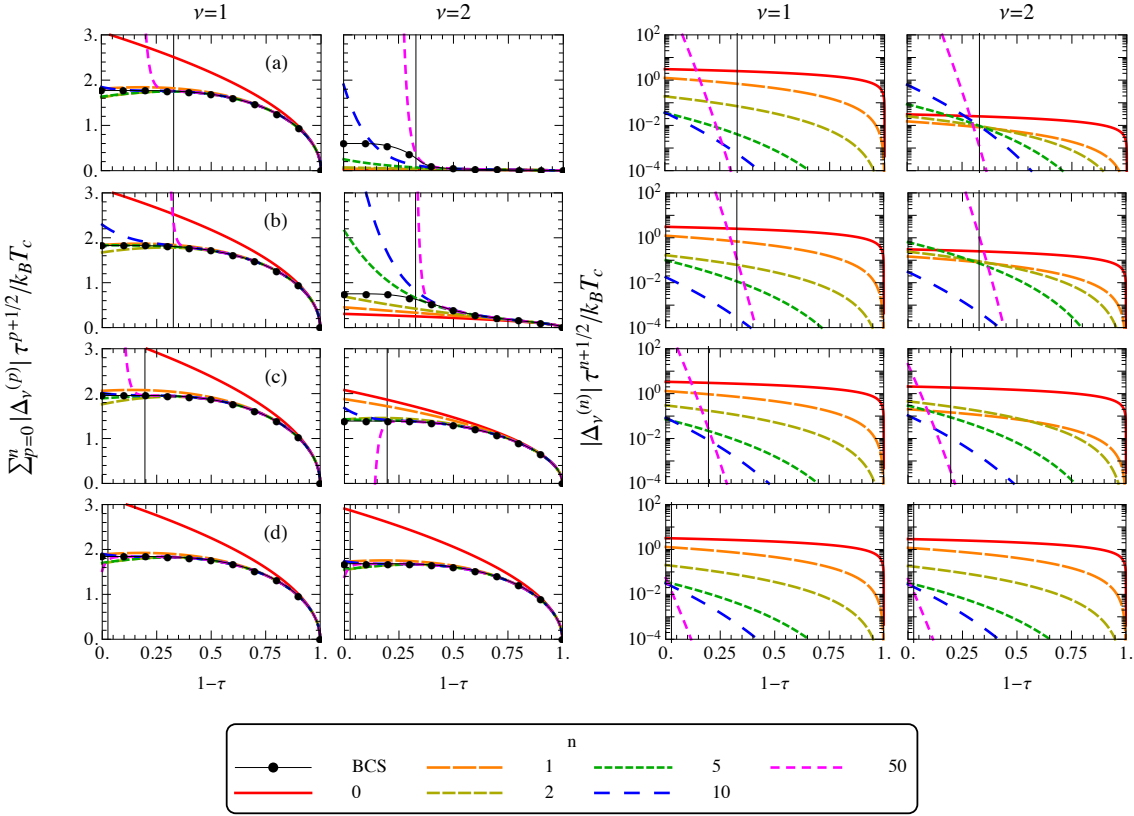
Figure 4.8: The extended GL expansion is compared to a numerical calculation of the full BCS result. In all plots we use the parameters $g_{11} = 0.6$, $g_{22} = 0.5$, $N_1(0) = N_2(0) = 0.3$, $\hbar\omega_D = 0.09$. a) $g_{12} = 0.001$, b) $g_{12} = 0.01$, c) $g_{12} = 0.1$, d) $g_{12} = 0.55$. Columns one and two show the comparison of the GL expansion to the BCS theory for bands one and two respectively. Columns three and four show the magnitude of individual terms in the expansion on a log plot for bands one and two respectively. In all plots the vertical black lines are located at what would be the critical point of the second band in the uncoupled limit, T_{2c}/T_c. We see that for $1 - \tau \gtrsim T_{2c}/T_c$ the trend is for additional terms to decrease in magnitude, and the series seem to be converging, while for $1 - \tau \lesssim T_{2c}/T_c$, the terms tend to grow and the series seem to be diverging. This is confirmed by looking at the individual terms in the log plot.

The plot of the magnitude of the terms in the expansion (figure 4.9) shows similar behaviour to the one-band plot (figure 4.6) for small τ. However the decay in the terms ceases at a much higher temperature (about τ 0.6), confirming the previous analysis.

4.2.6 Application to Real Two-band Materials

In figure 4.10 we present calculations for a range of real materials, $FeSe_{0.94}$ [106], OsB_2 [104], $LiFeAs$ [105], and MgB_2 [146]. The parameters used are representative of
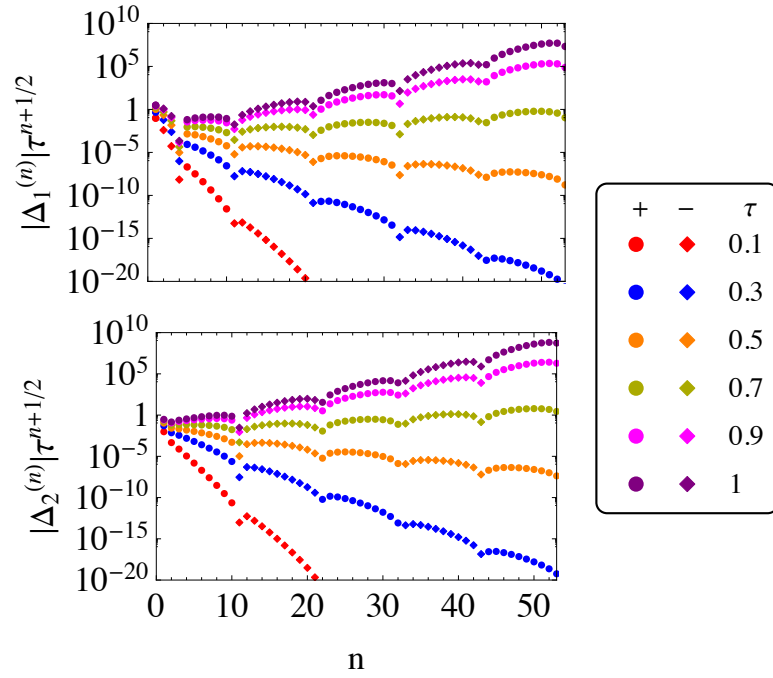
Figure 4.9: This plot shows the magnitude of each term in the two-band series as a function of n for a range of temperatures. The circles (diamonds) indicate that the sign of the term is positive (negative).
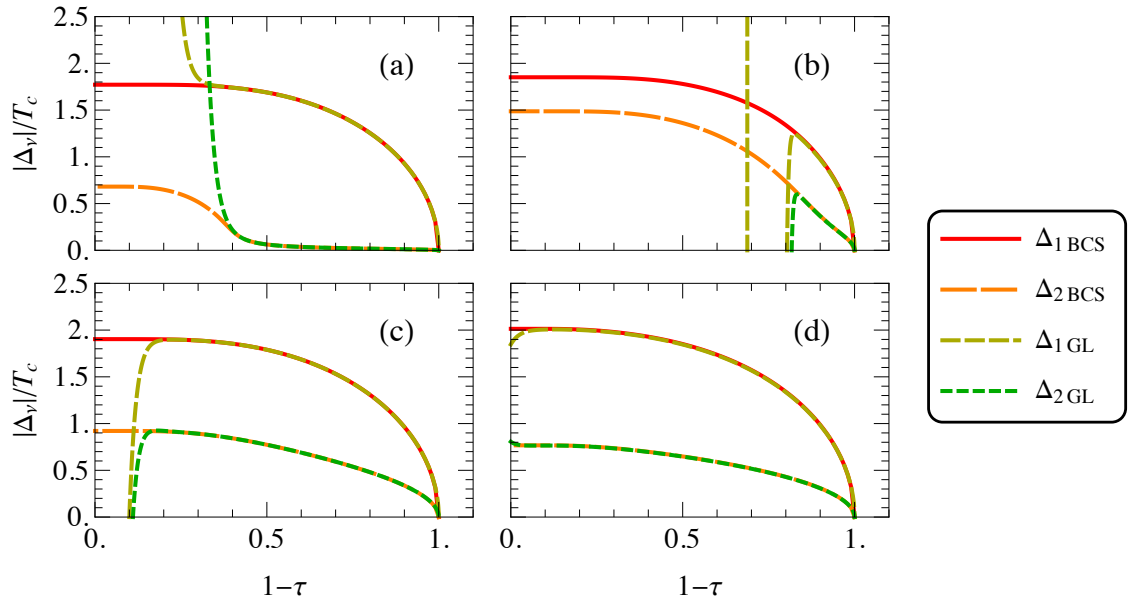

Figure 4.10: The extended GL solutions with parameters corresponding to real materials are compared to the full multiband BCS solutions. The materials are a) $FeSe_{0.94}$, b) OsB_2, c) LiFeAs, d) MgB_2.

the behaviour of the materials, though the exact choice of parameters is not unique. For each set of parameters we plot the BCS and extended GL gaps, with the terms in the GL calculation retained to order $\tau^{(2n+1)/2}$ with $n = 50$.

In a) the parameters were chosen in [106] to match data from a μSR experiment of FeSe$_{0.94}$. These are $g_{11} = 0.241$, $g_{22} = 0.195$, $g_{12} = 0.0005$, $N_2(0)/N_1(0) = 1$. We choose to set $N_1(0) = 1$, but note that in reality this should be chosen such that T_c matches the experimental result. However in the weak coupling limit the resulting scaled plot is independent of the critical temperature, so we are free to choose an overall scale for the interaction strength.

This material is dominated by band 1, which is largely unperturbed. The interband coupling is weak, and therefore we see that the extended GL curve performs well until the second band becomes important (at about $0.4T_c$). However, below this point, the extended GL fails to match with the BCS result.

In b) the parameters are chosen to be representative of OsB$_2$. The parameters used are $g_{11} = 0.387$, $g_{22} = 0.291$, $g_{12} = 0.0084$, $N_2(0)/N_1(0) = 1.22$, $N_1(0) = 1$. In this case the critical temperature of the two uncoupled bands are very close, and since the interband coupling is rather weak, the extended GL theory is only valid in the range $\tau \lesssim 0.2$. This is still a large improvement on the first order result, which only matches over a very limited region.

Parameters for LiFeAs are used for plot c). Although the coupling strengths in this case are very close and the interband coupling is quite small, the difference in the density of states causes the critical temperatures of the uncoupled bands to be separated in temperature, and so the extended GL solution performs well here in the range $\tau \lesssim 0.8$. The parameters used are $g_{11} = 0.63$, $g_{22} = 0.64$, $g_{12} = 0.061$, $N_2(0)/N_1(0) = 0.722$.

d) MgB$_2$ is dominated by band 1, with the interband coupling of the same order as the intraband coupling in band 2. The parameters used here are $g_{11} = 1.02$, $g_{22} = 0.37$, $g_{12} = 0.18$, $N_2(0)/N_1(0) = 1.33$. The extended GL for this system performs extremely well until very close to $T = 0$.

We see that in the two-band case, where the two gaps are close to degenerate and the interband coupling is very weak, the GL approximation is only valid in a very small temperature region near T_c, and the theory should be applied with care. However, for the case where one band is very dominant, or where the interband coupling is very large, the GL theory performs very well, and converges quickly to the BCS result over a fairly large temperature range.

		FeSe$_{0.94}$	OsB$_2$	LiFeAs	MgB$_2$
$\Delta_{10}/k_B T_c$	This Work	1.77	1.85	1.90	2.01
	Ref	1.77 [106]	1.90 [104]	1.89 [105]	2.25 [146]
$\Delta_{20}/k_B T_c$	This Work	0.68	1.48	0.92	0.77
	Ref	0.68 [106]	1.25 [104]	1.11 [105]	0.55 [146]

Table 4.2: This table displays the BCS ratio $\Delta_0/k_B T_c$ for the gaps in the two-band materials considered here. For a one-band BCS material, this should give the universal result 1.76. The values obtained from the fitted parameters agree reasonably with the experimental results.

Table 4.2 compares the two-band BCS ratio to experimental values. The values compare favourably with experimental results, although there is some discrepancy. However the experimental values obtained with different experiments also vary considerably.

4.2.7 Summary

In this section we have reconstructed the relationship of the BCS theory with the GL theory with the limitations developed by Gor'kov in his groundbreaking work. The theory has been restricted to the case of a uniform system, but has been extended to allow multiple bands and large order in τ. This extends the work of ref [58] where the authors calculated a similar expansion keeping terms of order $\tau^{3/2}$ in the presence of a magnetic field.

We have shown that in a one-band superconductor the $\tau^{3/2}$ correction improves the magnitude of order parameter closer to the BCS value. Higher order corrections for $n \geq 1$ in $\tau^{(2n+1)/2}$ improve the agreement with the BCS result except at $T = 0$, where the series for the gap appears to be nonconvergent.

In the two-band situation, the interband coupling plays a pivotal role in enhancing the smaller order parameter above the T_{2c} value in the BCS model. As the interband coupling increases, the point of inflection around T_{c2} heals gradually. At large interband coupling both gaps look similar to a one-band solution. The critical temperature of the system evolves smoothly out of the largest critical temperature, T_{1c}, and is enhanced by the interband coupling.

In the GL model there are significant differences for both the gaps below $T \lesssim T_{2c}$. The large deviation persists for weaker interband couplings despite including larger $\tau^{(2n+1)/2}$ corrections. This issue is significant when T_{2c} is close to the critical temperature T_c. In this case the range of validity of the GL solution can be extremely

small. The GL solution to the gaps below T_{2c} is unreliable, and therefore care must be taken when applying the GL model to multiband superconductors.

When the interband coupling is larger or when one of the gaps is very dominant, the GL solution performs much better and including higher order terms can make the solution close to the BCS value over a large temperature range. Similar to the one-band case, the point $T = 0$ is nonconvergent in the multiband solution regardless of interband coupling.

We have applied this extended GL theory to a range of two-band superconductors. We find that in some cases the extended theory performs extremely well over almost the entire temperature range, while for other materials the location of the second critical temperature limits the applicability of GL theory at lower temperatures.

In summary we have clearly demonstrated the importance of $\tau^{(2n+1)/2}$ expansion for large n for multiband GL superconductors. This point emphasises the weaker validity of the GL theory for lower temperatures for some materials, and especially for applications with small interband coupling. We are of the opinion that any use or misuse of GL theory has to be carefully examined considering its domain of applicability.

CHAPTER FIVE

Multiband Superconductors in a Magnetic Field: Vortex States

Having looked at the extended form of multiband GL theory, we now return to the traditional multiband GL theory description and look for nonuniform solutions.

We begin by investigating vortex states. One example of a vortex solution in the one-band case was shown earlier in section 2.1.3. We look at these for the multiband theory with a range of numeric methods in both one- and two-dimensions. After formulating the two-dimensional method, we also examine some skyrmion solutions. These are magnetic states which appear above a TRSB background.

5.1 Vortex States

As in the one-band vortices, the flux in a multiband vortex is quantised, with the quantum of flux $\varphi_0 = \frac{hc}{2e}$. This is a direct result of the requirement that the order parameter be single valued, so that the phase around a vortex can only change by an integer multiple of 2π.

5.1.1 Single Vortex Equations

A single vortex in a superconductor has cylindrical symmetry. We can look for solutions of this form by choosing an ansatz with this symmetry. We choose an ansatz where the magnitude of the order parameter only depends on the distance from the centre of the vortex. The order parameter picks up a phase of $2n\pi$ when following a contour around the vortex, where n is the order of the vortex. With

these assumptions, we can write an ansatz in the form

$$\Psi_\nu(\mathbf{r}) = f_\nu(\rho) \exp\left(i(n\theta + \phi_{\nu 0})\right), \tag{5.1a}$$

$$\mathbf{A}(\mathbf{r}) = \frac{n\varphi_0}{2\pi\rho} A(\rho) \hat{\mathbf{e}}_\theta, \tag{5.1b}$$

where f is the magnitude of the order parameters, n is an integer which determines the order of the vortex, ρ is the radial coordinate and θ is the polar angle around the vortex, $\phi_{\nu 0}$ is the relative phases of the order parameters in the bulk, $\hat{\mathbf{e}}_\theta$ is a unit vector in the angular direction, and $\varphi_0 = \frac{hc}{2e}$ is the flux quantum . The relative phase of the order parameters are assumed to be locked to their equilibrium values. This is a good approximation unless the superconductor is in the TRSB state. A more general form for a single vortex in the TRSB state would allow $\phi_{\nu 0}$ to vary away from the equilibrium value for small ρ. However we will see later that there are other collective states that appear in TRSB superconductors, so we will not consider that case here.

Putting the ansatz into the GL equations, we find the one-dimensional equations

$$a_\nu f_\nu(\rho) + b_\nu f_\nu(\rho)^3 + \sum_{\nu' \neq \nu} \gamma_{\nu\nu'} f_{\nu'}(\rho) \cos(\phi_{\nu 0} - \phi_{\nu' 0})$$
$$+ \frac{\hbar^2}{2m_\nu^*} \left(\frac{d^2 f_\nu}{d\rho^2} + \frac{1}{\rho} \frac{d f_\nu}{d\rho} + \frac{n^2(A(\rho)+1)^2}{\rho^2} f_\nu \right) = 0, \tag{5.2a}$$

$$\sum_{\nu' \neq \nu} \gamma_{\nu\nu'} f_{\nu'}(\rho) \sin(\phi_{\nu 0} - \phi_{\nu' 0}) = 0, \tag{5.2b}$$

$$\frac{d^2 A}{d\rho^2} - \frac{1}{\rho} \frac{dA}{d\rho} + \sum_\nu \frac{4\pi e^{*2}}{m_\nu^* c^2} f_\nu^2 (1 + A(\rho)) = 0, \tag{5.2c}$$

along with the boundary conditions

$$A(0) = 0, \qquad\qquad A(\infty) = -1, \tag{5.3a}$$

$$f_\nu(0) = 0, \qquad\qquad f_\nu(\infty) = f_{\nu 0}. \tag{5.3b}$$

Note that equation (5.2b) can only have a nontrivial solution for all ρ if $\sin(\phi_{\nu 0} - \phi_{\nu' 0}) = 0$ for all ν, ν', i.e. all the phase differences are locked at either 0 or π, so the material is in the standard superconducting state.

The supercurrent circulating around the vortex for the band ν can be found by returning to the full form for the current equation. The supercurrent associated with each band is found to be

$$\mathbf{j}_\nu(\mathbf{r}) = \frac{n\varphi_0}{2\pi\rho} (A(\rho) + 1) f_\nu^2(\rho) \hat{\mathbf{e}}_\theta. \tag{5.4}$$

We will first apply a finite difference method and a variational method to the single vortex problem. We will then extend the variational method to a two vortex problem. Finally we will use time-dependent Ginzburg-Landau theory (TDGL) with a forward-time central-space (FTCS) discretisation method to find the configuration of many vortices, as well as other magnetic states.

5.1.2 Finite Difference Method

The finite difference method is one of the simplest methods to implement and is applied to equation (5.2). We use central difference and quasi-linearisation, and iterate the solution until convergence is reached.

The finite difference method in one-dimension is used to solve a general second-order differential equation of the form [147, 148]

$$\left(\frac{\mathrm{d}^2}{\mathrm{d}x^2} + p(x)\frac{\mathrm{d}}{\mathrm{d}x} + q(x) \right) u(x) = r(x), \tag{5.5}$$

with the Dirichlet boundary conditions

$$u(x_L) = u_L, \tag{5.6a}$$

$$u(x_R) = u_R, \tag{5.6b}$$

where the subscripts L and R denote the left and right boundaries respectively. A uniform mesh of $N + 2$ points is chosen. The mesh points are at the points

$$x_j = x_L + jh_x, \qquad j = 0, 1, \ldots, N+1, \qquad h_x = \frac{x_R - x_L}{N+1}. \tag{5.7}$$

Defining the coefficients at the mesh points in the obvious way

$$p_j = p(x_j), \qquad q_j = q(x_j), \qquad r_j = r(x_j), \tag{5.8}$$

then converting the derivatives to central finite differences, the differential equation can be written as a matrix equation

$$\check{K} \cdot \vec{u} = \vec{f}, \tag{5.9}$$

where we have borrowed the notation that $\check{A}$ represents a matrix and $\vec{A}$ represents a vector. The $\check{K}$ matrix is tridiagonal and is created by approximating the derivatives as central differences. It is given in matrix form as

$$\check{K} = \frac{1}{h_x{}^2} \begin{pmatrix} -2 + h_x{}^2 q_1 & 1 + \frac{1}{2}h_x p_1 & 0 & \cdots & 0 \\ 1 - \frac{1}{2}h_x p_2 & -2 + h_x{}^2 q_2 & 1 + \frac{1}{2}h_x p_2 & \cdots & 0 \\ 0 & 1 - \frac{1}{2}h_x p_3 & -2 + h_x{}^2 q_3 & \cdots & 0 \\ \vdots & \vdots & \vdots & \ddots & \vdots \\ 0 & 0 & 0 & \cdots & -2 + h_x{}^2 q_N \end{pmatrix}. \tag{5.10}$$

The $\vec{f}$ vector is a combination of the homogeneous part of the original equations, plus terms which come from applying the Robin boundary conditions. It is explicitly given as

$$\vec{f} = \begin{pmatrix} r_1 - u_0 \frac{1}{h_x^2}(1 - \frac{1}{2}h_x p_1) \\ r_2 \\ r_3 \\ \vdots \\ r_N - u_{N+1} \frac{1}{h_x^2}(1 + \frac{1}{2}h_x p_N) \end{pmatrix}. \tag{5.11}$$

The vector $\vec{u}$ is a vector of the unknown node values

$$\vec{u} = \begin{pmatrix} u_1 \\ u_2 \\ u_3 \\ \vdots \\ u_N \end{pmatrix}. \tag{5.12}$$

The advantage of this approach is that the matrix equation can be solved very quickly by using the fact that the matrix is tridiagonal. However, this approach can only directly solve linear equations.

We use quasi-linearisation to convert the equation to a linear equation that is solved iteratively [148]. To perform this the nonlinear terms, f_ν^3, are Taylor expanded to first order about an initial solution, $f_\nu^{(0)}$. The resulting equation is linear and can be solved for a new function $f_\nu^{(1)}$. This can then be used as a new initial solution, and this iteration procedure can be repeated until convergence is reached, and at that point we have an approximate solution to the original nonlinear equation. Since we are only interested in the stationary states, we combine this iteration procedure with the time evolution, so that only one iteration is computed at each time step. In the long time limit the calculated solution will approximately solve the full nonlinear equation. The coefficients required for updating the order parameters after quasi-linearisation are

$$p_j = \frac{1}{\rho_j}, \tag{5.13a}$$

$$q_j = -\frac{2m_\nu}{\hbar^2}\left(-a + 3bf_{\nu j}^{(i)2}\right) - \frac{n^2\left(A_j^{(i)} + 1\right)^2}{\rho_j^2}, \tag{5.13b}$$

$$r_j = -\frac{2m_\nu}{\hbar^2}\left(\sum_{\nu'} \gamma_{\nu\nu'} f_{\nu' j}^{(i)} \cos(\phi_{\nu 0} - \phi_{\nu' 0}) + 2bf_{\nu j}^{(i)3}\right), \tag{5.13c}$$

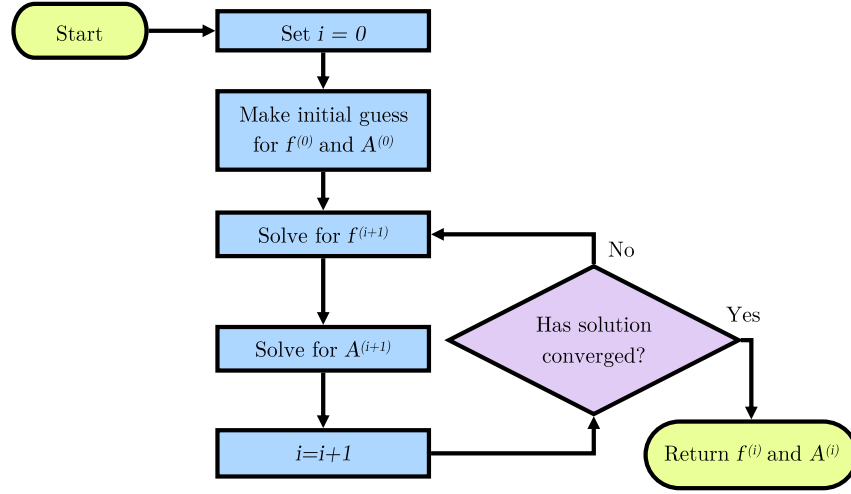where i here is an iteration index. The coefficients for the vector potential are easier

Figure 5.1: Flowchart for iterative solution of the finite difference equations.

to find and are immediately written as

$$p_j = -\frac{1}{\rho_j}, \tag{5.14a}$$

$$q_j = \sum_\nu \frac{4\pi e^{*2}}{m_\nu^* c^2} f_\nu^{(i+1)2}, \tag{5.14b}$$

$$r_j = -\sum_\nu \frac{4\pi e^{*2}}{m_\nu^* c^2} f_\nu^{(i+1)2}. \tag{5.14c}$$

The full method to solve this equation is therefore to choose an initial guess for the order parameters and the vector potential, then use this to find a new solution for the order parameters, then find a new solution for the vector potential, and repeat until the solution converges (figure 5.1).

A typical two-band solution is shown in figure 5.2. In general, although the coherence length in the bulk is the same for all bands, near the core each band can have a different effective coherence length. If these effective coherence lengths are very different, then the vortex will have a composite core, and one of the bands could temporarily saturate near its noninteracting uniform value. The return to the full uniform solution would then occur on the length scale of the larger coherence length.

Additionally, the effective penetration depth of the magnetic field near the centre of the vortex can be much lower than the penetration depth in the bulk due to the
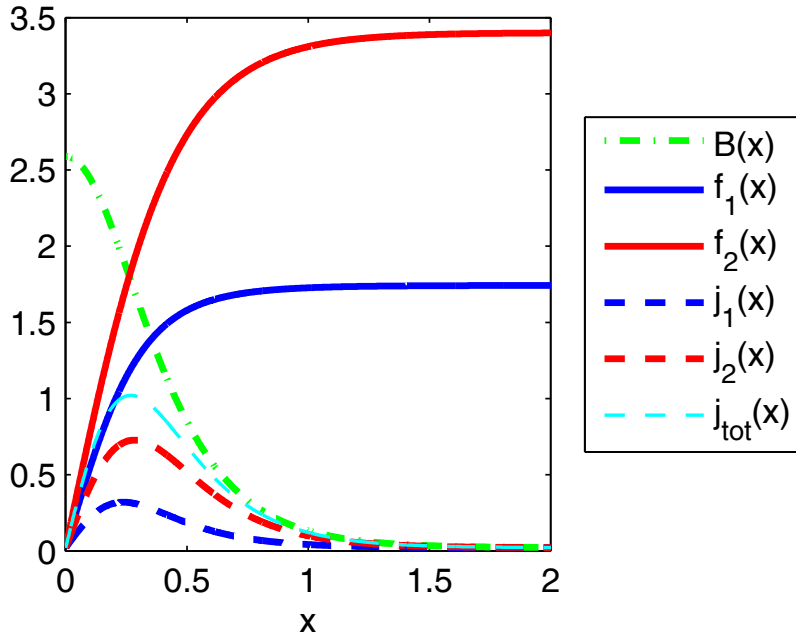
Figure 5.2: A vortex solution to the two-band GL equations computed using the finite difference method. The magnetic field, B, peaks at the centre of the vortex, and the exponential decay far from the core is visible. The smaller order parameter ,f_1, approaches the bulk value faster than the dominant order parameter, f_2. The supercurrent, j_{tot}, peaks quite close to the centre of the vortex.

suppression of the order parameters. As ρ increases, the effective penetration depth, asymptotically approaching the calculated value and the asymptotic solution.

Next we will use a variational method to find a single vortex, giant vortex $(n = 2)$ and double vortex solution.

5.1.3 Variational Method

One Vortex

A variational approach to the vortex problem is to give an ansatz to the form of the order parameters and vector potential as a function of distance, and then choose the parameters such that the energy of the vortex is minimised. If the ansatz captures the main physical aspects of the problem, then the form of the final function should approximate the true solution, and the energy of the vortex will give an upper bound to the true energy of the vortex state.

The appropriate ansatz to choose needs to return to the bulk superconducting solution far from the vortex core, and the order parameter (vector potential) must return to this value over a length scale of the coherence length (penetration depth)

respectively. These requirements are met by choosing an ansatz of the form [112, 134]

$$f_\nu(\rho) = f_{\nu 0} + \exp\left(-\frac{\sqrt{2}\rho}{\xi}\right) \sum_{m=0}^{m_{\max}} \frac{f_\nu^{(m)} \rho^m}{m!}, \tag{5.15a}$$

$$A(\rho) = -1 + \exp\left(-\frac{\rho}{\lambda}\right) \sum_{m=0}^{m_{\max}} \frac{A^{(m)} \rho^m}{m!}, \tag{5.15b}$$

where $f_\nu^{(m)}$ and $A^{(m)}$ are the variational parameters to be determined, and $m_{\max}$ is a cut-off to be chosen. Including more terms will improve the approximation at the cost of computational time.

The boundary conditions in the limit $\rho \to \infty$ are automatically satisfied. To satisfy the boundary conditions as $\rho \to 0$, we require

$$f_\nu^{(0)} = -f_{\nu 0}, \qquad\qquad A^{(0)} = 1, \qquad\qquad A^{(1)} = 1. \tag{5.16}$$

Additionally, for a giant vortex solution, we require $f_\nu^{(0)} = -\sqrt{2}f_{\nu 0}/\xi$ which ensures that $f_\nu = \mathcal{O}(\rho^2)$ as $\rho \to 0$.

With the variational ansatz created, this is then put back into the free energy of the system, so that the free energy is a quartic in the variational parameters. An approximate solution is one that minimises the free energy. This minimum is approached using Newton's method, which locally treats the potential as a quadratic in the variational parameters. This approach finds an accurate approximation to the ground state after relatively few steps, but is rather costly per step, which limits the number of free parameters in the ansatz.

An example of a single vortex for a two-band model is shown in figure 5.3, and an example of a giant vortex is shown in figure 5.4. These solutions capture the main features of the two-band vortex.

Two Interacting Vortices

Having found the single vortex solution, Jacobs and Rebbi [134] show that a conformal transformation can be used to map this onto an approximate two vortex solution. Choosing an ansatz with additional variational parameters, we can again find values which minimise the free energy of the two vortex solution.

This method has the advantage that the distance between the two vortices can be chosen by hand. The energy profile of the solution can then be plotted as a function of the separation, and from this we can find the vortex-vortex interaction force.
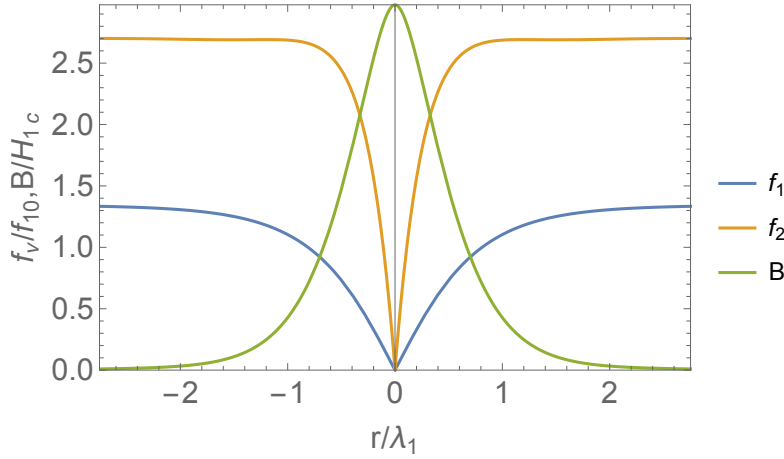
Figure 5.3: Single vortex solution ($n = 1$) computed using variational method. The parameters have been scaled to parameters of the uncoupled first band (setting $\gamma_{12} = 0$): the penetration depth, λ_1, the bulk value of the order parameter, f_{10}, and the thermodynamic critical field, H_{1c}.
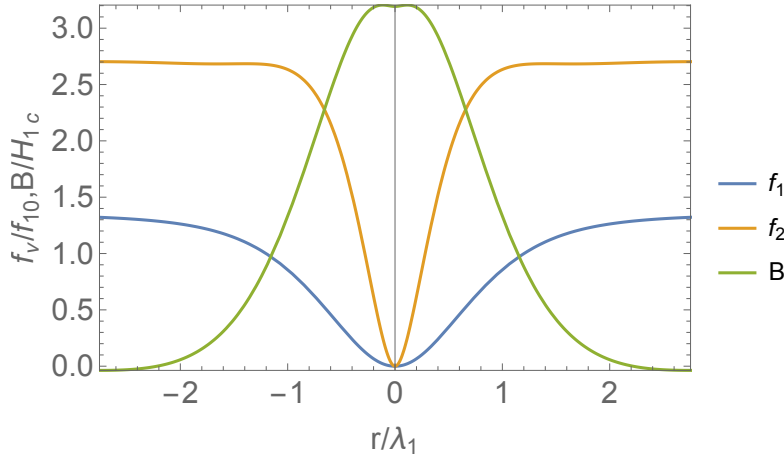

Figure 5.4: Giant vortex solution ($n = 2$) computed using variational method. The order parameters, f_1 and f_2, now behave as $\mathcal{O}\left(\rho^2\right)$ as $\rho \to 0$. The peak in the magnetic field, B, is also much wider and slightly higher compared to the single vortex solutions.

To perform the transformation, we first note that if we convert the two dimensional plane to the complex plane, $z = x + iy$, then the phase factor of the order parameter of the single vortex solution can be written as

$$\exp(i\phi) = \sqrt{(z/z^*)}. \tag{5.17}$$

The plane with a two vortex solution is then mapped back onto a one vortex solution using the conformal transformation

$$z = z'^2 - (d/2)^2. \tag{5.18}$$

Then we can write the full wave function as

$$\Psi_\nu(z, z^*) = \exp\left(i\phi_{\nu 0}\right)\sqrt{\frac{z^2 - (d/2)^2}{z^{*2} - (d/2)^2}}\, f_\nu(z, z^*), \tag{5.19}$$

where we have now formulated the phase factor for the two vortex ansatz, and f_ν is again the magnitude of the order parameter. We require the order parameter to have the following behaviour

$$z \to \pm d/2, \qquad\qquad f_\nu(z, z^*) \to 0, \tag{5.20a}$$

$$|z| \to \infty, \qquad\qquad f_\nu(z, z^*) \to f_{\nu 0}, \tag{5.20b}$$

$$d \gg \xi, \lambda > |z|, \qquad f_\nu(z \pm d/2, z^* \pm d/2) \to f_\nu^{(1)}(|z \pm d/2|), \tag{5.20c}$$

$$d \to 0, \qquad\qquad f_\nu(z, z^*) \to f_\nu^{(2)}(|z|). \tag{5.20d}$$

This behaviour can be achieved by choosing an ansatz that interpolates between the single vortex and giant vortex solutions, plus an interaction term with variational parameters that are to be determined. The ansatz is chosen to be of the form

$$\begin{aligned}
f_\nu(z, z^*) = {}& \frac{w f_\nu^{(1)}\left(|z - d/2|\right) f_\nu^{(1)}\left(|z + d/2|\right)}{f_{\nu 0}} \\
&+ \frac{(1-w)\left|z^2 - (d/2)^2\right|}{|z^2|} f_\nu^{(2)}\left(|z|\right) + \delta f_\nu(z, z^*),
\end{aligned} \tag{5.21}$$

where $f_\nu^{(1)}, (f_\nu^{(2)})$ are the single (giant) vortex solutions respectively, and w is a parameter that interpolates between the two solutions.

The interaction term, $\delta f_\nu(z, z^*)$, must be chosen to vanish at the vortex locations, and must decay sufficiently fast far from the vortex cores. A suitable choice for this is

$$\delta f_\nu(z, z^*) = \frac{|z^2 - (d/2)^2|}{\cosh(\sqrt{2}\,|z|/\xi)} \sum_{i=0}^{i_{\max}} \sum_{j=-i}^{i} f_{\nu,ij}\left[z^{i+j}(z^*)^{i-j}\right]. \tag{5.22}$$

An approximation for the vector potential can likewise be constructed from an interpolation of the single vortex and giant vortex solutions, plus a variational interaction term.

The free energy is again found by placing the ansatz in the equation (4.1) and integrating over the plane. The resulting free energy is again a quartic polynomial in the remaining variational parameters, and can therefore be minimised using Newton's method. A typical solution with two bands and two vortices is shown in figure 5.5. We note that following a contour enclosing one of the vortices, the phase of the order
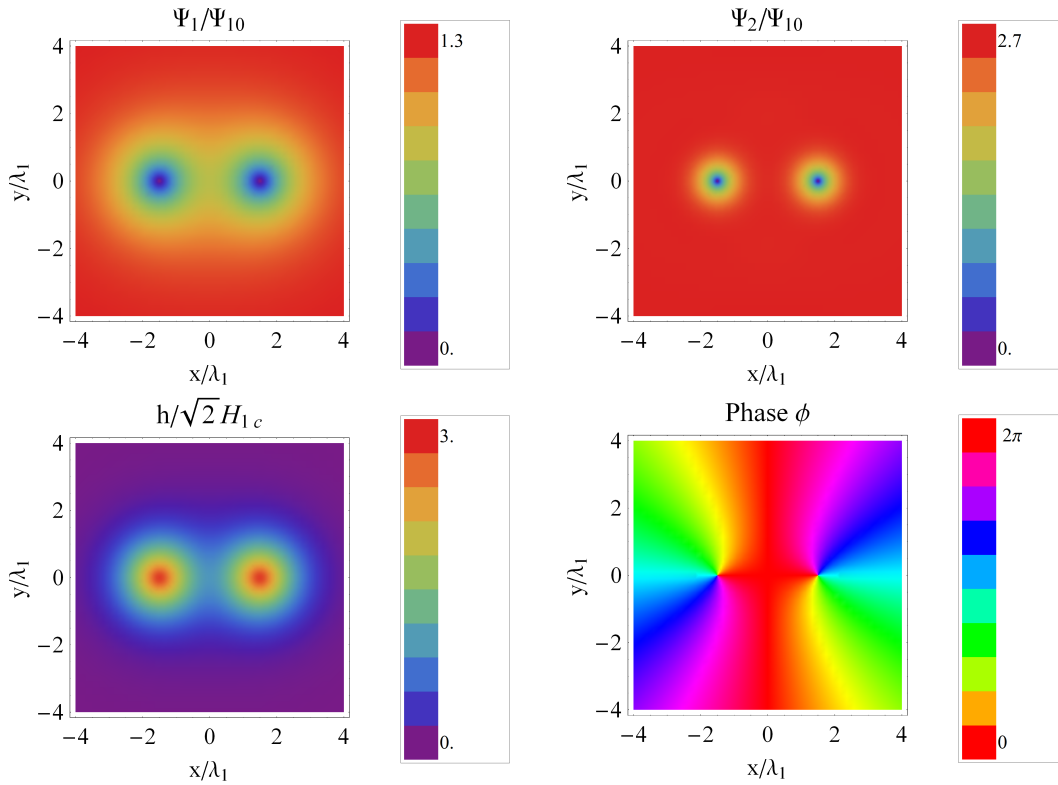
Figure 5.5: Double vortex solution computed using variational method. The phase difference of 2π around each of the individual vortices, and the total phase difference of 4π around both vortices can be seen in the phase plot. In this case there is some overlap of both the first order parameter and the magnetic field (here denoted by h), while the vortices in the second order parameter are well separated.

parameter changes by 2π, while following a large contour that enclose both vortices, the phase of the order parameter shifts by 4π.

In figure 5.6 line scans are shown for a range of vortex separations, d. As expected from the ansatz used to create these solutions, the solutions at large separation approach the form of two independent vortices, and as the separation goes to zero the solution approaches the giant vortex solution. The solution for these two extremes looks as expected. However the intermediate case shown in b) seems to perform far worse, and the behaviour of the order parameter near the origin looks too sharp. This behaviour could improve if more terms were included in the interaction correction, but it is likely that a large number of terms would be needed, since it is in this region that the ansatz is the poorest. It is therefore difficult to rely on results in this intermediate separation with this method.

The double vortex solution can be found for an arbitrary separation distance. Performing this for a large number of separations, we find the free energy for each
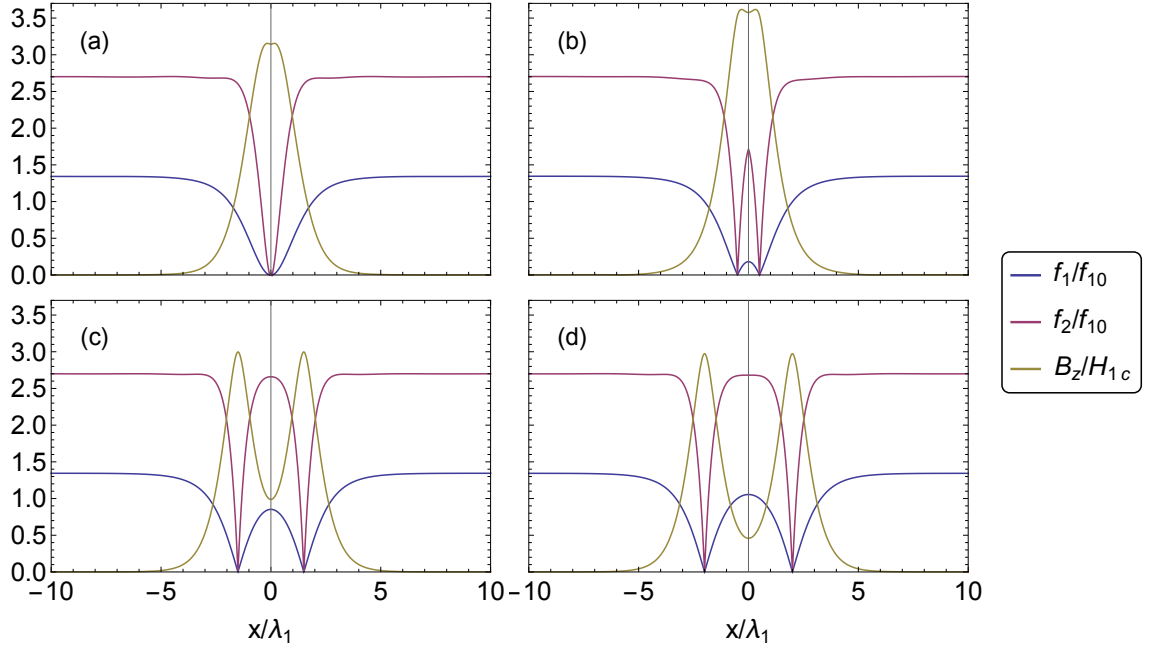
Figure 5.6: Line scan of a series of double vortex solutions computed using the variational method. The vortex separation, d, used for these plots is a) 0.1, b) 1, c) 3, d) 4.
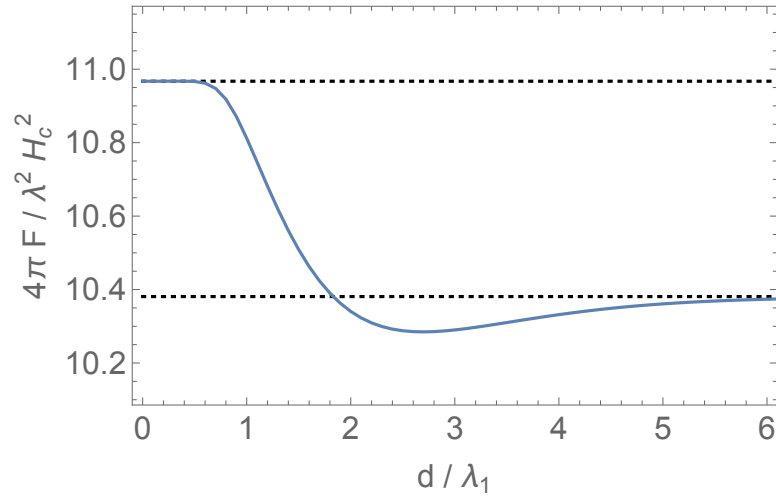

Figure 5.7: Interacting double vortex energy as a function of the distance of separation, d, computed using the variational method. There is a minimum in the free energy when the vortices are at a separation of about 2.7 units.

solution. One such result is shown in figure 5.7. At small separation the free energy is the same as the double vortex solution. With increasing separation, this decreases, reaching a minimum before increasing to the free energy of two essentially noninteracting single vortex states. This shows that for these parameters there is an attraction between vortices at large separation, and a repulsive interaction at small distances. We note that the minimum in the free energy is very shallow, and could be washed out by thermal effects, as well as effects from pinning centres and other imperfections in any real sample.

5.1.4   Time-Dependent Ginzburg-Landau Theory

In GL theory, the aim is to find solutions such that the GL equations are satisfied. These solutions correspond to minima of the free energy. In TDGL an additional time parameter is added such that an initial state evolves towards a minimum of the free energy. After evolving an initial state for a long time, the state should approximately solve the original GL equations.

To evolve the solutions towards a minimum of the free energy, we introduce the phenomenological TDGL equations [112, 149]

$$\frac{\hbar^2}{2m_\nu D_\nu}\frac{\partial \Psi_\nu}{\partial t} = -\frac{\delta F_s}{\delta \Psi_\nu^*} + \zeta_\nu(\mathbf{r}, t), \tag{5.23a}$$

$$\frac{\sigma}{c^2}\frac{\partial \mathbf{A}}{\partial t} = -\frac{\delta F_s}{\delta \mathbf{A}} + \boldsymbol{\zeta}_\mathbf{A}(\mathbf{r}, t), \tag{5.23b}$$

where we have introduced a set of phenomenological parameters. D_ν and σ control how quickly the solution evolves, and ζ_ν and $\boldsymbol{\zeta}_\mathbf{A}$ are thermal noise terms to prevent the solution becoming stuck in metastable states. If we take $\lim_{t\to\infty} \zeta_\nu(t) = 0$, $\lim_{t\to\infty} \boldsymbol{\zeta}_\mathbf{A}(t) = \mathbf{0}$, then this should produce the time-independent solutions in the limit $t \to \infty$.

Performing the variational derivatives, we can write the full equations as

$$\frac{\hbar^2}{2m_\nu D_\nu}\frac{\partial \Psi_\nu}{\partial t} = -\left(a_\nu \Psi_\nu(\mathbf{r}) + b_\nu |\Psi_\nu(\mathbf{r})|^2 \Psi_\nu(\mathbf{r}) + \frac{1}{2m_\nu^*}\Pi(\mathbf{r})^2\Psi_\nu(\mathbf{r})\right.$$
$$\left. + \sum_{\nu'\neq\nu} \gamma_{\nu\nu'}\Psi_{\nu'}(\mathbf{r})\right) + \zeta_\nu(\mathbf{r}, t). \tag{5.24a}$$

$$\frac{\sigma}{c^2}\frac{\partial \mathbf{A}}{\partial t} = \frac{c}{4\pi}\nabla \times \nabla \times \mathbf{A}(\mathbf{r}) + \boldsymbol{\zeta}_\mathbf{A}(\mathbf{r}, t)$$
$$- \sum_\nu \left[-\frac{e^*\hbar}{2im_\nu^*}\left(\Psi_\nu^*(\mathbf{r})\nabla\Psi_\nu(\mathbf{r}) - \Psi_\nu(\mathbf{r})\nabla\Psi_\nu^*(\mathbf{r})\right) - \frac{e^{*2}}{m_\nu^* c}|\Psi_\nu(\mathbf{r})|^2\mathbf{A}(\mathbf{r})\right]. \tag{5.24b}$$
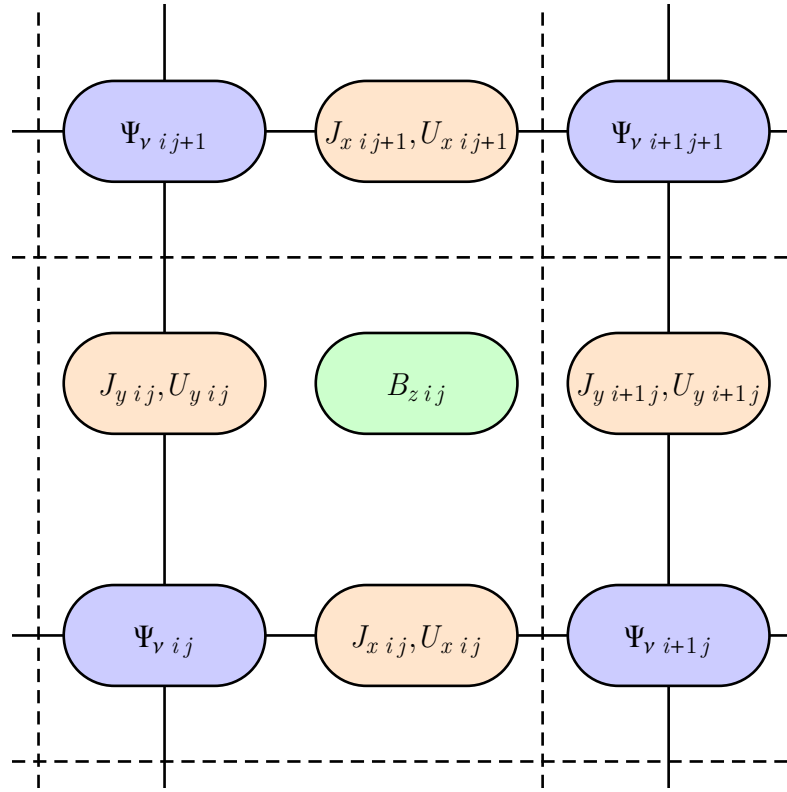
Figure 5.8: The discretisation cell used in TDGL. The four mesh points in the lower left make up a unit cell, and the full mesh is made by repeating this unit cell. The order parameters, Ψ_ν, are located at the vertices, the current, $\mathbf{j}$, and link variables, $\mathbf{U}$, are located on the edges, and the magnetic field, B_z, is located at the centre of the faces.

These equations are very general and can be applied to arbitrary geometries and for a variety of spatial discretisation and time evolution methods. The simplest scheme is a FTCS discretisation scheme for a 2D domain [112, 150, 151]. This method is conditionally stable, and the time step must be chosen small enough. However, the computational cost of each time step is very small with this method.

Before the equations are discretised, the link variables U_x and U_y are introduced. These variables hold the same degrees of freedom as the vector potential and allow the equations to remain gauge-invariant after discretisation.

$$U_x(x,y) = \exp\left(-\mathrm{i}\frac{\varphi_0}{2\pi}\int_{x_0}^{x}\mathrm{d}\xi\, A_x(\xi,y)\right), \tag{5.25a}$$

$$U_y(x,y) = \exp\left(-\mathrm{i}\frac{\varphi_0}{2\pi}\int_{y_0}^{y}\mathrm{d}\xi\, A_y(x,\xi)\right), \tag{5.25b}$$

where x_0, y_0 is some reference point.

To actually implement this, a rectangular domain is chosen with side lengths L_x and L_y respectively. This domain is discretised uniformly with a mesh of $n_x \times n_y$

grid points, so that the step sizes are given by $h_x = L_x/n_x$ and $h_y = L_y/n_y$. A time discretisation with time step k_t is also chosen. For the spatial discretisation, the variables themselves are evaluated at displaced grid points (figure 5.8) [151]. After discretisation the time-step equations using the FTCS scheme become

$$\Psi_{\nu ij}^{(t+1)} = \Psi_{\nu ij}^{(t)} + k_t \frac{2m_\nu D_\nu}{\hbar^2}\left[-\left(a_\nu + b_\nu \left|\Psi_{\nu ij}^{(t)}\right|^2\right)\Psi_{\nu ij}^{(t)} - \sum_{\nu' \neq \nu} \gamma_{\nu\nu'}\Psi_{\nu' ij}^{(t)} + \zeta_{\nu ij}^{(t+1)} \right.$$
$$+\frac{\hbar^2}{2m_\nu}\left(\frac{U_{xij}^{(t)}\Psi_{\nu i+1j}^{(t)} - 2\Psi_{\nu ij}^{(t)} + U_{xi-1j}^{(t)}\Psi_{\nu i-1j}^{(t)}}{h_x^2} + \frac{U_{yij}^{(t)}\Psi_{\nu ij+1}^{(t)} - 2\Psi_{\nu ij}^{(t)} + U_{yij-1}^{(t)}\Psi_{\nu ij-1}^{(t)}}{h_y^2}\right)\right],$$
$$(5.26\text{a})$$

$$U_{xij}^{(t+1)} = U_{xij}^{(t)}$$
$$\times \exp\left[-\frac{ik_t c^2}{\sigma}\text{Im}\left(\frac{c}{4\pi}\frac{W_{zij}^{(t)} - W_{zij-1}^{(t)}}{h_y^2} + \sum_\nu \frac{e^*\hbar}{2m_\nu^*}U_{xij}^{(t)}\Psi_{\nu ij}^{(t+1)*}\Psi_{\nu i+1j}^{(t+1)} + \zeta_{xij}^{(t+1)}\right)\right],$$
$$(5.26\text{b})$$

$$U_{yij}^{(t+1)} = U_{yij}^{(t)}$$
$$\times \exp\left[-\frac{ik_t c^2}{\sigma}\text{Im}\left(\frac{c}{4\pi}\frac{W_{zi-1j}^{(t)} - W_{zij}^{(t)}}{h_x^2} + \sum_\nu \frac{e^*\hbar}{m_\nu^*}U_{yij}^{(t)}\Psi_{\nu ij}^{(t+1)*}\Psi_{\nu ij+1}^{(t+1)} + \zeta_{yij}^{(t+1)}\right)\right],$$
$$(5.26\text{c})$$

$$W_{zij}^{(t+1)} = U_{xij+1}^{(t+1)*}U_{yij}^{(t+1)*}U_{xij}^{(t+1)}U_{yi+1j}^{(t+1)}.$$
$$(5.26\text{d})$$

These are evolved iteratively from initial conditions until the solution converges sufficiently.

After the computation, we can recover the magnetic field

$$B_{zij}^{(t)} = \frac{2\pi}{\varphi_0}\frac{1 - W_{zij}^{(t)}}{ih_x h_y},$$
$$(5.27)$$

which is obtained by considering the exponential of the contour integral of the vector potential along the edges surrounding the magnetic field variable B_{zij} and using Stokes theorem to relate this to the integral of the field.

In addition, we can recover the supercurrent

$$J_{xij}^{(t)} = \sum_\nu \text{Im}\left[\frac{\hbar e^*}{m_\nu h_x}U_{xij}^{(t)}\Psi_{\nu ij}^{(t)*}\Psi_{\nu i+1j}^{(t)}\right],$$
$$(5.28\text{a})$$
$$J_{yij}^{(t)} = \sum_\nu \text{Im}\left[\frac{\hbar e^*}{m_\nu h_y}U_{yij}^{(t)}\Psi_{\nu ij}^{(t)*}\Psi_{\nu ij+1}^{(t)}\right].$$
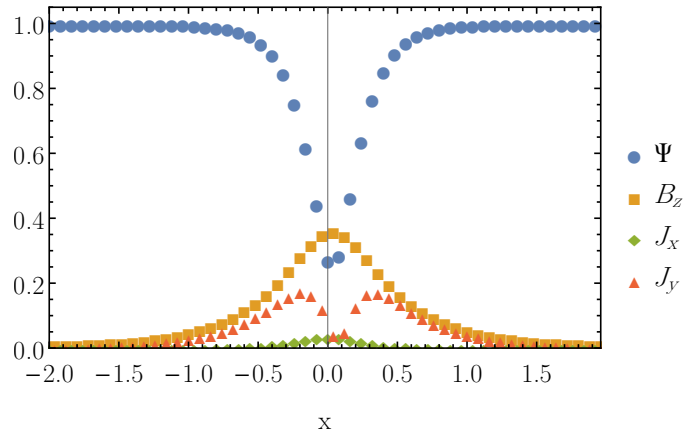$$(5.28\text{b})$$

Figure 5.9: Line scan of a single vortex created using TDGL. Only the magnitude of the order parameter Ψ_1 is shown.

The final piece that is needed to allow this to be performed is to include boundary conditions that allow vortices to be included. Periodic boundary conditions are used in the y direction, while quasi-periodic boundary conditions are imposed in the x direction. The quasi-periodic boundary conditions impose a phase shift of the order parameters and a shift in the vector potential, while observables quantities – the magnitude of the order parameters and the magnetic field – are periodic. The quasi-periodic relations are

$$\Psi_{\nu n_x j} = \Psi_{\nu 0 j} \exp\left(2\pi i n_V j / n_y\right), \tag{5.29a}$$

$$A_{y n_x j} = A_{y 0 j} + \frac{n_V \varphi_0}{L_y}, \tag{5.29b}$$

$$U_{y n_x j} = U_{y 0 j} \exp\left(2\pi i h_y n_V / L_y\right), \tag{5.29c}$$

where n_V is the vortex number to be induced in the sample. When the simulations are initially run, the number of vortices that initially form can be larger than this due to the formation of vortex-antivortex pairs. However these pairs cost energy and eventually annihilate each other.

With this formalism in place, simulations can be run for a superconducting sample. We choose a square computation domain and begin with random initial conditions, then evolve the solution until a stable solution is found.

As a first example, a single vortex is placed in a three-band superconductor. A line scan near the centre of the vortex is shown in figure 5.9, and the full solution is shown in figure 5.10. The vortex was moved to the centre of the domain after the simulation was complete.

In this example, the superconductor is in a trivial case of the TRSB state. All
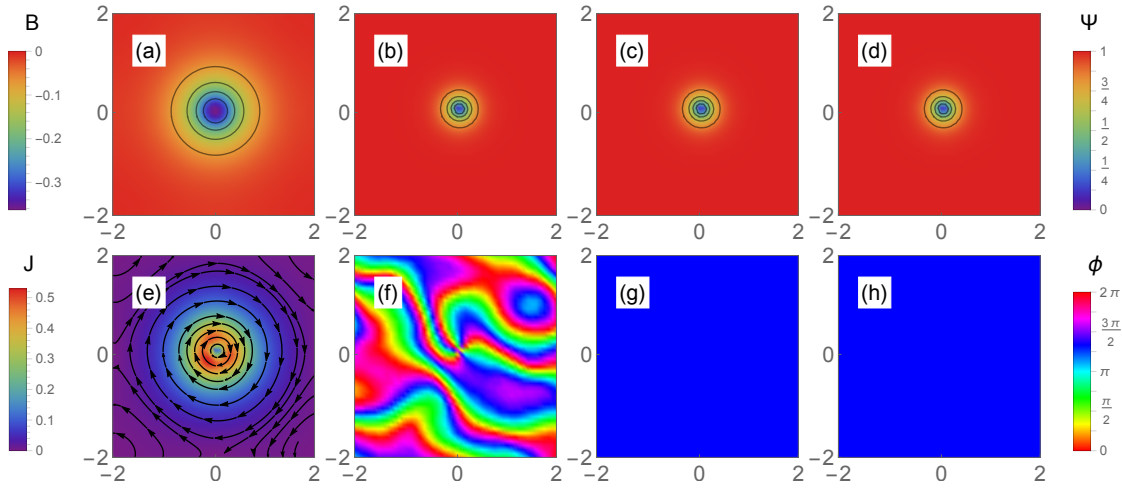
Figure 5.10: Single vortex created using TDGL. a) Magnetic field, b)-d) the magnitude of the order parameters, $|\Psi_\nu|$, scaled to the maximum values, e) the supercurrent, $\mathbf{j}$, f) the sum of the phases of the order parameters, $\sum_\nu \phi_\nu$, g)-h) the phase differences, $\phi_1 - \phi_2$, $\phi_2 - \phi_3$.

three bands are identical with identical repulsive interactions, and so the relative phases between the bands always stays at $4\pi/3$ (the relative phases in g) and h) are constant), and there is an equivalent ground state where the phase differences are instead $2\pi/3$. The line scan shows the linear decay of the order parameters near the centre of the vortex, and the exponential approach to the uniform solution. It can also be seen that the magnetic field is approximately quadratic near the core, and decays exponentially to the bulk. This has good qualitative agreement with the form of the single vortex solution obtained by the previous methods.

Next we consider a two vortex solution (figure 5.12). Decreasing the mass of the first band allows for a bound state between the vortices to form without the solution collapsing to a giant vortex. A line scan is shown in figure 5.11 passing through the centre of one of the vortices and near the centre of the second. The order parameters again behave linearly near the vortex core. In between the two vortices, the order parameters Ψ_2 and Ψ_3 almost reach their bulk values, while Ψ_1 remains far below the bulk value. The distance between the vortices is also small enough that the magnetic field is not able to decay to the bulk value. This confirms the interpretation that there can be a minimum in the energy of a two vortex solution, which was seen in the variational method earlier.

There is a slight perturbation of the phase difference between the bands near the vortex core, and this can especially be seen in (g) but is also visible in (h). Therefore the approximation used earlier that the phase difference between the
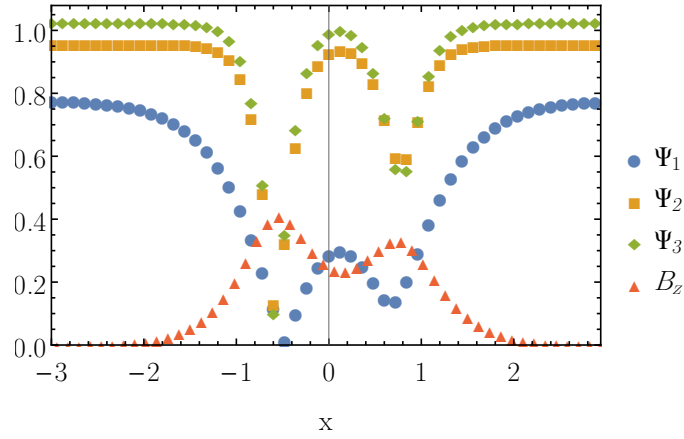
Figure 5.11: Line scan of a double vortex created using TDGL with three order parameters. The order parameters Ψ_2 and Ψ_3 almost obtain their bulk values in between the two vortices, while the order parameter Ψ_1 remains greatly suppressed. The magnetic field also does not decay to zero in this intermediate region, and it is this overlap that prevents the vortices from collapsing further.
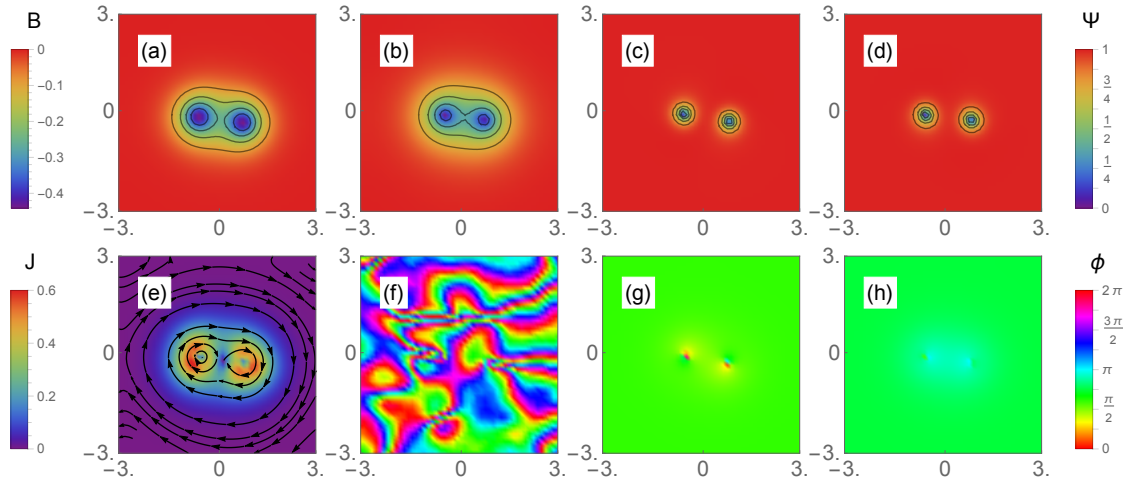

Figure 5.12: Double vortex created using TDGL. a) Magnetic field, b)-d) the magnitude of the order parameters, $|\Psi_\nu|$, scaled to the maximum values, e) the supercurrent, $\mathbf{j}$, f) the sum of the phases of the order parameters, $\sum_\nu \phi_\nu$, g)-h) the phase differences, $\phi_1 - \phi_2$, $\phi_2 - \phi_3$.

bands is constant for the vortex solution is a reasonable approximation, but not exact.

As a final example of vortex states in multiband superconductors we produce an Abrikosov lattice (figure 5.13). In this case we include 8 vortices. We choose parameters such that the bulk material is not a TRSB state, and the first band is stronger than the other two bands. However the longest length scale is the penetration
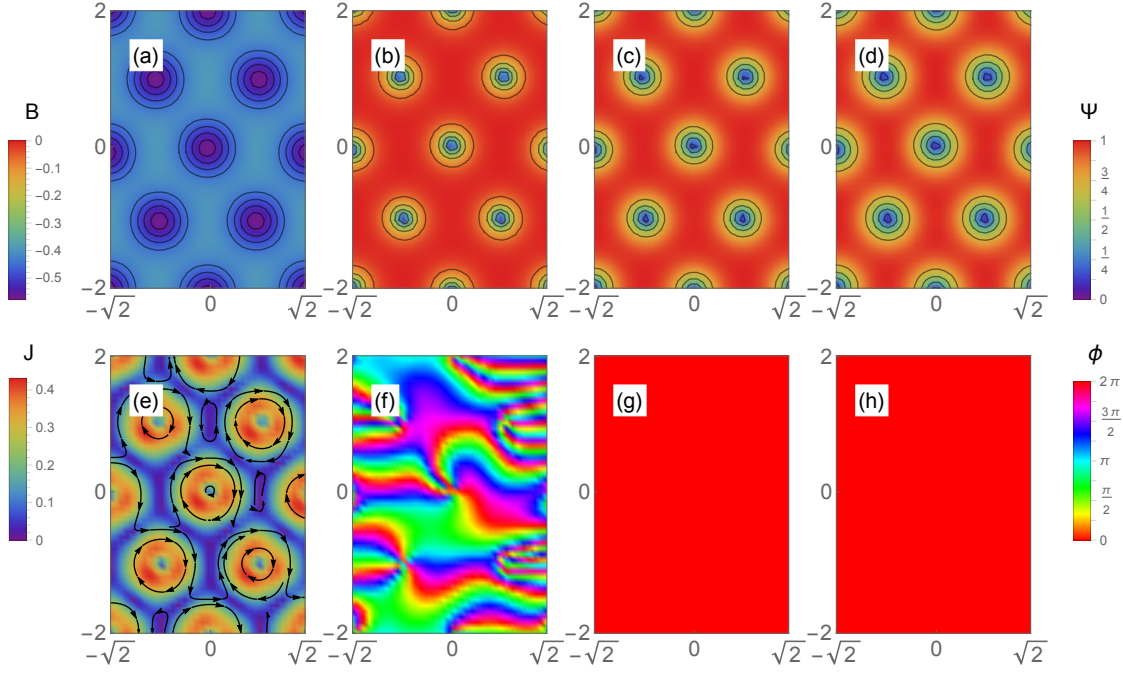
Figure 5.13: Abrikosov lattice of vortices with $n_V = 8$ created using TDGL. a) Magnetic field, b)-d) the magnitude of the order parameters, $|\Psi_\nu|$, scaled to the maximum values, e) the supercurrent, $\mathbf{j}$, f) the sum of the phases of the order parameters, $\sum_\nu \phi_\nu$, g)-h) the phase differences, $\phi_1 - \phi_2$, $\phi_2 - \phi_3$.

depth so that the vortices are repulsive and a stable lattice can form. To allow for the expected triangular lattice ground state, we choose $L_x = L_y/\sqrt{2}$.

As expected, the vortices arrange themselves in an equilateral triangle lattice with uniform spacing. At this density the variation in the magnetic field is quite small. There is also some overlap of the cores in the order parameters so that they do not quite reach the bulk value before they begin to decrease again due to the next vortex.

Increasing the magnetic field further eventually suppresses the order parameters completely, and the magnetic field becomes a constant. The magnetic field can be increased by either decreasing the area of the computational domain or by increasing the number of vortices. The magnetic field where this occurs gives an approximation of H_{c2}.

5.2 Kink Solutions

When a superconductor is in the TRSB state, the ground state is degenerate. In the three-band case, there exist two ground states, corresponding to whether the phases of the gaps are arranged clockwise or anticlockwise (recall figure 3.5). It is possible for the chosen ground state to be different in separate parts of the superconductor. A kink solution connects these ground states.

The kink solution asymptotically approaches the uniform ground states, and evolves from one ground state to the other over a fairly narrow region. This can be viewed as a domain wall separating the two ground states.

At the domain wall, the phases are not in the lowest energy state, so the amplitude of the order parameters is depressed. This depression is also quite localised, occurring over a length of about 2ξ.

Tanaka [109, 152] and later Yanagisawa et al. [114] examined the behaviour of the relative phase along a kink. They show that with the approximation that the magnitude of the gaps remains constant, the relative phases obey the double sine-Gordon equation.

The kink solution always costs energy, so the domain wall will evolve towards a state where the surface area is minimised. This can be viewed as the domains having a surface tension. Garaud and Babaev [153] show that these domain walls can be stabilised by changing the geometry of the boundary or with the use of pinning centres. The idea is that, once the domain wall has formed, it would have to increase in length in order to be removed from the system, and hence is in a meta-stable state. Even more interestingly, the domains can be stabilised by an interaction with vortex states. This can produce a new type of solution, the skyrmion states.

5.3 Skyrmion States

The slight depression along the domain wall can attract and interact with the vortex solutions discussed previously. Considering the fractional vortices in each band separately, a lower energy state can be formed by placing these along the domain wall, rather than having the core of the fractional vortices located at the same point[114, 130]. This allows the magnetic flux associated with the state to spread over a larger area, lowering the energy contribution from the magnetic field.

The simplest skyrmion state contains two quanta of magnetic flux, as a single flux quantum always collapses to a vortex in the absence of any other pinning forces.
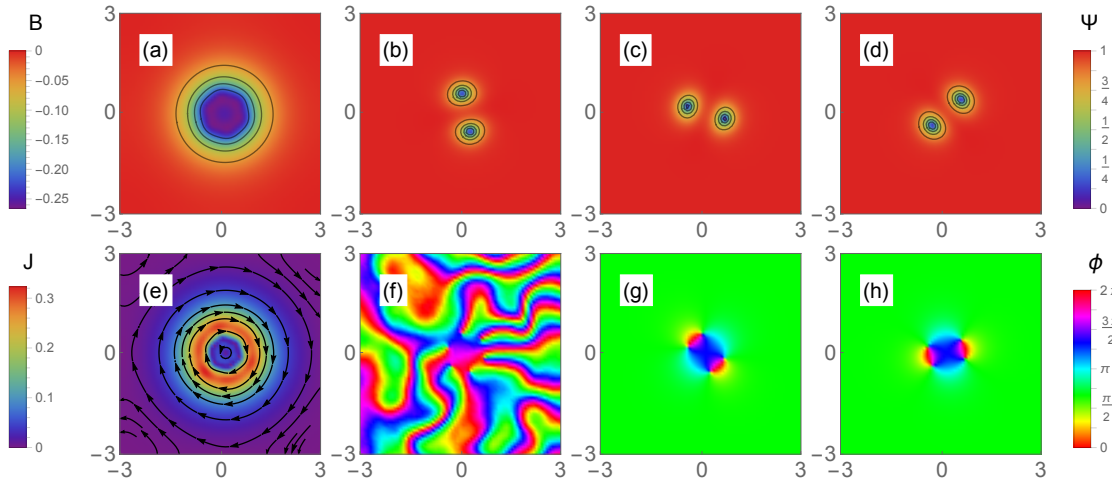
Figure 5.14: Two-quanta skyrmion. a) Magnetic field, b)-d) the magnitude of the order parameters, $|\Psi_\nu|$, scaled to the maximum values, e) the supercurrent, **j**, f) the sum of the phases of the order parameters, $\sum_\nu \phi_\nu$, g)-h) the phase differences, $\phi_1 - \phi_2$, $\phi_2 - \phi_3$.
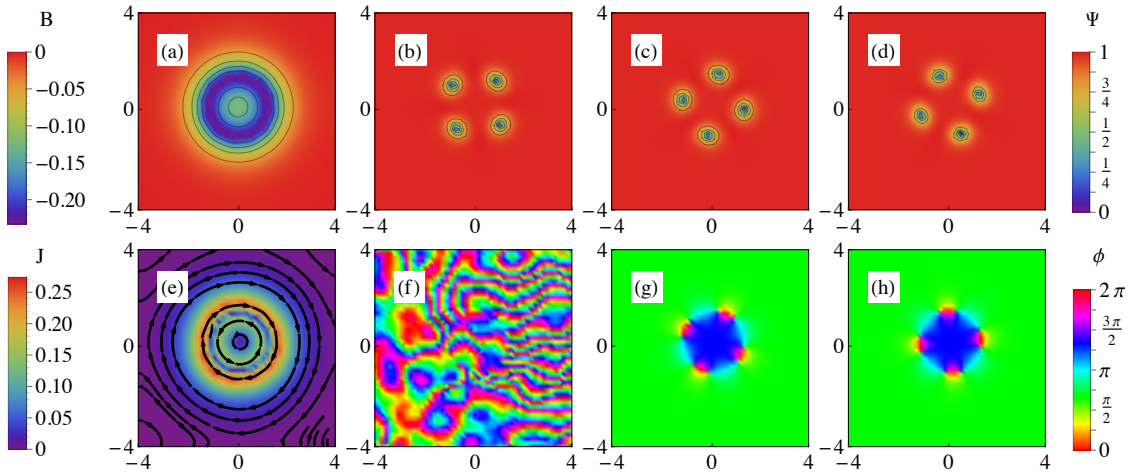

Figure 5.15: Four-quanta skyrmion. a) Magnetic field, b)-d) the magnitude of the order parameters, $|\Psi_\nu|$, scaled to the maximum values, e) the supercurrent, **j**, f) the sum of the phases of the order parameters, $\sum_\nu \phi_\nu$, g)-h) the phase differences, $\phi_1 - \phi_2$, $\phi_2 - \phi_3$.

An example of a two-quanta skyrmion is given in figure 5.14. For this simulation the bands are all equal with equal repulsive interactions and equal masses. The magnetic field (a) contains six peaks arranged in a hexagon, creating a large structure due to the penetration depth being large compared to the separation of the peaks. Associated with each of these peaks is a fractional vortex where one of the order parameters (b)-(d) is in a vortex-like state, with a zero at the centre and a phase difference of 2π around the zero. However, unlike the vortex states we looked at earlier, the location of these fractional vortices in the three bands do not coincide. The phase differences

(g) and (h) show that, outside the skyrmion, the superconductor is in the TRSB state while in the centre of the skyrmion the superconductor is also in the TRSB state, but with the other handedness for the order of the phases.

This is the simplest of the skyrmion states. There exist a hierarchy of states with more quanta of flux. The simplest family of solutions adds additional units of flux quanta along the domain boundary. Examples of these higher order states are given in figure 5.15, which shows a four-quanta skyrmion, and figure 5.16, which shows a five-quanta skyrmion plus a single vortex.

These skyrmion states are very robust and appear spontaneously with a large variety of GL parameters. An example with unequal masses in the different bands is given in figure 5.17. In this case the individual peaks in the magnetic field are harder to identify, and instead two main peaks are visible. Hence this type of skyrmion state would be hard to distinguish experimentally from a double vortex bound state like that seen in figure 5.12.

Other solutions which sometimes appear in these computations develop two horizontal domain walls. This can occur even in the case when only a single flux is placed in the domain. These solutions are unphysical and are only stable in the computations since, in order to remove these domain walls smoothly, the length of the domain walls would initially have to increase. Therefore, when these form in a computation they need to be removed, usually by restarting with a new random initial configuration.

There are two ways to generate these higher order solutions. One is to start from random initial conditions as before, choose the number of flux quanta to put into the system, and then evolve and see which state the system evolves to. The system could evolve to a state where the flux quanta are isolated and form a collection of individual vortices, or they could form one or more skyrmions, or some combination of the two. This method is capable of producing skyrmions with six or so flux quanta, but in larger domains it becomes increasingly likely that some of the flux quanta will instead form isolated vortices (figure 5.16).

Instead, more complicated skyrmions are produced using lower order solutions as a starting point. These solutions are then multiplied together. This creates the main topological structure of a solution. This is used as a new initial configuration, which is evolved as normal to find a new stable solution. This method was used to produce the complicated layered skyrmion shown in figure 5.18, which has an eight-quanta skyrmion surrounding a four-quanta skyrmion.
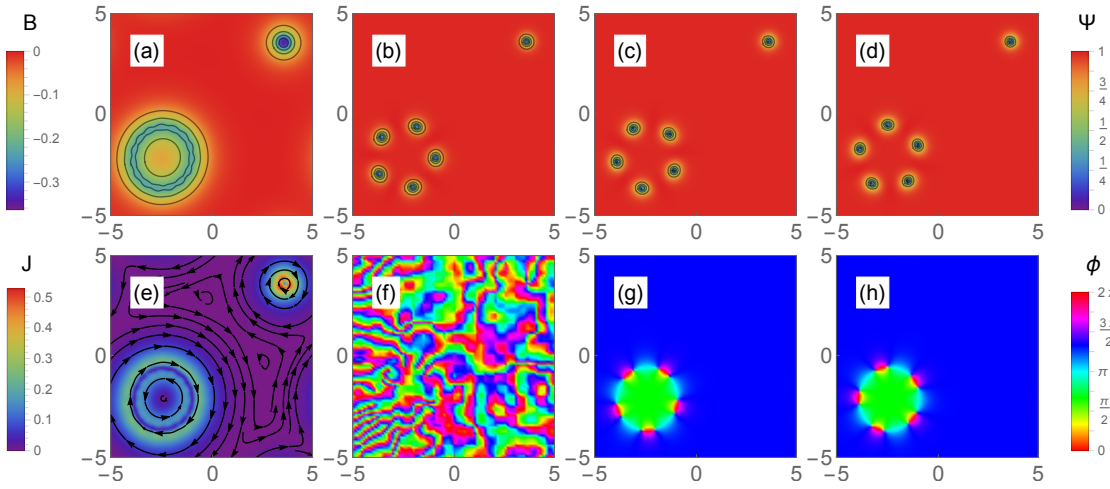
Figure 5.16: Five-quanta skyrmion plus a single vortex. a) Magnetic field, b)-d) the magnitude of the order parameters, $|\Psi_\nu|$, scaled to the maximum values, e) the supercurrent, $\mathbf{j}$, f) the sum of the phases of the order parameters, $\sum_\nu \phi_\nu$, g)-h) the phase differences, $\phi_1 - \phi_2$, $\phi_2 - \phi_3$.

Figure 5.17: Two-quanta skyrmion state with unequal masses. a) Magnetic field, b)-d) the magnitude of the order parameters, $|\Psi_\nu|$, scaled to the maximum values, e) the supercurrent, $\mathbf{j}$, f) the sum of the phases of the order parameters, $\sum_\nu \phi_\nu$, g)-h) the phase differences, $\phi_1 - \phi_2$, $\phi_2 - \phi_3$.
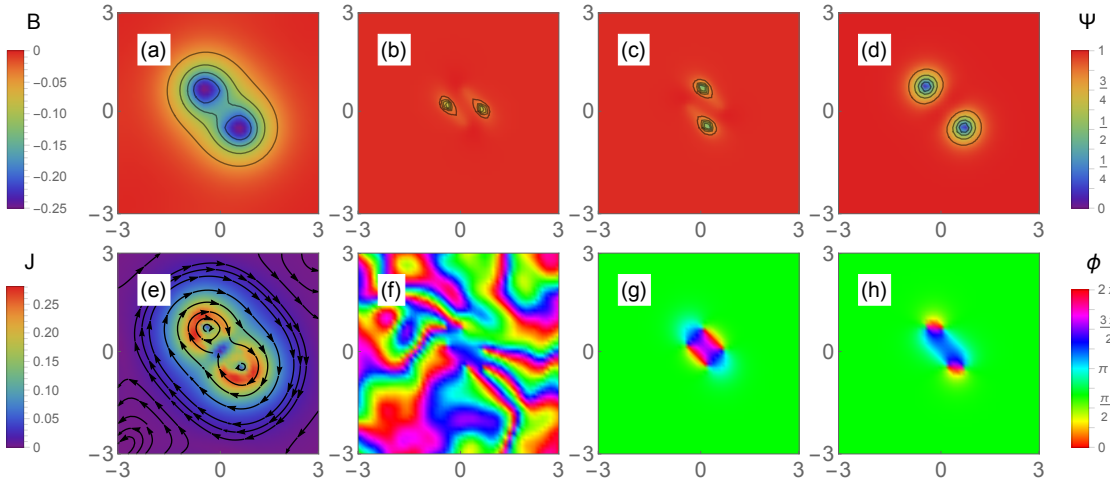
It is quite clear, however, that while these higher skyrmion solutions are at least metastable, they are unlikely to be produced by chance from a random initial condition, and therefore they are unlikely to be seen in practice unless similar control on the formation of these skyrmions can be achieved experimentally. They are also unlikely to remain stable in the presence of large fluctuations, and are expected to break up to form simpler skyrmion and vortex structures unless further techniques are developed to stabilise them.
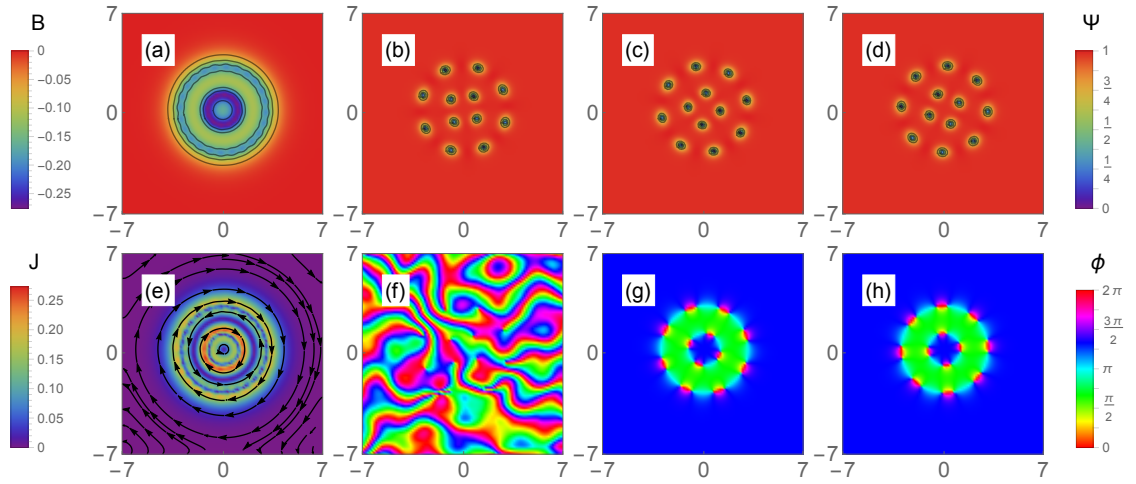
Figure 5.18: Layered skyrmion. An eight-quanta skyrmion surrounds a four-quanta skyrmion. In f) only the phase of the first band is shown for clarity. a) Magnetic field, b)-d) the magnitude of the order parameters, $|\Psi_\nu|$, scaled to the maximum values, e) the supercurrent, $\mathbf{j}$, f) the phase of the first order parameter, ϕ_1, g)-h) the phase differences, $\phi_1 - \phi_2$, $\phi_2 - \phi_3$.

5.4 Summary

In this section we have discussed a selection of numerical methods and applied them to the case of multiband vortex and skyrmion states. We have recovered the vortex states seen in one-band superconductors. It is seen that while the order parameters only have one effective length scale deep inside the superconductor, near a vortex core they can approach their bulk values over different length scales.

The advantages of the variational method is the ability to examine the double vortex state, and to look at the vortex-vortex interaction. This includes the ability to look at the energy of the pair as a function of the distance between them. This shows that for a multiband vortex pair there can be a minimum at a finite distance.

The TDGL method is especially useful for examining a variety of magnetic structures. This method is able to examine single vortex states, vortex pairs and the vortex lattice, as well as a range of skyrmion states. Examples were shown where two vortices formed a bound state (figure 5.12), confirming that there is a minimum in the free energy at a finite separation. At higher magnetic fields the vortex-vortex separation becomes smaller than this length scale and the usual Abrikosov triangular lattice is recovered (figure 5.13).

Finally we used the TDGL method to examine skyrmion states. We found a series of these solutions, and found that they are very robust, appearing often from

random initial conditions. We noted however that the more complex solutions did not arise from random initial conditions, but instead had to be composed from simpler solutions. We expect that the same will be true when looking for skyrmion states in TRSB materials, if and when a TRSB superconductor is found.

CHAPTER SIX

Conclusion

To conclude this thesis, we highlight the key results that we obtained in the study of multiband superconductors, and look at the further developments that could be made following on from this work. Even though the field has been around for a long time there are still many unresolved questions and directions for future research.

6.1   Summary of Results

The main results from our thesis were published in our two papers, and are associated with the TRSB state in three-band BCS theory and with the extension of multiband GL theory to high order in powers of τ $(= 1 - T/T_{\mathrm{c}})$. Additionally we have studied multiband GL theory in the presence of a magnetic field by using numerical approaches to vortex structures.

6.1.1   Multiband BCS

The key result we found in multiband BCS was that, in the TRSB state, the coupled multiband BCS equations can be reduced to a set of one-band BCS equations with a modified coupling strength. In the process of calculating this, we also found a condition on this state and showed that when this condition was satisfied the gaps were always found in the TRSB state. Therefore the TRSB state is more favourable than the state with frustrated phases, but is only a solution to the multiband equations when the triangle inequality condition is satisfied.

Even when the superconductor is not in the TRSB state, the triangle inequality and the reduced one-band solutions still have an effect on the full solutions. One way this occurs is through the location of the T^0 points, where one of the gaps becomes zero below the critical temperature. These points occur when the triangle inequality is satisfied as an equality above the transition from the TRSB state to the standard

superconducting state. The inequality is also satisfied as an equality when two of the bands are degenerate. This leads to a large region of two-band superconductivity, where one of the gaps is identically zero.

The requirement that the gap be a continuous function of the temperature causes these solutions to impact on the gap in a large region of parameter space.

6.1.2   Multiband Ginzburg-Landau

In multiband GL, we extended the theory to include corrections in the expansion, allowing for the theory to be applied further away from the critical temperature. We showed that this works extremely well in one-band. After calculating a large number of terms, we showed that the solution was converging up to 0.9τ, and including additional terms would increase the region of convergence further.

In two-band GL, the expansion can work extremely well, but does not do so in all cases. The expansion performs well when the interband coupling is large, or when the critical temperatures of the uncoupled bands are very different. However, when the critical temperatures of the uncoupled bands are close together and the interband coupling is small, the additional terms in the expansion fail to improve the region of convergence appreciably. It is possible that increasing the number of terms significantly more could overcome this. However the plots of the magnitude of the terms in this region suggests that the expansion is divergent in this case, and that this divergence is related to the appearance of a second critical temperature in the limit that the interband coupling goes to zero.

6.1.3   Multiband Ginzburg-Landau in the Presence of a Magnetic Field

In the last chapter we examined a number of different approaches for finding planar vortex structures in multiband GL theory, including (i) a finite difference and variational approach to solve the one-dimensional vortex equations, (ii) a conformal transformation and variational approach to find a two vortex solution, and (iii) a finite difference approach to solving the TDGL equations on a two-dimensional domain with quasi-periodic boundary conditions. These approaches allowed us to find a number of vortex solutions, and additionally to find skyrmion solutions. These solutions included vortex bound states, indicating that there can exist a minimum in the vortex-vortex interaction, the Abrikosov triangular vortex lattice, and a variety of skyrmions including a layered skyrmion.

6.2 Directions for Future Research

6.2.1 Multiband BCS

There are three main generalisations to be looked at for the multiband BCS result. First, it would be interesting to look at four- and five-bands and see if a similar reduction can occur. The result examined here is only at the mean-field theory level. It would be very exciting if a similar result was found to hold when including quantum fluctuations, either as an expansion or with a full quantum treatment. Finally we would like to perform this approach in a similar manner to another model, such as multiband Eliashberg theory, or a multiband Hubbard model. If this could be performed, it would show that these reduced one-band solutions have a deeper relation with the TRSB state, and give the reduced gaps solutions a more fundamental position in the theory of TRSB superconductors.

6.2.2 Multiband Ginzburg-Landau

The extended GL theory we have presented only contains terms which provide corrections in the expansion of the magnitude of the order parameters. It has been shown by Peeters and co-workers how to include the first order correction to the gradient and magnetic terms. We would like to include similar terms in the higher expansion in a systematic way. This would likely involve a diagrammatic approach to track these terms correctly. This extended expansion could then be applied to find better approximations to the critical fields of multiband superconductors.

In the multiband expansion we showed that the expansion failed in some cases. This is likely due to singularities or branch cuts that are near the critical temperature of the second band in the uncoupled limit. We would like to be able to find and characterise these singularities and see how they move in the complex plane as the interband coupling is varied. We would like to investigate this both within the extended multiband GL theory and multiband BCS theory.

Additionally, we would like to find an expansion that could be applied to lower temperatures for all multiband superconductors. This is of significant interest as this could then be used to confirm whether skyrmion states remain as stable solutions within the extended model, or whether they are artefacts of the truncation and only exist in traditional multiband GL theory. The extended GL model is currently unable to address this issue as it is unable to be applied below the transition to the TRSB state, since the gap is not analytic at this point. Since the skyrmion states

have only been found above the TRSB background, this is a significant obstacle for applications of the extended GL model.

6.2.3 Vortex and Skyrmion States

More work could also be performed on the vortex and skyrmion states with traditional GL theory. We would like to look at these states in nanoscopic sized samples and investigate how edge effects modify these solutions. As highlighted in our review article [3], other aspects of interest in nanoscale superconductivity include effects due to the breakdown of the band structure, the resulting discrete quantum states (parametrised by the Kubo gap), and the influence on pairing when there are an even or odd number of available electrons.

We would also like to develop additional methods for finding vortices, such as a finite element method which could be applied to both two- and three-dimensional samples, as well as improving the speed of convergence of the methods investigated so far.

Bibliography

[1] B. J. Wilson and M. P. Das, "Time-reversal-symmetry-broken state in the BCS formalism for a multi-band superconductor", J. Phys.: Condens. Matter **25**, 425702 (2013).

[2] B. J. Wilson and M. P. Das, "Beyond the standard model of Ginzburg-Landau theory: multiband superconductors", J. Phys.: Condens. Matter **26**, 325701 (2014).

[3] M. P. Das and B. J. Wilson, "Novel superconductivity: from bulk to nano systems", Adv. Nat. Sci.: Nanosci. Nanotechnol. **6**, 013001 (2015).

[4] X.-W. Guan, Z.-Q. Ma, and B. Wilson, "One-dimensional multicomponent fermions with δ-function interaction in strong- and weak-coupling limits: κ-component Fermi gas", Phys. Rev. A **85**, 033633 (2012).

[5] B. Wilson, A. Foerster, C. Kuhn, I. Roditi, and D. Rubeni, "A geometric wave function for a few interacting bosons in a harmonic trap", Phys. Lett. A **378**, 1065 (2014).

[6] B. J. Wilson and M. P. Das, "Multi-band superconductivity", in the Sixth International Conference on Advanced Materials and Nanotechnology (Feb. 11–15, 2013).

[7] B. J. Wilson and M. P. Das, "Phase diagram and chiral skyrmions in three band superconductors", in the 14th International Workshop on Vortex Matter in Superconductors (May 21–28, 2013).

[8] M. P. Das and B. J. Wilson, "Beyond the standard model of GL theory", in the 4th International Conference on Superconductivity and Magnetism (Apr. 27–, May 2, 2014).

[9] H. K. Onnes, "The superconductivity of mercury", Comm. Phys. Lab. Univ. Leiden **122**, 124 (1911).

[10] H. K. Onnes, "On the sudden rate at which the resistance of mercury disappears", Akad. van Wetenschappen **14**, 818 (1911).

[11] W. Meissner and R. Ochsenfeld, "Ein neuer effekt bei eintritt der supraleitfähigkeit", German, Naturwissenschaften **21**, 787 (1933).

[12] F. London and H. London, "The electromagnetic equations of the supraconductor", English, Proc. R. Soc. London, Ser. A **149**, pp. 71 (1935).

[13] A. B. Pippard, "The surface energies of superconductors", Math. Proc. Cambridge **47**, 617 (1951).

[14] A. B. Pippard, "An experimental and theoretical study of the relation between magnetic field and current in a superconductor", Proc. R. Soc. London, Ser. A **216**, 547 (1953).

[15] L. D. Landau, "On the theory of phase transitions", Zh. Eksp. Teor. Fiz. **7**, 19 (1937).

[16] L. D. Landau and V. I. Ginzburg, Zh. Eksp. Teor. Fiz. **20**, 546 (1950), English translation in: L. D. Landau, *Collected Papers of LD Landau*, edited by D. ter Haar (Pergamon Press, Oxford, 1965).

[17] A. A. Abrikosov, "O magnitnykh svoistvakh sverkhprovodnikov vtoroi gruppy", Zh. Eksp. Teor. Fiz. **32**, 1442 (1957), English translation in A. A. Abrikosov, "On the magnetic properties of superconductors of the second group", Sov. Phys. JETP **5**, 1174 (1957).

[18] D Cribier, B Jacrot, L Madhov Rao, and B Farnoux, "Evidence from neutron diffraction for a periodic structure of the magnetic field in a niobium superconductor", Phys. Lett. **9**, 106 (1964).

[19] U. Essmann and H. Träuble, "The direct observation of individual flux lines in type II superconductors", Phys. Lett. A **24**, 526 (1967).

[20] H. Träuble and U. Essmann, "Flux-line arrangement in superconductors as revealed by direct observation", J. Appl. Phys. **39**, 4052 (1968).

[21] K. Fossheim and A. Sudbø, *Superconductivity:Physics and Applications* (John Wiley & Sons, Chichester, 2004).

[22] E. H. Brandt, "The flux-line lattice in superconductors", Rep. Prog. Phys. **58**, 1465 (1995).

[23] E. Maxwell, "Isotope effect in the superconductivity of mercury", Phys. Rev. **78**, 477 (1950).

[24] C. A. Reynolds, B. Serin, W. H. Wright, and L. B. Nesbitt, "Superconductivity of isotopes of mercury", Phys. Rev. **78**, 487 (1950).

[25] H. K. Onnes and W. Tuyn, Leiden Comm. **160b**, 451 (1922).

[26] H. Fröhlich, "Theory of the superconducting state. I. the ground state at the absolute zero of temperature", Phys. Rev. **79**, 845 (1950).

[27] J. Bardeen, "Electron-vibration interactions and superconductivity", Rev. Mod. Phys. **23**, 261 (1951).

[28] J. Bardeen and D. Pines, "Electron-phonon interaction in metals", Phys. Rev. **99**, 1140 (1955).

[29] G. S. Blevins, W. Gordy, and W. M. Fairbank, "Superconductivity at millimeter wave frequencies", Phys. Rev. **100**, 1215 (1955).

[30] M. Tinkham, *Documents on Modern Physics: Superconductivity*, 1st ed. (Gordon and Breach, 1965).

[31] L. N. Cooper, "Bound electron pairs in a degenerate Fermi gas", Phys. Rev. **104**, 1189 (1956).

[32] J. Bardeen, L. N. Cooper, and J. R. Schrieffer, "Microscopic theory of superconductivity", Phys. Rev. **106**, 162 (1957).

[33] J. Bardeen, L. N. Cooper, and J. R. Schrieffer, "Theory of superconductivity", Phys. Rev. **108**, 1175 (1957).

[34] N. N. Bogoliubov, "A new method in the theory of superconductivity. 1.", Sov. Phys. JETP **7**, 41 (1958).

[35] J. G. Valatin, "Comments on the theory of superconductivity", Il Nuovo Cimento **7**, 843 (1958).

[36] L. P. Gor'kov, "Microscopic derivation of the Ginzburg-Landau equations in the theory of superconductivity", Sov. Phys. JETP **9**, 1364 (1959).

[37] A. B. Migdal, "Interaction between electrons and lattice vibrations in a normal metal", Sov. Phys. JETP **7**, 996 (1958).

[38] G. M. Eliashberg, "Interactions between electrons and lattice vibrations in a superconductor", Sov. Phys. JETP **11** (1960).

[39] G. M. Eliashberg, "Temperature Green's function for electrons in a superconductor", Sov. Phys. JETP **12**, 1000 (1961).

[40] Y. Nambu, "Quasi-particles and gauge invariance in the theory of superconductivity", Phys. Rev. **117**, 648 (1960).

[41] F Marsiglio and J. Carbotte, in *Superconductivity: volume 1: conventional and unconventional superconductors*, edited by K.-H. Bennemann and J. B. Ketterson (Springer, Berlin, 2008), pp. 73–162.

[42] G. Kerker and K. Bennemann, "Theory for strong-coupling superconductivity in transition-metal alloys", Solid State Commun. **15**, 29 (1974).

[43] W. L. McMillan, "Transition temperature of strong-coupled superconductors", Phys. Rev. **167**, 331 (1968).

[44] P. Anderson, "Theory of dirty superconductors", J. Phys. Chem. Solids **11**, 26 (1959).

[45] A. A. Abrikosov and L. P. Gor'kov, "K teorii sverkhprovodyashchikh splavov. I. elektrodinamika splavov pri absolyutnom nule", Zh. Eksp. Teor. Fiz. **35**, 1558 (1958), English translation in: A. A. Abrikosov and L. P. Gor'kov, "On the theory of superconducting alloys, I. the electrodynamics of alloys at absolute zero", Sov. Phys. JETP **8**, 1090 (1959).

[46] A. A. Abrikosov and L. P. Gor'kov, "K teorii sverkhprovodyashchikh splavov s paramagnitnymi primesyami", Zh. Eksp. Teor. Fiz. **39**, 1781 (1960), English translation in A. A. Abrikosov and L. Gor'kov, "Contribution to the theory of superconducting alloys with paramagnetic impurities", Sov. Phys. JETP **12**, 1243 (1961).

[47] C. Caroli, P. de Gennes, and J. Matricon, "Coherence length and penetration depth of dirty superconductors", English, Physik der kondensierten Materie **1**, 176 (1963).

[48] I. Affleck and J. B. Marston, "Large-n limit of the Heisenberg-Hubbard model: implications for high-T_c superconductors", Phys. Rev. B **37**, 3774 (1988).

[49] J. Hirsch, "Singlet pairs, covalent bonds, superexchange, and superconductivity", Phys. Lett. A **136**, 163 (1989).

[50] T. C. Choy and M. P. Das, "Attractive pairing potential from the repulsive Hubbard model", Phys. Rev. B **47**, 8942 (1993).

[51] T. A. Maier, M. Jarrell, T. C. Schulthess, P. R. C. Kent, and J. B. White, "Systematic study of d-wave superconductivity in the 2D repulsive Hubbard model", Phys. Rev. Lett. **95**, 237001 (2005).

[52] M. P. Das and J Mahanty, eds., *Modern perspectives in many-body physics, Proceedings of the sixth physics summer school*, Vol. 1, (Canberra, Australia, Jan. 11–29, 1993), The Australian National University (World Scientific, Singapore, 1994).

[53] B. D. Josephson, "Possible new effects in superconductive tunnelling", Phys. Lett. **1**, 251 (1962).

[54] G. Eilenberger, "Transformation of Gorkov's equation for type II superconductors into transport-like equations", English, Zeitschrift für Physik **214**, 195 (1968).

[55] K. D. Usadel, "Generalized diffusion equation for superconducting alloys", Phys. Rev. Lett. **25**, 507 (1970).

[56] A. A. Shanenko, M. V. Milošević, F. M. Peeters, and A. V. Vagov, "Extended Ginzburg-Landau formalism for two-band superconductors", Phys. Rev. Lett. **106**, 047005 (2011).

[57] A. V. Vagov, A. A. Shanenko, M. V. Milošević, V. M. Axt, and F. M. Peeters, "Extended Ginzburg-Landau formalism: systematic expansion in small deviation from the critical temperature", Phys. Rev. B **85**, 014502 (2012).

[58] A. Vagov, A. A. Shanenko, M. V. Milošević, V. M. Axt, and F. M. Peeters, "Two-band superconductors: extended Ginzburg-Landau formalism by a systematic expansion in small deviation from the critical temperature", Phys. Rev. B **86**, 144514 (2012).

[59] S. N. Klimin, J. Tempere, and J. T. Devreese, "Extended Ginzburg-Landau functional for two-band superfluid Fermi gases", version 4, (2013), arXiv:`1309.1421` `[cond-mat]`.

[60] J. Eisenstein, "Superconducting elements", Rev. Mod. Phys. **26**, 277 (1954).

[61] J. Tuoriniemi, K. Juntunen-Nurmilaukas, J. Uusvuori, E. Pentti, A. Salmela, and A. Sebedash, "Superconductivity in lithium below 0.4 millikelvin at ambient pressure", Nature **447**, 187 (2007).

[62] D. K. Finnemore, T. F. Stromberg, and C. A. Swenson, "Superconducting properties of high-purity niobium", Phys. Rev. **149**, 231 (1966).

[63] B. T. Matthias, T. H. Geballe, and V. B. Compton, "Superconductivity", Rev. Mod. Phys. **35**, 1 (1963).

[64] J. Bednorz and K. Müller, "Possible high T_c superconductivity in the Ba-La-Cu-O system", Zeitschrift für Physik B Condensed Matter **64**, 189 (1986).

[65] A. Schilling, M. Cantoni, J. D. Guo, and H. R. Ott, "Superconductivity above 130 K in the Hg-Ba-Ca-Cu-O system", Nature **363**, 56 (1993).

[66] C. W. Chu, L. Gao, F. Chen, Z. J. Huang, R. L. Meng, and Y. Y. Xue, "Superconductivity above 150 K in $HgBa_2Ca_2Cu_3O_8 + \delta$ at high pressures", Nature **365**, 323 (1993).

[67] D. H. Lee and J. Ihm, "Two-band model for high T_c superconductivity in La$_{2-x}$(Ba,Sr)$_x$CuO$_4$", Solid State Commun. **62**, 811 (1987).

[68] V. Kresin and S. Wolf, "Multigap structure in the cuprates", Physica C **169**, 476 (1990).

[69] M. E. Jones and R. E. Marsh, "The preparation and structure of magnesium boride, MgB$_2$", J. Am. Chem. Soc. **76**, 1434 (1954).

[70] R. M. Swift and D. White, "Low temperature heat capacities of magnesium diboride (MgB$_2$) and magnesium tetraboride (MgB$_4$)", J. Am. Chem. Soc. **79**, 3641 (1957).

[71] J. Nagamatsu, N. Nakagawa, T. Muranaka, Y. Zenitani, and J. Akimitsu, "Superconductivity at 39K in magnesium diboride", Nature **410**, 63 (2001).

[72] S. L. Bud'ko, G. Lapertot, C. Petrovic, C. E. Cunningham, N. Anderson, and P. C. Canfield, "Boron isotope effect in superconducting MgB$_2$", Phys. Rev. Lett. **86**, 1877 (2001).

[73] J. Kortus, I. I. Mazin, K. D. Belashchenko, V. P. Antropov, and L. L. Boyer, "Superconductivity of metallic boron in MgB$_2$", Phys. Rev. Lett. **86**, 4656 (2001).

[74] M. Iavarone, G. Karapetrov, A. E. Koshelev, W. K. Kwok, G. W. Crabtree, D. G. Hinks, W. N. Kang, E.-M. Choi, H. J. Kim, H.-J. Kim, and S. I. Lee, "Two-band superconductivity in MgB$_2$", Phys. Rev. Lett. **89**, 187002 (2002).

[75] Y. G. Ponomarev, S. A. Kuzmichev, M. G. Mikheev, M. V. Sudakova, S. N. Tchesnokov, N. Z. Timergaleev, A. V. Yarigin, E. G. Maksimov, S. I. Krasnosvobodtsev, A. V. Varlashkin, M. A. Hein, G. Müller, H. Piel, L. G. Sevastyanova, O. V. Kravchenko, K. P. Burdina, and B. M. Bulychev, "Evidence for a two-band behavior of MgB$_2$ from point-contact and tunneling spectroscopy", Solid State Commun. **129**, 85 (2004).

[76] F. Bouquet, R. A. Fisher, N. E. Phillips, D. G. Hinks, and J. D. Jorgensen, "Specific heat of Mg^{11}B$_2$: evidence for a second energy gap", Phys. Rev. Lett. **87**, 047001 (2001).

[77] H. J. Choi, D. Roundy, H. Sun, M. L. Cohen, and S. G. Louie, "The origin of the anomalous superconducting properties of MgB$_2$", Nature **418**, 758 (2002).

[78] H. J. Choi, D. Roundy, H. Sun, M. L. Cohen, and S. G. Louie, "First-principles calculation of the superconducting transition in MgB$_2$ within the anisotropic Eliashberg formalism", Phys. Rev. B **66**, 020513 (2002).

[79] X. X. Xi, "Two-band superconductor magnesium diboride", Rep. Prog. Phys. **71**, 116501 (2008).

[80] M. Zehetmayer, "A review of two-band superconductivity: materials and effects on the thermodynamic and reversible mixed-state properties", Supercond. Sci. Technol. **26**, 043001 (2013).

[81] Y. Kamihara, H. Hiramatsu, M. Hirano, R. Kawamura, H. Yanagi, T. Kamiya, and H. Hosono, "Iron-based layered superconductor: LaOFeP", J. Am. Chem. Soc. **128**, 10012 (2006).

[82] Y. Kamihara, T. Watanabe, M. Hirano, and H. Hosono, "Iron-based layered superconductor La[$O_{1-x}F_x$]FeAs ($x = 0.05 - 0.12$) with $T_c = 26K$", J. Am. Chem. Soc. **130**, 3296 (2008).

[83] K. Ishida, Y. Nakai, and H. Hosono, "To what extent iron-pnictide new superconductors have been clarified: a progress report", J. Phys. Soc. Jpn. **78**, 062001 (2009).

[84] I. I. Mazin and J. Schmalian, "Pairing symmetry and pairing state in ferropnictides: theoretical overview", Physica C **469** (2009).

[85] J. A. Wilson, "A perspective on the Fe-based superconductors", J. Phys.: Condens. Matter **22**, 203201 (2010).

[86] E. A. Ekimov, V. A. Sidorov, E. D. Bauer, N. N. Mel'nik, N. J. Curro, J. D. Thompson, and S. M. Stishov, "Superconductivity in diamond", Nature **428**, 542 (2004).

[87] L. Boeri, J. Kortus, and O. K. Andersen, "Three-dimensional MgB_2-type superconductivity in hole-doped diamond", Phys. Rev. Lett. **93**, 237002 (2004).

[88] M. Kociak, A. Y. Kasumov, S. Guéron, B. Reulet, I. I. Khodos, Y. B. Gorbatov, V. T. Volkov, L. Vaccarini, and H. Bouchiat, "Superconductivity in ropes of single-walled carbon nanotubes", Phys. Rev. Lett. **86**, 2416 (2001).

[89] N. Emery, C. Hérold, J.-F. Marêché, and P. Lagrange, "Synthesis and superconducting properties of CaC_6", Sci. Technol. Adv. Mater. **9**, 044102 (2008).

[90] K. Tanigaki, T. W. Ebbesen, S. Saito, J. Mizuki, J. S. Tsai, Y. Kubo, and S. Kuroshima, "Superconductivity at 33 K in $Cs_xRb_yC_60$", Nature **352**, 222 (1991).

[91] G. Knebel, D. Aoki, J.-P. Brison, L. Howald, G. Lapertot, J. Panarin, S. Raymond, and J. Flouquet, "Competition and/or coexistence of antiferromagnetism and superconductivity in CeRhIn$_5$ and CeCoIn$_5$", Physica Status Solidi B **247**, 557 (2010).

[92] J. A. Bert, B. Kalisky, C. Bell, M. Kim, Y. Hikita, H. Y. Hwang, and K. A. Moler, "Direct imaging of the coexistence of ferromagnetism and superconductivity at the LaAlO$_3$/SrTiO$_3$ interface", Nat. Phys. **7**, 767 (2011).

[93] A. Gabovich, A. Voitenko, and M. Ausloos, "Charge- and spin-density waves in existing superconductors: competition between Cooper pairing and Peierls or excitonic instabilities", Phys. Rep. **367**, 583 (2002).

[94] N. Kimura and I. Bonalde, in *Non-centrosymmetric superconductors*, Vol. 847, edited by E. Bauer and M. Sigrist, Lecture Notes in Physics (Springer Berlin Heidelberg, 2012), pp. 35–79.

[95] H. Suhl, B. T. Matthias, and L. R. Walker, "Bardeen-Cooper-Schrieffer theory of superconductivity in the case of overlapping bands", Phys. Rev. Lett. **3**, 552 (1959).

[96] V. A. Moskalenko, "Superconductivity in metals with overlapping energy bands", Fiz. Metal. Metalloved **8**, 2518 (1959).

[97] J. Peretti, "Superconductivity of transition elements", Phys. Lett. **2**, 275 (1962).

[98] J. Kondo, "Superconductivity in transition metals", Prog. Theor. Phys. **29**, 1 (1963).

[99] B. T. Geilikman, R. O. Zaitsev, and V. Z. Kresin, "Properties of superconductors having overlapping bands", Sov. Phys.: Solid State **9** (1967).

[100] D. R. Tilley, "The Ginzburg-Landau equations for pure two band superconductors", Proc. Phys. Soc. **84**, 573 (1964).

[101] A. J. Leggett, "Number-phase fluctuations in two-band superconductors", Prog. Theor. Phys. **36**, 901 (1966).

[102] G. Blumberg, A. Mialitsin, B. S. Dennis, M. V. Klein, N. D. Zhigadlo, and J. Karpinski, "Observation of Leggett's collective mode in a multiband MgB$_2$ superconductor", Phys. Rev. Lett. **99**, 227002 (2007).

[103] J. W. Garland, "Mechanisms for superconductivity in the transition metals", Phys. Rev. Lett. **11**, 111 (1963).

[104] Y. Singh, C. Martin, S. L. Bud'ko, A. Ellern, R. Prozorov, and D. C. Johnston, "Multigap superconductivity and Shubnikov-de Haas oscillations in single crystals of the layered boride OsB_2", Phys. Rev. B **82**, 144532 (2010).

[105] H. Kim, M. A. Tanatar, Y. J. Song, Y. S. Kwon, and R. Prozorov, "Nodeless two-gap superconducting state in single crystals of the stoichiometric iron pnictide LiFeAs", Phys. Rev. B **83**, 100502 (2011).

[106] R. Khasanov, M. Bendele, A. Amato, K. Conder, H. Keller, H.-H. Klauss, H. Luetkens, and E. Pomjakushina, "Evolution of two-gap behavior of the superconductor $FeSe_{1-x}$", Phys. Rev. Lett. **104**, 087004 (2010).

[107] Y. Tanaka and T. Yanagisawa, "Chiral state in three-gap superconductors", Solid State Commun. **150**, 1980 (2010).

[108] R. G. Dias and A. M. Marques, "Frustrated multiband superconductivity", Supercond. Sci. Technol. **24**, 085009 (2011).

[109] Y. Tanaka, "Phase instability in multi-band superconductors", J. Phys. Soc. Jpn. **70**, 2844 (2001).

[110] M. E. Zhitomirsky and V.-H. Dao, "Ginzburg-Landau theory of vortices in a multigap superconductor", Phys. Rev. B **69**, 054508 (2004).

[111] M. M. Doria, A. R. de C. Romaguera, and F. M. Peeters, "The ground states of the two-component order parameter superconductor", Europhys. Lett. **92**, 17004 (2010).

[112] S.-Z. Lin and X. Hu, "Vortex states and the phase diagram of a multiple-component Ginzburg-Landau theory with competing repulsive and attractive vortex interactions", Phys. Rev. B **84**, 214505 (2011).

[113] L. Komendová, M. V. Milošević, A. A. Shanenko, and F. M. Peeters, "Different length scales for order parameters in two-gap superconductors: extended Ginzburg-Landau theory", Phys. Rev. B **84**, 064522 (2011).

[114] T. Yanagisawa, Y. Tanaka, I. Hase, and K. Yamaji, "Vortices and chirality in multi-band superconductors", J. Phys. Soc. Jpn. **81**, 024712 (2012).

[115] S.-Z. Lin and X. Hu, "Massless Leggett mode in three-band superconductors with time-reversal-symmetry breaking", Phys. Rev. Lett. **108**, 177005 (2012).

[116] S.-Z. Lin and X. Hu, "Phase solitons in multi-band superconductors with and without time-reversal symmetry", New J. Phys. **14**, 063021 (2012).

[117] S.-Z. Lin, "Ground state, collective mode, phase soliton and vortex in multi-band superconductors", J. Phys.: Condens. Matter **26**, 493202 (2014).

[118] V. Stanev and A. E. Koshelev, "Complex state induced by impurities in multiband superconductors", Phys. Rev. B **89**, 100505 (2014).

[119] L. Komendová, Y. Chen, A. A. Shanenko, M. V. Milošević, and F. M. Peeters, "Two-band superconductors: hidden criticality deep in the superconducting state", Phys. Rev. Lett. **108**, 207002 (2012).

[120] E. Babaev and M. Speight, "Semi-Meissner state and neither type-I nor type-II superconductivity in multicomponent superconductors", Phys. Rev. B **72**, 180502 (2005).

[121] E. Babaev, J. Carlström, and M. Speight, "Type-1.5 superconducting state from an intrinsic proximity effect in two-band superconductors", Phys. Rev. Lett. **105**, 067003 (2010).

[122] E. H. Brandt and M. P. Das, "Attractive vortex interaction and the intermediate-mixed state of superconductors", J. Supercond. Novel Magn. **24**, 57 (2011).

[123] E. H. Brandt, R. G. Mints, and I. B. Snapiro, "Long-range fluctuation-induced attraction of vortices to the surface in layered superconductors", Phys. Rev. Lett. **76**, 827 (1996).

[124] G. Blatter and V. Geshkenbein, "Van der Waals attraction of vortices in anisotropic and layered superconductors", Phys. Rev. Lett. **77**, 4958 (1996).

[125] S. Mukherji and T. Nattermann, "Steric repulsion and van der Waals attraction between flux lines in disordered high T_c superconductors", Phys. Rev. Lett. **79**, 139 (1997).

[126] V. G. Kogan and J. Schmalian, "Ginzburg-Landau theory of two-band superconductors: absence of type-1.5 superconductivity", Phys. Rev. B **83**, 054515 (2011).

[127] E. Babaev and M. Silaev, "Comment on "Ginzburg-Landau theory of two-band superconductors: absence of type-1.5 superconductivity"", Phys. Rev. B **86**, 016501 (2012).

[128] V. G. Kogan and J. Schmalian, "Reply to "comment on 'Ginzburg-Landau theory of two-band superconductors: absence of type-1.5 superconductivity'"", Phys. Rev. B **86**, 016502 (2012).

[129] J. Garaud, J. Carlström, and E. Babaev, "Topological solitons in three-band superconductors with broken time reversal symmetry", Phys. Rev. Lett. **107**, 197001 (2011).

[130] J. Garaud, J. Carlström, E. Babaev, and M. Speight, "Chiral $\mathbb{C}P^2$ skyrmions in three-band superconductors", Phys. Rev. B **87**, 014507 (2013).

[131] K. E. Gray, "Ginzburg-Landau equations, interphase surface energy, and the intermediate state of superconductors with a paramagnetic normal state", Phys. Rev. B **27**, 4157 (1983).

[132] A. A. Abrikosov, "The magnetic properties of superconducting alloys", J. Phys. Chem. Solids **2**, 199 (1957).

[133] J. M. Speight, "Static intervortex forces", Phys. Rev. D **55**, 3830 (1997).

[134] L. Jacobs and C. Rebbi, "Interaction energy of superconducting vortices", Phys. Rev. B **19**, 4486 (1979).

[135] D. Saint-James, G. Sarma, and E. J. Thomas, *Type II Superconductivity* (Pergamon Press, Oxford, 1969).

[136] R. Huebener, *Magnetic Flux Structures in Superconductors*, 2nd ed., Springer Series in Solid-State Sciences (Book 6) (Springer, Berlin, 2001).

[137] J. R. Schrieffer, *Theory of Superconductivity*, 1st ed. (W. A. Benjamin Inc., 1964).

[138] A. A. Abrikosov, L. P. Gor'kov, and I. E. Dzyaloshinski, *Methods of Quantum Field Theory in Statistical Mechanics* (Prentice-Hall Inc, New Jersey, 1963).

[139] J. B. Ketterson and S. N. Song, *Superconductivity* (Cambridge University Press, Cambridge, 1999).

[140] A. L. Fetter and J. D. Walecka, *Quantum Theory of Many-Particle Systems*, 1st ed. (McGraw-Hill, San Francisco, 1971).

[141] X. Hu and Z. Wang, "Stability and Josephson effect of time-reversal-symmetry-broken multicomponent superconductivity induced by frustrated intercomponent coupling", Phys. Rev. B **85**, 064516 (2012).

[142] Y. Takahashi, Z. Huang, and X. Hu, "H-T phase diagram of multi-component superconductors with frustrated inter-component couplings", J. Phys. Soc. Jpn. **83**, 034701 (2014).

[143] R. E. Lagos and G. G. Cabrera, "A two band model for superconductivity: probing interband pair formation", Braz. J. Phys. **33**, 713 (2003).

[144] A. Gurevich, "Enhancement of the upper critical field by nonmagnetic impurities in dirty two-gap superconductors", Phys. Rev. B **67**, 184515 (2003).

[145] J. Geyer, R. M. Fernandes, V. G. Kogan, and J. Schmalian, "Interface energy of two-band superconductors", Phys. Rev. B **82**, 104521 (2010).

[146] A. A. Golubov, J Kortus, O. V. Dolgov, O Jepsen, Y Kong, O. K. Andersen, B. J. Gibson, K Ahn, and R. K. Kremer, "Specific heat of MgB_2 in a one- and a two-band model from first-principles calculations", J. Phys.: Condens. Matter **14**, 1353 (2002).

[147] R. J. LeVeque, *Finite Difference Methods for Ordinary and Partial Differential Equations: Steady-State and Time-Dependent Problems* (Siam, 2007).

[148] A. Iserles, *A First Course in the Numerical Analysis of Differential Equations* (Cambridge University Press, 2009).

[149] Q. Du, "Numerical approximations of the Ginzburg-Landau models for superconductivity", J. Math. Phys. **46**, 095109, – (2005).

[150] H. G. Kaper and M. K. Kwong, "Vortex configurations in type-II superconducting films", J. Comput. Phys. **119**, 120 (1995).

[151] W. D. Gropp, H. G. Kaper, G. K. Leaf, D. M. Levine, M. Palumbo, and V. M. Vinokur, "Numerical simulation of vortex dynamics in type-II superconductors", J. Comput. Phys. **123**, 254 (1996).

[152] Y. Tanaka, "Soliton in two-band superconductor", Phys. Rev. Lett. **88**, 017002 (2001).

[153] J. Garaud and E. Babaev, "Domain walls and their experimental signatures in $s + is$ superconductors", Phys. Rev. Lett. **112**, 017003 (2014).